

BOSTON UNIVERSITY  
GRADUATE SCHOOL OF ARTS AND SCIENCES

Dissertation

**MEASUREMENT OF THE MAGNETIC ANOMALY OF  
THE MUON TO X PARTS PER BILLION IN RUN 1 OF  
THE FERMILAB MUON  $g - 2$  EXPERIMENT**

by

**NICHOLAS BRENNAN KINNAIRD**

B.S., University of Texas at Austin, 2013  
B.S., University of Texas at Austin, 2013  
M.A., Boston University, 2016

Submitted in partial fulfillment of the  
requirements for the degree of  
Doctor of Philosophy

2019

© 2019 by  
NICHOLAS BRENNAN KINNAIRD  
All rights reserved

Approved by

First Reader

---

B. L. Roberts, PhD  
Professor of Physics

Second Reader

---

R. M. Carey, PhD  
Professor of Physics

## **Dedication**

I dedicate this thesis to

## Acknowledgments

Here go all your acknowledgments. You know, your advisor, funding agency, lab mates, etc., and of course your family.

As for me, I would like to thank Jonathan Polimeni for cleaning up old LaTeX style files and templates so that Engineering students would not have to suffer typesetting dissertations in MS Word. Also, I would like to thank IDS/ISS group (ECE) and CV/CNS lab graduates for their contributions and tweaks to this scheme over the years (after many frustrations when preparing their final document for BU library). In particular, I would like to thank Limor Martin who has helped with the transition to PDF-only dissertation format (no more printing hardcopies – hooray !!!)

The stylistic and aesthetic conventions implemented in this LaTeX thesis/dissertation format would not have been possible without the help from Brendan McDermot of Mugar library and Martha Wellman of CAS.

Finally, credit is due to Stephen Gildea for the MIT style file off which this current version is based, and Paolo Gaudiano for porting the MIT style to one compatible with BU requirements.

Janusz Konrad  
Professor  
ECE Department

**MEASUREMENT OF THE MAGNETIC ANOMALY OF  
THE MUON TO X PARTS PER BILLION IN RUN 1 OF  
THE FERMILAB MUON  $g - 2$  EXPERIMENT**

(Order No. )

**NICHOLAS BRENNAN KINNAIRD**

Boston University, Graduate School of Arts and Sciences, 2019

Major Professor: B. L. Roberts, Professor of Physics

**ABSTRACT**

This abstract was copied from my departmental seminar, and it needs to be updated for my thesis: One of the few indications for new physics is the discrepancy between the theoretical and experimental values for the anomalous magnetic moment of the muon. There is a 3 to 4 sigma discrepancy between theory and the last experimental measurement held at Brookhaven National Laboratory in 2001, which measured the muon g-2 to 540 parts per billion. This discrepancy has been consistent for many years now with ever improving theoretical calculations and other experimental measurements. In order to resolve or confirm this difference, a new experiment is underway at Fermilab to measure the muon g-2 to 4 times higher precision at 140 ppb. Muon g-2 at Fermilab gathered its first production data in 2018, and is currently taking data now. I will describe the principles of the experiment and detail two specific parts of the analysis that I have been involved in. These include track fitting and precession frequency analysis of the Run 1 data.

# Contents

<b>1</b>	<b>Introduction</b>	<b>1</b>
1.1	Magnetic moments of particles . . . . .	2
1.2	Standard Model contributions to $a_\mu$ . . . . .	3
1.2.1	QED . . . . .	3
1.2.2	Electroweak . . . . .	4
1.2.3	Hadronic . . . . .	5
1.2.4	Combined Standard Model value . . . . .	9
1.3	Experimental value of $a_\mu$ and discrepancy with $a_\mu^{\text{SM}}$ . . . . .	10
1.4	Beyond the Standard Model and the purpose of E989 . . . . .	10
<b>2</b>	<b>Principle Techniques of E989</b>	<b>14</b>
2.1	Measuring $\omega_a$ . . . . .	16
2.2	Measuring the magnetic field . . . . .	21
2.3	Production of polarized muons . . . . .	26
2.4	Injection of muons . . . . .	29
2.5	Storage of muons . . . . .	30
2.5.1	Kicker . . . . .	32
2.5.2	Electrostatic quadrupoles . . . . .	34
2.6	Muon beam dynamics . . . . .	36
2.6.1	Coherent betatron oscillation . . . . .	39
2.6.2	Beam debunching . . . . .	40
2.7	Corrections to $\omega_a$ . . . . .	41

2.7.1	Electric field correction . . . . .	41
2.7.2	Pitch correction . . . . .	44
2.8	Run 1 in E989 . . . . .	47
<b>3</b>	<b>Detector Systems</b>	<b>51</b>
3.1	Auxiliary detectors . . . . .	51
3.1.1	T0 . . . . .	51
3.1.2	Inflector Beam Monitoring System . . . . .	52
3.1.3	Fiber harps . . . . .	53
3.2	Calorimeters . . . . .	55
3.2.1	Requirements and systematic effects . . . . .	55
3.2.2	Hardware . . . . .	56
3.2.3	Laser calibration system . . . . .	59
3.3	Straw trackers . . . . .	59
3.3.1	Tracker readout electronics . . . . .	64
<b>4</b>	<b>Track Reconstruction and Analysis</b>	<b>67</b>
4.1	Track finding . . . . .	67
4.2	Track fitting . . . . .	70
4.2.1	Error propagation and coordinate systems . . . . .	70
4.2.2	$\chi^2$ minimization . . . . .	78
4.2.3	Fits to idealized tracks in vacuum . . . . .	81
4.2.4	Material correlations . . . . .	82
4.2.5	Fits to simulated tracks including material effects . . . . .	86
4.2.6	Left-right ambiguity and fit modes . . . . .	94
4.2.7	Fits to tracks from data and comparison with Monte-Carlo . .	96
4.3	Track extrapolation . . . . .	99
4.4	Muon beam measurements . . . . .	99

<b>5</b>	<b><math>\omega_a</math> Measurement</b>	<b>108</b>
5.1	Reconstruction . . . . .	108
5.2	Histogramming . . . . .	114
5.2.1	Pileup subtraction . . . . .	114
5.3	Lost muons . . . . .	114
5.4	Fitting . . . . .	115
5.4.1	CBO terms . . . . .	116
5.5	Systematic errors . . . . .	116
5.5.1	Gain . . . . .	116
5.5.2	Pileup . . . . .	116
<b>6</b>	<b>Conclusion</b>	<b>117</b>
6.1	Run 1 value of $a_\mu$ . . . . .	117
<b>A</b>	<b><math>g</math> for Spin-1/2 Particles</b>	<b>118</b>
<b>B</b>	<b>Straw measurement angular correction</b>	<b>121</b>
<b>C</b>	<b>Ratio Method Derivation</b>	<b>124</b>
C.1	Ratio form and function . . . . .	124
C.2	Ratio errors . . . . .	129
<b>D</b>	<b>Pileup Modified Errors</b>	<b>130</b>
D.1	Pileup errors for the ratio function . . . . .	133

# List of Tables

2.1	Uncertainties in the magnetic field measurement . . . . .	26
2.2	Muon beam frequencies in the E989 experiment . . . . .	37
2.3	Run 1 datasets . . . . .	50
4.1	Run 1 dataset muon beam parameters . . . . .	105
5.1	Uncertainties in the precession frequency measurement . . . . .	116
D.1	Number of doublet counts added to pileup histogram from shadow method . . . . .	131

# List of Figures

1.1	QED diagrams contributing to the magnetic moment . . . . .	4
1.2	Electroweak diagrams contributing to the magnetic moment . . . . .	5
1.3	First order hadronic vacuum polarization diagram contributing to the magnetic moment . . . . .	7
1.4	Hadronic light-by-light diagrams contributing to the magnetic moment	8
1.5	Comparison between theoretical and experimental values for $a_\mu$ . . . .	9
1.6	General diagram for new physics . . . . .	12
1.7	Citations for E821 publications vs year . . . . .	12
2.1	Feynman diagram for muon decay . . . . .	17
2.2	Muon decay for maximum and minimum energy decay positrons . . . .	17
2.3	Number distribution and asymmetry for muon decay in the muon rest frame and lab frame . . . . .	18
2.4	$g - 2$ time spectrum example . . . . .	20
2.5	Magnet cross section . . . . .	22
2.6	FID signal . . . . .	23
2.7	Azimuthally averaged magnetic field sample . . . . .	24
2.8	Fermilab accelerator layout for muon delivery to E989 . . . . .	27
2.9	Fermilab accelerator pulse train . . . . .	28
2.10	Muon injection point through inflector . . . . .	30
2.11	Superconducting inflector magnet . . . . .	31
2.12	The E989 experiment . . . . .	31

2.13	Vacuum chamber map . . . . .	33
2.14	Electrostatic quadrupoles installed in a vacuum chamber . . . . .	35
2.15	Electrostatic quadrupole potentials . . . . .	35
2.16	Tune plane . . . . .	38
2.17	Coherent betatron oscillation . . . . .	40
2.18	Beam debunching fast rotation . . . . .	42
2.19	Pitching beam motion . . . . .	45
2.20	Electrostatic quadrupole high voltage traces . . . . .	48
3.1	T0 counter and pulses . . . . .	52
3.2	IBMS Models . . . . .	53
3.3	IBMS Positions . . . . .	53
3.4	Fiber harp and measurement . . . . .	54
3.5	Calorimeters . . . . .	57
3.6	SiPM pulse . . . . .	58
3.7	Straw tracker drift circles . . . . .	61
3.8	Tracker module . . . . .	62
3.9	Tracker module coordinate system . . . . .	63
3.10	TrackerCaloWithLines . . . . .	65
3.11	Tracker electronics readout chain . . . . .	66
4.1	Track candidate selection . . . . .	69
4.2	Vertical and radial magnetic fields calculated in Opera2D . . . . .	72
4.3	Free and surface tracking coordinate systems . . . . .	74
4.4	Tracker reference frame . . . . .	74
4.5	Transport and error matrices for straw tracker planes . . . . .	76
4.6	Natural tracker measurement system . . . . .	78
4.7	$P$ value and $\chi^2$ distribution for fitted tracks in vacuum . . . . .	82

4.8	Track parameter truth pulls for fitted tracks in vacuum . . . . .	83
4.9	Material scattering error in tracker . . . . .	84
4.10	$\chi^2$ for fitted tracks including material effects but no correlations . . . . .	85
4.11	P value and $\chi^2$ distribution for fitted tracks in the $g - 2$ Geant4 simulation with material effects included . . . . .	87
4.12	Simulated true energy loss vs Geant predicted energy loss for tracks .	88
4.13	Track parameter truth pulls for fitted tracks in the $g - 2$ Geant4 simulation with material effects included . . . . .	89
4.14	Number of iterations for the track fitting to converge . . . . .	90
4.15	Number of planes hit for fitted tracks . . . . .	90
4.16	Fitted track momentum distribution and corresponding residuals to truth . . . . .	91
4.17	Fitted track vertical and horizontal momenta and corresponding residuals to truth . . . . .	92
4.18	Fitted track vertical and horizontal positions and corresponding residuals to truth . . . . .	93
4.19	P value distribution for fitted tracks in data . . . . .	97
4.20	Fitted tracks in data compared to Monte-Carlo, track times and total momentum . . . . .	97
4.21	Fitted tracks in data compared to Monte-Carlo, radial and vertical momentum and position distributions . . . . .	98
4.22	Birds eye view of extrapolation in ring . . . . .	100
4.23	Extrapolated muon beam distribution cross-section . . . . .	103
4.24	Muon beam radial and vertical distributions . . . . .	103
4.25	Muon beam radial and vertical distributions as a function of time in-fill	104

4.26 Muon beam radial and vertical distribution means as a function of time in-fill . . . . .	104
4.27 CBO frequency as a function of time . . . . .	106
4.28 CBO amplitude as a function of time . . . . .	107
5.1 Template fit to SiPM trace . . . . .	110
5.2 In-fill gain function fit for a single calorimeter crystal . . . . .	112
5.3 Calorimeter cluster from SiPM traces fit with templates . . . . .	113
5.4 put caption here . . . . .	114
B.1 Angular correction for measured DCAs . . . . .	122

## List of Abbreviations

ASDQ	.....	Amplifier Shaper Discriminator with charge (Q)
ASIC	.....	application specific integrated circuit
BNL	.....	Brookhaven National Laboratory
BSM	.....	beyond the standard model
CBO	.....	coherent betatron oscillation
E821	.....	Brookhaven Muon $g - 2$ Experiment
E989	.....	Fermilab Muon $g - 2$ Experiment
EW	.....	electroweak
FID	.....	free-induction decay
FNAL	.....	Fermi National Accelerator Laboratory
Geane	.....	Geometry and Error Propagation
Geant	.....	Geometry and Tracking
HLbL	.....	hadronic light-by-light
HVP	.....	hadronic vacuum polarization
IBMS	.....	inflector beam monitoring system
NMR	.....	nuclear magnetic resonance
PCB	.....	printed circuitry board
PMT	.....	photo-multiplier tube
POT	.....	protons on target
ppb	.....	parts per billion
ppm	.....	parts per million
ppt	.....	parts per trillion
QCD	.....	quantum chromodynamics
QED	.....	quantum electrodynamics
RMS	.....	root mean square
SiPM	.....	silicon photo-multiplier
SM	.....	Standard Model
STDP	.....	short-term double pulse
VW	.....	vertical waist
WFD	.....	waveform digitizer

# Chapter 1

## Introduction

The prevailing theory of particle physics, the Standard Model (SM), has had tremendous success in describing our universe. It has been used to predict and explain a wide variety of phenomena, particles, properties, and interactions to great precision. However, in spite of its success in explaining nearly all experimental results, there remain unanswered questions about our universe. Some of these include the matter-antimatter asymmetry, the source of mass for the neutrinos, the existence of dark matter, and an inability to fully incorporate our best theory of gravitation. Many particle physics experiments around the world are being devised and conducted in order to shed light on these questions and improve our understanding of reality. One such experiment is the Fermilab Muon  $g - 2$  Experiment (E989) underway at the Fermi National Accelerator Laboratory (FNAL) located in Batavia, Illinois.

I have been a part of the E989 experiment since I began my graduate degree six years ago. This dissertation will describe the E989 experiment and the work which I have done for it in detail. Chapter 1 will provide experimental and theoretical background to the experiment, as well its motivation. Chapter 2 will describe the experimental principle and specifics of muon production and storage. Chapter 3 will describe the various detector systems. Chapter 4 will describe the straw tracking reconstruction including the track fitting algorithm that I developed, as well as some analysis results. Chapter 5 will describe the precession frequency measurement portion of the experiment, and detail my analysis results from data taken in the

experiment’s first run in 2018. Chapter 6 will conclude the thesis and the results contained within.

## 1.1 Magnetic moments of particles

In order to understand the purpose of the Fermilab Muon  $g - 2$  Experiment, first we need to understand the meaning of the  $g$  in  $g - 2$ . This is what the experiment is measuring. All particles have intrinsic properties. One property of charged particles is the magnetic dipole moment.<sup>1</sup> This property of a particle is related to its spin through the equation

$$\vec{\mu} = g \frac{q}{2m} \vec{s}, \quad (1.1)$$

where  $\vec{\mu}$  is the magnetic dipole moment of a particle,  $\vec{s}$  is its spin vector,  $m$  is its mass,  $q = \pm e$  where  $e$  is the elementary charge, and  $g$  is the so called “Landé g-factor”.  $g$  is a measurable and predictable constant. Since the torque on a particle in a magnetic field is

$$\vec{N} = \vec{\mu} \times \vec{B}, \quad (1.2)$$

the rate at which a particles spin precesses in a magnetic field will depend on  $g$ . This is one of the key physics principles in the E989 experiment as will be discussed later.

In a Dirac theory,  $g$  is equal to 2 for spin- $\frac{1}{2}$  particles with no internal structure [1]. See Appendix A for a derivation of this result. It turns out however, that in reality  $g$  is not quite equal to 2 even for these types of particles. Motivated by early experimental discrepancies such as the measurements of the hyperfine structure in hydrogen [2], in 1948 Schwinger calculated the first “radiative correction” to the electron magnetic moment [3]. In a quantum field theory, interactions of the particle

---

<sup>1</sup>*Magnetic dipole moment* and *magnetic moment* are equivalent when talking about particles.

with virtual particles in loops will contribute to the value of  $g$ . In this context it is convenient to recast the magnetic dipole moment formula as

$$\vec{\mu} = 2(1 + a) \frac{q}{2m} \vec{s},$$

$$a = \frac{g - 2}{2}, \quad (1.3)$$

where  $a$  is called the “magnetic anomaly,” and contains all higher order corrections to  $g$ . The first correction calculated to  $a$  by Schwinger was  $a = \alpha/2\pi \approx 0.00116$ , where  $\alpha$  is the fine structure constant. By measuring  $a$ , the SM theory can be tested and extensions to it constrained. A precise measurement of the magnetic anomaly, or the anomalous magnetic moment of the muon, is the main goal of the Fermilab Muon  $g - 2$  Experiment.

## 1.2 Standard Model contributions to $a_\mu$

Any complete theory must agree with experimental observations. The latest theoretical predictions for the muon magnetic moment will be presented here. The contributions to  $a_\mu$  can be summed from separate pieces relating to different parts of the SM. These include the quantum-electrodynamics (QED) corrections purely from other leptons and photons, the electroweak (EW) corrections from interactions with the weak force bosons  $W^\pm$  and  $Z^0$ , and the hadronic corrections from interactions with hadrons:

$$a_\mu^{\text{SM}} = a_\mu^{\text{QED}} + a_\mu^{\text{EW}} + a_\mu^{\text{Had}} \quad (1.4)$$

### 1.2.1 QED

The QED contributions to  $a_\mu$  stem solely from loops with virtual leptons and photons. They are very well understood and have been calculated to very high order, having

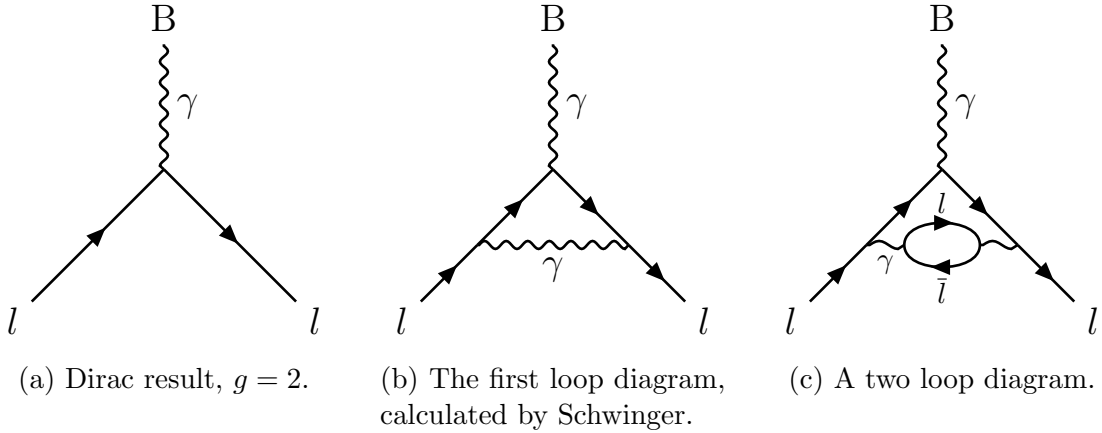


Figure 1.1: The first of many QED diagrams contributing to  $a$ . B is an external magnetic field. Feynman diagrams made with References [4, 5].

been calculated up to five-loop level from over 12,000 Feynman diagrams. This has been done with both analytical and numerical methods. The first couple of diagrams including the Dirac  $g = 2$  and Schwinger diagrams are shown in Figure 1.1. The value is [6, 7]

$$a_\mu^{\text{QED}} = \sum_{n=1}^{\infty} C_n \left(\frac{\alpha}{\pi}\right)^n, \quad (1.5)$$

$$= (11658471.8971 \pm 0.0007) \times 10^{-10},$$

where in the first line  $a_\mu^{\text{QED}}$  is expressed as a perturbative expansion in the fine structure constant, and the value comes from the expansion up to  $n = 5$ .  $C_1 = 1/2$  is the Schwinger result mentioned previously stemming from the diagram shown in Figure 1.1b. Over 99% of the value of  $a_\mu$  comes from the QED sector, but the error is much smaller than the other contributions.

### 1.2.2 Electroweak

The electroweak contributions to  $a_\mu$  are known to two-loop level, with some three-loop parts estimated. The contributions stem from couplings with the heavy weak gauge bosons. The different one loop diagrams are shown in Figure 1.2. Per usual

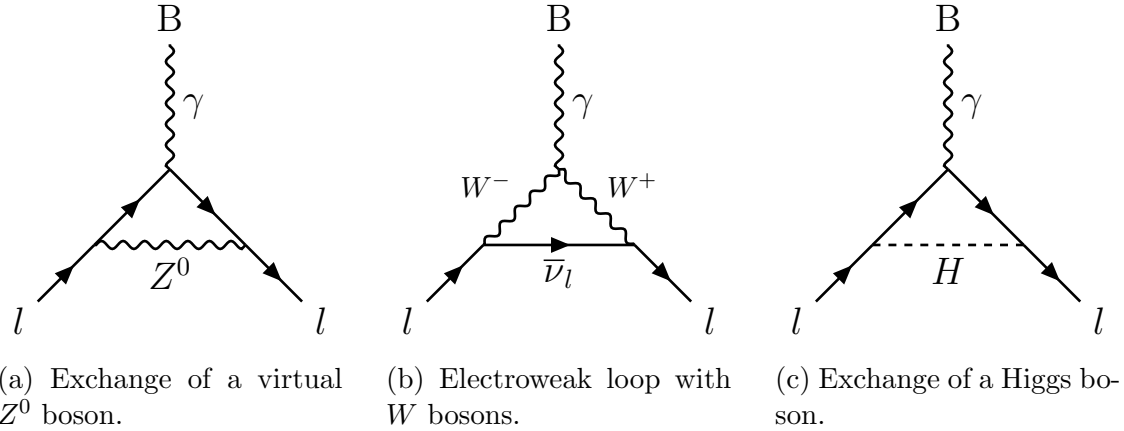


Figure 1.2: First order weak diagrams contributing to  $a$ . B is an external magnetic field. Feynman diagrams made with References [4, 5].

Feynman rules, the propagators will contain the masses of the interacting bosons, while the kinematics will contain the masses of the leptons. For calculations of a muon in the case of Figure 1.2a, these result in a factor  $\sim (m_\mu/m_{Z^0})^2$ . Because the mass of the gauge bosons are so much more than the muon, these processes are necessarily suppressed and the electroweak contributions to  $a_\mu$  are small. For this reason knowing these contributions only up to two loop level is sufficient. To this degree of accuracy, the value of the electroweak contributions is [8, 9]

$$a_\mu^{\text{EW}} = (15.12 \pm 0.01) \times 10^{-10}, \quad (1.6)$$

with improvements having been made recently. Again the error on these contributions is small compared to the hadronic contributions discussed next, as well as the experimental uncertainty.

### 1.2.3 Hadronic

The hadronic contributions to  $a_\mu$  arise from interactions with virtual hadrons. Because they cannot be calculated perturbatively at low energies, due to the nature of quantum chromodynamics (QCD), these calculations comprise the dominant uncer-

tainty in the SM calculation. This makes their error estimation extra important when comparing to experiment. Most active work on  $a_\mu$  in the theoretical community is in this sector. These contributions can be separated into two parts:

$$a_\mu^{\text{Had}} = a_\mu^{\text{HVP}} + a_\mu^{\text{HLbL}} \quad (1.7)$$

### Hadronic Vacuum Polarization

The first of these hadronic contribution parts is the hadronic vacuum polarization part (HVP), the first order diagram of which is shown in Figure 1·3a. There are two main prescriptions for calculating these contributions. The first is to use a dispersive approach to introduce a virtual hadron bubble into the integral calculation for the photon propagator<sup>2</sup>, and then utilize the optical theorem to relate the imaginary part of that propagator to the total cross-section of electron-positron annihilation to hadrons [11]. While this could be solved perturbatively for a lepton bubble in place of the hadron bubble, this is instead a data driven approach when considering non-perturbative QCD. The leading order contribution can be written as

$$a_\mu^{\text{HVP;LO}} = \left( \frac{\alpha m_\mu}{3\pi} \right)^2 \int_{m_\pi^2}^{\infty} \frac{ds}{s^2} K(s) R(s) \quad (1.8)$$

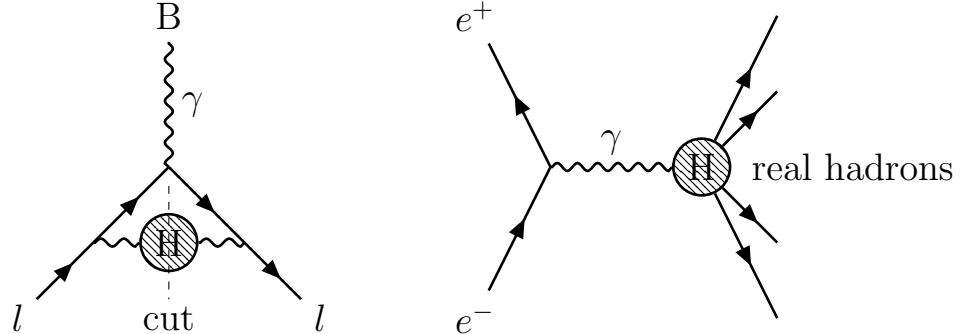
where  $K(s)$  is some calculable kinematic factor, and  $R(s)$  is a ratio of cross-sections

$$R(s) = \frac{\sigma(e^+e^- \rightarrow \text{hadrons})}{\sigma(e^+e^- \rightarrow \mu^+\mu^-)}. \quad (1.9)$$

The cross-section data for this relation has been measured in different energy ranges by various experiments, including KLOE, CLEO, BaBar, and BESIII [12, 13, 14, 15].

---

<sup>2</sup>The details of dispersion theory will not be described here but a pedagogical introduction is given in Reference [10].



(a) The first order HVP diagram. The bubble H in the middle indicates any combination of hadrons which satisfy the Feynman rules.

(b) The Feynman diagram for electron positron annihilation to hadrons.

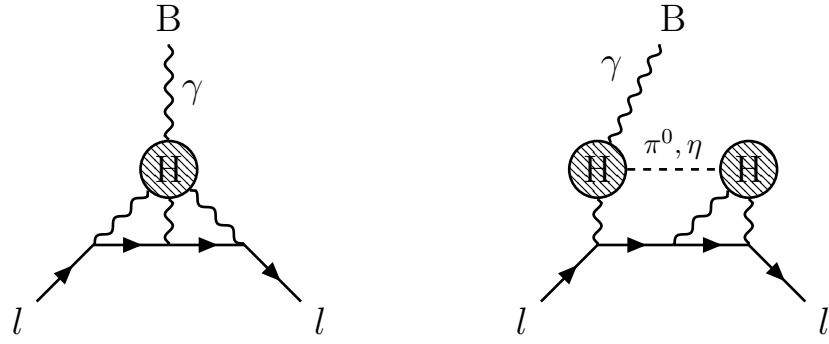
Figure 1.3: The first order HVP diagram on the left, which can be related to the diagram on the right by making a ‘cut’ across the virtual hadrons bubble. B is an external magnetic field. Feynman diagrams made with References [4, 5].

The analysis by Keshavarzi et al. [16] gives results as

$$\begin{aligned} a_\mu^{\text{HVP;LO}} &= (693.26 \pm 2.46) \times 10^{-10}, \\ a_\mu^{\text{HVP;NLO}} &= (-9.82 \pm 0.04) \times 10^{-10}, \end{aligned} \quad (1.10)$$

where  $a_\mu^{\text{HVP;NLO}}$  is the next-to-leading order calculation. This evaluation is consistent with Davier et al. [17].

The second prescription to estimating the HVP contributions is a first principles approach, using lattice QCD and QED. It is a gauge theory defined on a matrix of points in time and space. Once the matrix is taken infinitely large with the spacing between the points infinitely small, the behavior from a continuous theory is recovered. The results for the leading order estimates of  $a_\mu^{\text{HVP;LO}}$  are consistent with those provided above, though the error is larger. If the calculation is supplemented with the cross-section data described above, then this method provides the most precise determination of  $a_\mu^{\text{HVP;LO}}$  [18].



(a) The first HLbL diagram, where three photons are exchanged with some virtual hadrons bubble.

(b) A second HLbL diagram, where three photons are exchanged with two virtual hadrons bubbles, that are connected with some virtual charge-less propagator.

Figure 1.4: HLbL diagrams contributing to  $a_\mu$ . B is an external magnetic field. Feynman diagrams made with References [4, 5].

### Hadronic Light-by-Light

The second of these hadronic contribution parts is a higher order four-photon interaction, termed hadronic light-by-light (HLbL). Diagrams are shown in Figure 1.4. Again perturbation theory is unable to assist in the calculation of these contributions. For a long time the calculation of these diagrams was model dependent, and has therefore been the most contentious part of the SM calculation. In more recent years, there have been efforts to produce results using dispersive [19, 20, 21] and lattice approaches [22, 23, 24]. A cumulative report on recent progress is given by N. Asmussen et al. [25]. The error on this contribution is large due to these various approaches, comparable to that of the  $a_\mu^{\text{HVP;LO}}$  term, even though the size of this contribution is small. The value of the HLbL contributions to  $a_\mu$  given by Nyffeler [26] comes from model estimates and is

$$a_\mu^{\text{HLbL}} = (9.8 \pm 2.6) \times 10^{-10}. \quad (1.11)$$

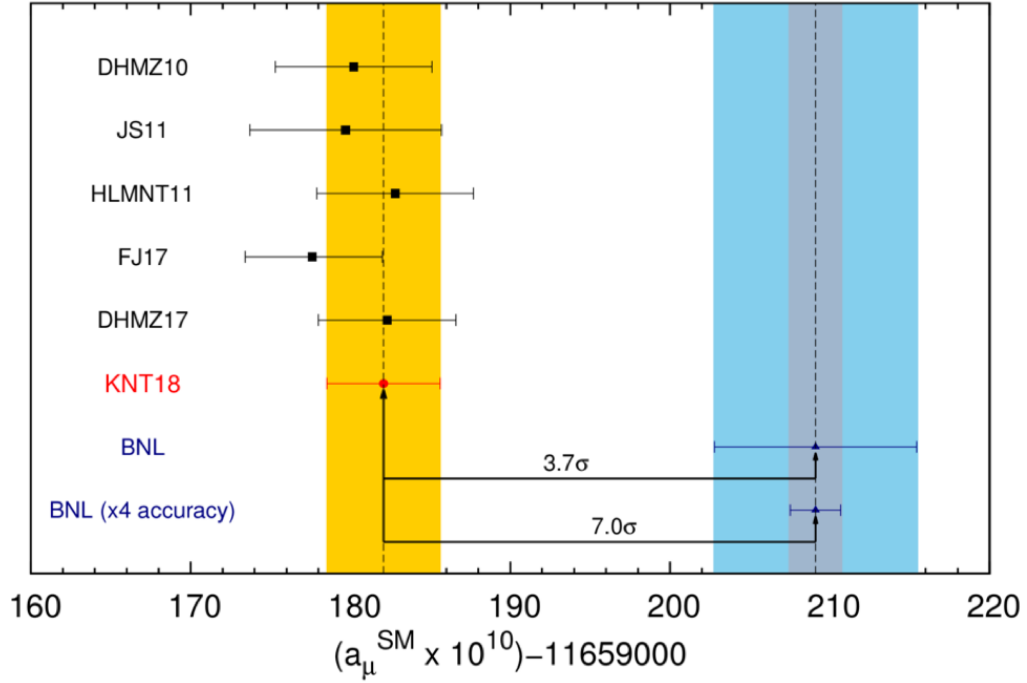


Figure 1.5: Various theoretical values for  $a_\mu$  on the left, as compared to the most recent and extrapolated experimental result on the right [16].

#### 1.2.4 Combined Standard Model value

The sum of the  $a_\mu$  contributions listed here is [6, 7, 8, 9, 16, 26]

$$\begin{aligned} a_\mu^{\text{SM}} &= a_\mu^{\text{QED}} + a_\mu^{\text{EW}} + a_\mu^{\text{Had}}, \\ &= (11659180.26 \pm 3.58) \times 10^{-10}. \end{aligned} \tag{1.12}$$

The relative uncertainty of this result is 307 parts per billion (ppb). Other analyses with different values for the various contributions typically agree well, as shown on the left side of Figure 1.5. In general the consistency of the theory has been stable for almost ten years now. Depending on which calculations are used, the discrepancy between theory and experiment ranges between 3 to 4 standard deviations. The latest experimental result is described in the following section.

### 1.3 Experimental value of $a_\mu$ and discrepancy with $a_\mu^{\text{SM}}$

The theoretical contributions to  $a_\mu$  listed in the previous sections have improved over time as methods have matured and more experimental data has been gathered. Similarly, work on the direct experimental measurement of  $a_\mu$  has been going on for decades, with more precise results being determined over time [27]. The most recent experiment to measure  $g - 2$  was the Brookhaven Muon  $g - 2$  Experiment (E821) held at Brookhaven National Laboratory (BNL) in 2001. That experiment measured a value for  $a_\mu$  of [28]

$$a_\mu^{\text{Exp}} = (11659208.0 \pm 6.3) \times 10^{-10}, \quad (1.13)$$

which corresponds to a 540 ppb relative uncertainty. Note that the uncertainty of the experimental measurement is comparable to that of the theory, necessitating precise understanding of all the different theoretical parts. The difference between the experimental and theoretical values here is

$$a_\mu^{\text{Exp}} - a_\mu^{\text{SM}} = (27.74 \pm 7.25) \times 10^{-10}, \quad (1.14)$$

corresponding to a discrepancy of 3.83 standard deviations from 0.

### 1.4 Beyond the Standard Model and the purpose of E989

While the discrepancy between experiment and theory might be attributed to miscalculations in the theory or systematic errors in the E821 experiment, no such errors have been found despite repeated attempts to resolve the two. Indeed the discrepancy has only grown over time as the theoretical calculations have matured. The most intriguing and exciting source of the discrepancy would be physics beyond the standard model (BSM), Figure 1·6. Since the value of  $a_\mu$  receives contributions from

all particles that couple to the muon through virtual loops, unknown particles might be the source of this discrepancy. Specifically, since the contribution to the magnetic moment from heavy virtual particles goes as

$$a \sim \frac{m^2}{\Lambda^2}, \quad (1.15)$$

where  $\Lambda$  is the mass scale of the new physics and  $m$  the mass of the lepton in question, the sensitivity of the muon as compared to the electron to large mass scales is  $m_\mu^2/m_e^2 \approx 43,000$  times greater. For this reason, it is possible that even though the g-factor of the electron has been measured extraordinarily precisely, to .26 parts per trillion (ppt) corresponding to a .23 ppb relative uncertainty in  $a_e$  [29, 30], it has not yielded a definitive difference between theory and experiment, whereas the magnetic moment of the muon might do so<sup>3</sup>.

Because the discrepancy from the previous experiment was not at the 5 standard deviation level necessary to classify it as a discovery, the E989 experiment was undertaken. Indeed with the lack of new physics results coming out of the LHC and other experiments, E989 is especially positioned to uncover something new at a time where there are so few hints of new physics. Because of this, the interest in the E821 experiment and underway E989 experiment has only grown over time. The number of citations for the E821 results has been consistently for 20 years as shown in Figure 1.7.

The E989 experiment has the goal of measuring  $a_\mu$  to 140 ppb over the course of several years. This would be a factor of four improvement over the E821 result stemming from a twenty times increase in statistics, which was the limiter in the previous experiment. Assuming the same central value for  $a_\mu$  is obtained, this would push the statistical significance of the discrepancy over the five standard deviation

---

<sup>3</sup>A recent measurement of the fine structure constant  $\alpha$  to the highest precision yet [31] has yielded a new value of  $a_e$  for which the difference between theory and experiment is 2.5 standard deviations, but with the opposite sign as compared to  $a_\mu$ .

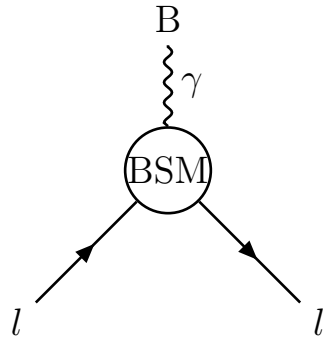


Figure 1·6: A general Feynman diagram, where the leptons couple to an external magnetic field  $B$  through some BSM physics. Feynman diagrams made with References [4, 5].

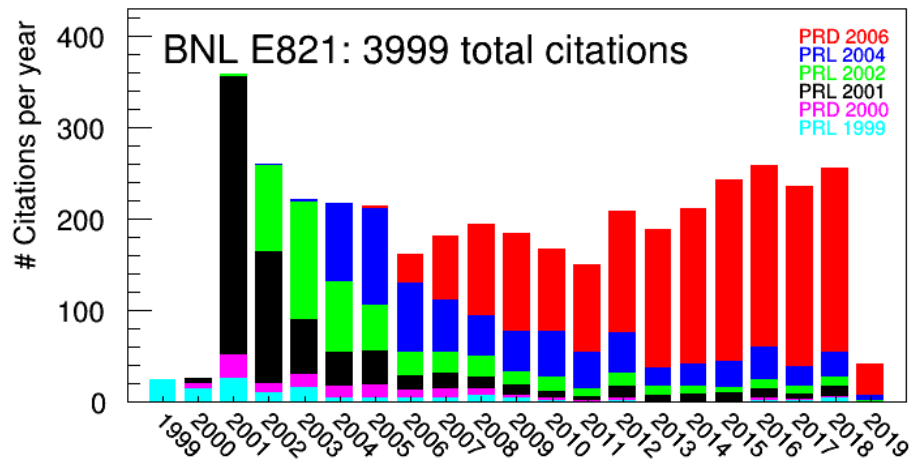


Figure 1·7: The number of citations for the BNL experiment publications as a function of year [32]. **Update this plot before submission.**

mark to approximately seven standard deviations, as shown in Figure 1·5. The data comprising Run 1, gathered between April and July of 2018, is the subject of this thesis, and corresponds to a statistical uncertainty comparable to the E821 result. When it's all said and done, the possibility is that we will measure something new and exciting. Even if we do not however, it is valuable in itself to resolve this theoretical and experimental conflict.

## Chapter 2

# Principle Techniques of E989

A particle with non-zero spin in a magnetic field will experience a torque which attempts to line up the magnetic dipole moment of the particle with the external field. Because of this, in a dipole field a particle's spin will turn at the spin precession frequency [33]

$$\vec{\omega}_s = -g \frac{q}{2m} \vec{B} - (1 - \gamma) \frac{q}{\gamma m} \vec{B}, \quad (2.1)$$

where  $m$  is the particles mass,  $q = \pm e$  where  $e$  is the positive elementary charge,  $g$  is the g-factor,  $\gamma$  is the Lorentz relativistic factor, and  $B$  is an external magnetic field. The first term is the usual Larmor frequency and the second term is a relativistic correction to the precession frequency called Thomas precession. Similarly, a particle with some momentum perpendicular to the magnetic field will orbit at the cyclotron frequency

$$\vec{\omega}_c = -\frac{q}{\gamma m} \vec{B}. \quad (2.2)$$

By taking the difference between these two frequencies we arrive at the “spin difference frequency”

$$\vec{\omega}_a = \vec{\omega}_s - \vec{\omega}_c = -\frac{g-2}{2} \frac{q}{m} \vec{B} = -a \frac{q}{m} \vec{B}, \quad (2.3)$$

a frequency that is directly proportional to anomaly  $a$ . If  $g = 2$  as in a Dirac theory, then the particle's spin would turn at the same rate as the momentum vector, and this spin difference frequency  $\omega_a$  would be identically zero. If this spin difference frequency for a muon and the external magnetic dipole field can be measured, then the anomalous magnetic moment of the muon  $a_\mu$  can be extracted.

As will be detailed in Section 2.2, the measurement of the magnetic field is related to the Larmor precession frequency of free protons in water

$$\omega_p = -g_p \frac{e}{2m_p} B, \quad (2.4)$$

where  $g_p$  and  $m_p$  are the g-factor and mass of the proton respectively. Replacing  $B$  and solving for  $a_\mu$ , we arrive at

$$a_\mu = \frac{g_p}{2} \frac{\omega_a}{\omega_p} \frac{m_\mu}{m_p}. \quad (2.5)$$

Using the magnetic moment formulae for the proton, electron, and muon as shown in Equation 1.1, Equation 2.5 can be transformed to either of the following consistent equations:

$$a_\mu = \frac{g_e}{2} \frac{\omega_a}{\omega_p} \frac{m_\mu}{m_e} \frac{\mu_p}{\mu_e} \quad (2.6)$$

$$a_\mu = \frac{\omega_a/\omega_p}{\lambda - \omega_a/\omega_p} \quad (2.7)$$

Here the  $p$ ,  $e$ , and  $\mu$  subscripts stand for the relevant quantities for the proton, electron, and muon respectively. In the second equation  $\lambda = \mu_\mu/\mu_p$ . As mentioned before the electron g-factor  $g_e$  has been measured to extremely high precision, 0.26 ppt [29, 30]. The muon-electron mass ratio  $m_\mu/m_e$  and muon-proton magnetic moment ratio  $\lambda$  have been measured to 22 ppb [30, 34]. Finally the proton-electron magnetic moment ratio  $\mu_p/\mu_e$  has been measured to 3 ppb [30]. The errors on these terms are

small compared to the target uncertainty for E989 of 140 ppb, the measurement of which now comes down to measuring the ratio  $\omega_a/\omega_p$ .

## 2.1 Measuring $\omega_a$

How can  $\omega_a$  for muons be measured? The answer lies with two key points in the dynamics of muon decay. Positive muons decay to a positron and two neutrinos, as shown in Figure 2·1. The first point is that because of the parity violating nature of the weak interaction, the decay positron will be preferentially emitted right-handed, with its spin directed in the same direction as its momentum [35]. The second key point is that angular momentum must be conserved. Consider the most extreme examples of maximum and minimum energy positrons as shown in Figure 2·2. In the muon rest frame, decay positrons with maximum energy will be emitted opposite to the two neutrinos. Since neutrinos and anti-neutrinos must be left and right-handed respectively, thus having their spins anti-parallel and parallel to their momentum, by the law of conservation of angular momentum the positron must have its spin be parallel to the spin of the muon at the time of the decay. By the opposite argument, decay positrons emitted with minimum energy such that the neutrinos are ejected opposite to one another must have their spins be anti-parallel to that of the muon at the time of decay. Together, these two points mean that higher energy decay positrons will preferentially be emitted in directions parallel to the muon spin at the time of decay, while lower energy decay positrons will preferentially be emitted in directions anti-parallel to the muon spin at the time of the decay.

This correlation between the emitted direction of a high energy decay positron and the spin of the muon is the signature needed to measure  $\omega_a$ . By placing an ensemble of polarized muons within a magnetic storage ring, those muons will orbit at the cyclotron frequency and their spins will precess at the spin precession frequency. As

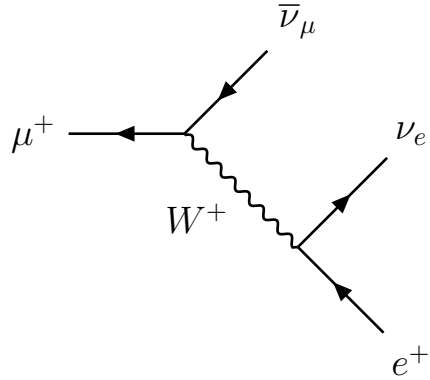


Figure 2·1: Feynman diagram for muon decay.  $\mu^+$  decay through a  $W^+$  boson to a positron, muon anti-neutrino, and an electron neutrino. This process consists of nearly 100% of the muon decay branching ratio, with other decay states including radiative processes.

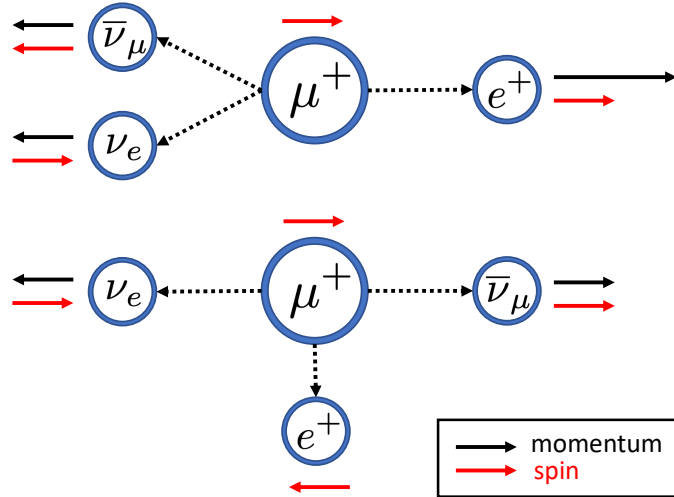


Figure 2·2: Muon decay in the rest frame for maximum (top) and minimum (bottom) energy decay positrons. Due to the conservation of angular momentum and the single possible helicity states of the decay neutrinos, the spin of the decay positron is exactly parallel to the spin of the muon at the time of the decay for maximum energy decay positrons, or anti-parallel for minimum energy decay positrons.

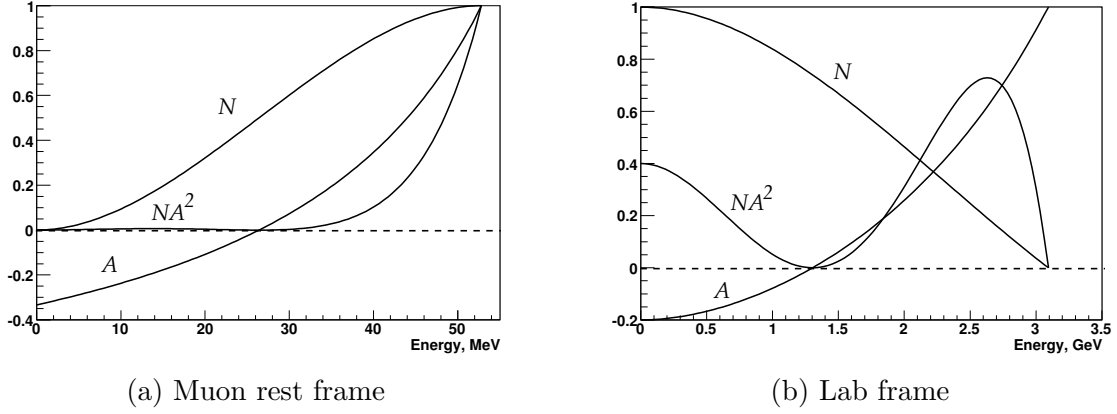


Figure 2.3: Decay number distribution  $N$  and asymmetry  $A$  in the muon rest frame (left) and in the lab frame (right) as a function of positron energy with a maximum positron energy of 3.1 GeV.  $N$  is multiplied by arbitrary factors in both pictures.

they go around the ring they will decay to positrons whose energy and decay directions contain information about the spin of the muon. The differential decay distribution for positive muons in the muon rest frame is described by [35]

$$dP(y, \theta) \propto N(y)[1 + A(y) \cos(\theta)]dyd\Omega, \quad (2.8)$$

where  $y = E/E_{max}$  is the energy fraction of the positron and  $\theta$  is the angle between the spin of the muon and the momentum of the positron at the time of decay.  $N(y)$  is the number distribution of decay positrons and  $A(y)$  is the so called ‘asymmetry’ encoding the preferred positron decay direction. Here the energy of the positron is assumed to be much greater than its mass. The number distribution and asymmetry are given by [35]

$$N(y) = 2y^2(3 - 2y), \quad (2.9)$$

$$A(y) = \frac{2y - 1}{3 - 2y}, \quad (2.10)$$

and are shown in Figure 2.3a.

In the lab frame, nearly all of the highest energy positrons will be emitted parallel to the muon momentum, which makes it challenging to select purely on the decay angle of the positron. That's not a problem however, as we already know that decay positrons with the highest energies will be emitted parallel to the muon spin at the time of decay. Essentially, the energy distribution of detected high energy positrons is modulated by  $\omega_a$ , or  $\theta = \omega_a t + \phi$ . The number of detected positrons at some time and energy in the lab frame for some initial number  $N_0$  of muons can then be described by

$$N_d(t, E) = N_0(E) \cdot e^{-t/\gamma\tau_\mu} \cdot [1 + A(E) \cos(\omega_a t + \phi(E))], \quad (2.11)$$

where the  $d$  subscript stands for ‘detected,’ the muons are decaying with a lifetime of  $\gamma\tau_\mu$ , and all the relevant parameters are energy dependent. Here  $N_0(E)$  and  $A(E)$  have been transformed from Equations 2.9 and 2.10 to the lab frame:

$$N_0(E) \propto (y - 1)(4y^2 - 5y - 5), \quad (2.12)$$

$$A(E) = \frac{-8y^2 + y + 1}{4y^2 - 5y - 5}, \quad (2.13)$$

where as a reminder  $y = E/E_{max}$ . Here the polarization of the muons is assumed to be unity. These relations are shown in Figure 2.3b. To increase the amount of statistics, all positrons above some energy threshold cut  $E_{th}$  can be taken as the observable,

$$N_d(t, E_{th}) = N_0(E_{th}) \cdot e^{-t/\gamma\tau_\mu} \cdot [1 + A(E_{th}) \cos(\omega_a t + \phi(E_{th}))], \quad (2.14)$$

where the number and asymmetry of the detected positrons is now calculated by

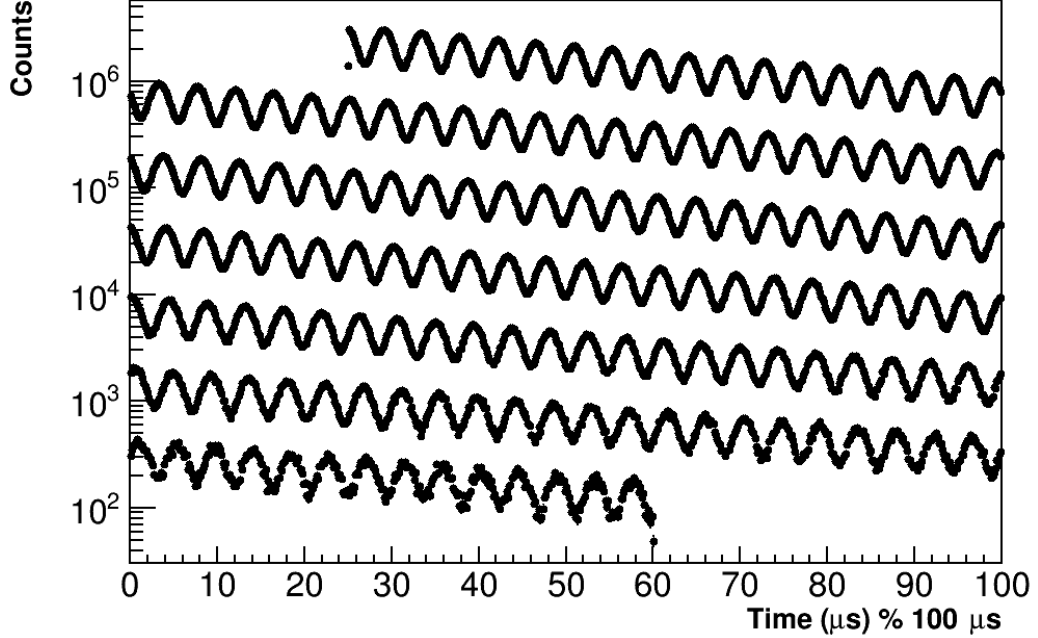


Figure 2.4: The number of detected positrons above some energy threshold ( $y \sim 0.55$ ) as a function of time, where the data plotted come from Run 1 and correspond to nearly  $1 \times 10^9$  counts. The time axis is wrapped around every  $100\text{ }\mu\text{s}$ . See Chapter 5 for how such a histogram is fitted.

simply integrating Equations 2.12 and 2.13 from  $y_{th}$  to 1,

$$N_0(E_{th}) \propto (y_{th} - 1)^2(-y_{th}^2 + y_{th} + 3), \quad (2.15)$$

$$A(E_{th}) = \frac{y_{th}(2y_{th} + 1)}{-y_{th}^2 + y_{th} + 3}, \quad (2.16)$$

where  $y_{th} = E_{th}/E_{max}$ . By counting decay positrons above some energy threshold and fitting the resulting time spectrum with Equation 2.14,  $\omega_a$  can be extracted. An sample of data adhering to such a time spectrum is shown in Figure 2.4.

The statistical error on the  $\omega_a$  measurement, assuming bin errors are Gaussian and a  $\chi^2$  minimization is used with the fit function described in Equation 2.14, is [36]

$$\frac{\sigma_{\omega_a}}{\omega_a} = \frac{\sqrt{2}}{\sqrt{N_{\text{total}}} A \gamma \tau_\mu \omega_a}, \quad (2.17)$$

where  $N_{\text{total}}$  is the total number of counts included in the above-threshold time spectrum. This equation assumes a weighting of one for every count included in the fitted time spectrum. Other weighting schemes exist which slightly improve the statistical precision of the  $\omega_a$  measurement [36], but they are not used in this analysis. What Equation 2.17 reveals is that the statistical precision of  $\omega_a$  is maximized when the quantity  $NA^2$  is at a maximum. It was found for E989 that the optimal energy threshold was about 1.7 GeV as shown in Figure 5·4, which includes detector acceptance effects and corresponds to an asymmetry of about  $A = 0.37$ . Equation 2.17 can be rearranged in order to solve for the number of positrons needed to be collected above threshold for a specific precision goal. For a statistical error of 100 ppb on  $\omega_a$ , the required number of positrons above threshold is approximately  $170 \times 10^9$ , determined from the values  $A = 0.37$ ,  $\gamma = 29.3$  (described later),  $\tau_\mu = 2.2 \mu\text{s}$ , and  $\omega_a = 1.44 \text{ rad}/\mu\text{s}$ . This statistical error of  $\omega_a$  combined with the systematic uncertainties given in Table 5.1, provide the total error on  $\omega_a$ .

## 2.2 Measuring the magnetic field

In order to measure the magnetic moment of the muon to 140 ppb, the field needs to be both highly uniform, and measured to extreme precision. The E989 goal for the field measurement is 70 ppb. As shown in Equation 2.6 the measurement of the magnetic field has equal weight to that of the precession frequency. A cross-section of the magnetic storage ring used in E989 is shown in Figure 2·5. It is an approximately 14 m diameter C magnet, where the muons are stored within a 4.5 cm radius cylindrical storage region at the center of a 1.451 T magnetic field. This corresponds to an approximately  $0.28 \text{ m}^3$  or  $10 \text{ ft}^3$  total volume around the inside of the ring. The magnetic field is made uniform by manipulating many magnetic ‘knobs’ built into the  $g - 2$  storage ring, including the main magnet current, pole

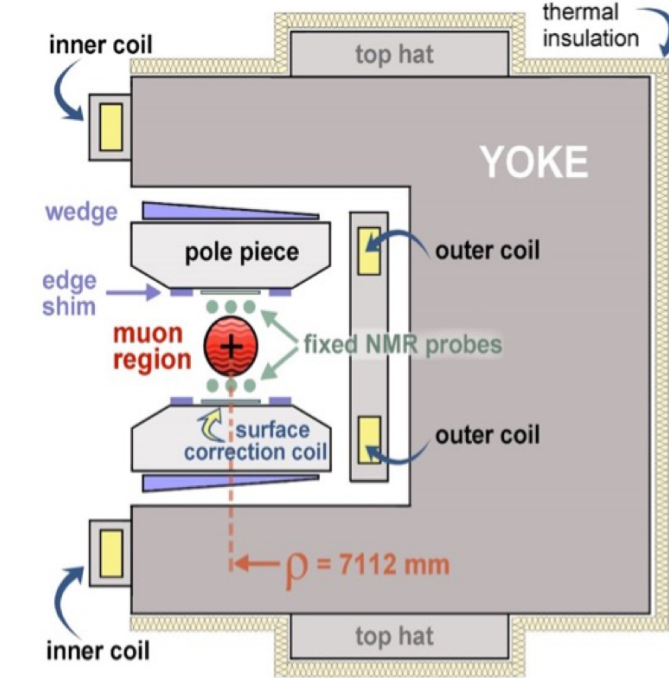


Figure 2·5: Cross-section of the  $g - 2$  magnet. The muons live in the storage region. This is surrounded by many magnetic features of the magnet which allow for sub-ppm level tuning of the magnetic field.

pieces, wedges, top hats, and thousands of small magnetic shims placed around the storage region, as shown in Figure 2·5. There is also an active feedback system which stabilizes the magnetic field over time using current carrying coils near the storage region. After a several month shimming campaign by many members of the field team, a precision on the magnetic field of approximately 25 ppm RMS (root mean square) was achieved.

Measuring the magnetic field comes down to measuring  $\omega_p$  as shown in Equation 2.4. This is because the magnetic field measurement is made using a pulsed nuclear magnetic resonance technique (NMR). NMR was chosen as it provides a field measurement precision on the order of 10 ppb with negligible statistical uncertainty [37]. NMR probes work by rotating the magnetization of a sample of protons in some fluid, typically water or petroleum jelly, and then measuring the Larmor frequency

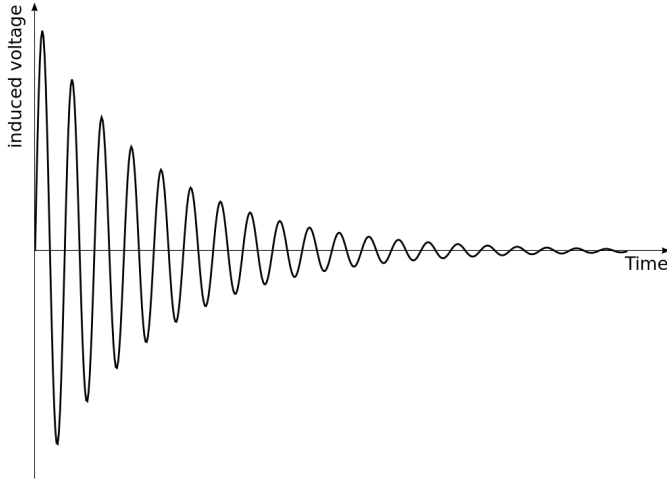


Figure 2·6: An example FID signal. The current picked up in the coils around the proton sample will oscillate as the spins precess around the main magnetic field, and decay as the spins return to alignment with the external field.

( $\approx 61.79$  MHz) of the free-induction decay (FID) signal of the proton spins. The magnetization of the protons will relax back to equilibrium with the external field as the spins of the protons interact with local magnetic field gradients or inhomogeneities, typically on the order of several milliseconds. Pickup coils are located around the sample which both deliver the pulse to rotate the proton sample magnetization and measure the FID signal. An example of an FID signal is shown in Figure 2·6.

Technically, it is not solely  $\omega_p$  that needs to be measured. What really matters is the average magnetic field that the muons see, or the time-averaged spatially-weighted magnetic field. The scheme devised to measure this is two-fold. First, the magnetic field in the muon storage region is measured by a trolley which travels around the inside of the ring. This trolley holds 17 NMR probes and measures the field at approximately 6000 locations around the inside of the ring. However, because the trolley cannot be in the storage region when the muons are present in the ring, during data taking it is retracted and the field is instead monitored by 378 fixed NMR

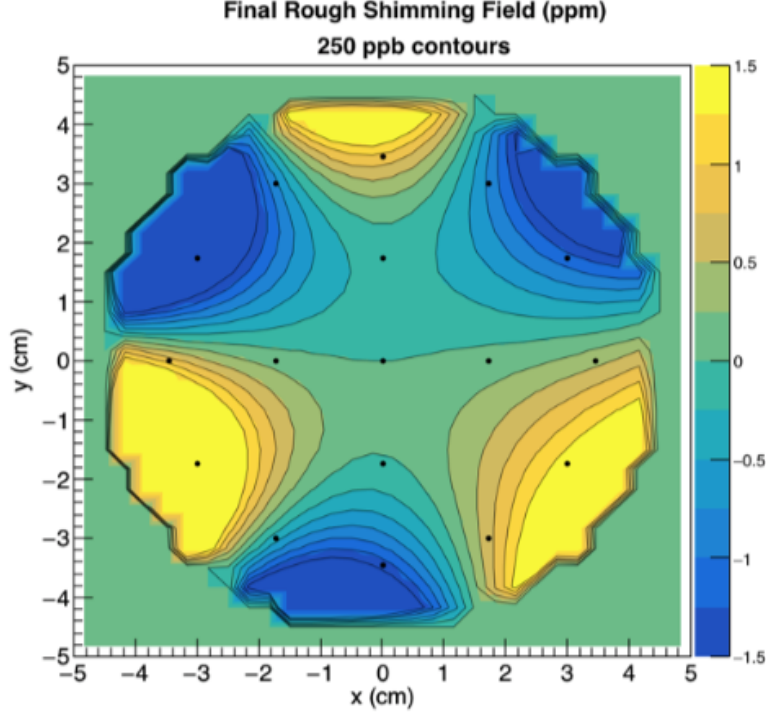


Figure 2·7: A sample of the azimuthally-averaged magnetic field within the storage region [38]. The contours are normalized to the field value at the center of the storage region. The scale of the field differences is approximately  $\pm 1.5$  ppm. The black dots in the picture correspond to the location of the trolley probes.

probes located in the high magnetic field region, but just outside the storage region. The prescription is that the storage ring field is measured every few days by the trolley probes, and the field between trolley runs is interpolated using measurements from the continually-sampling fixed probes. In this way the magnetic field can be mapped over time and over the space in which the muons are stored. A sample of the azimuthally-averaged magnetic field measured with trolley and fixed probes is shown in Figure 2·7.

Lastly, it is the free proton precession frequency in the field that is of interest, but the frequency that the trolley probes measure will be different due to the molecular properties of the proton sample as well as the material properties of the probe itself.

The frequency that the probes measure can be re-cast as

$$\omega_{p,\text{probe}} = \omega_{p,\text{free}}(1 - \sigma(\text{H}_2\text{O}, T) + \delta_b + \delta_p + \delta_s), \quad (2.18)$$

where  $\sigma(\text{H}_2\text{O}, T)$  is the temperature dependent diamagnetic shielding of protons in a water molecule, and the  $\delta$ 's come from corrections due to the bulk susceptibility of the water sample, paramagnetic impurities in the water sample, and the magnetic effects of the probe itself, respectively [37]. In order to correct for these effects two additional special probes are used, both of which live in a single section of the ring which has been shimmed to extra uniformity. The first is a calibration probe which measures the free proton precession frequency at the center of the storage region corresponding to the placement of the central trolley probe. The calibration probe is made of materials in order to reduce the effects in Equation 2.18 and has been characterized in other test magnets. The second special probe is called the ‘plunging probe.’ This probe lives inside the vacuum chamber and drops into the storage region to measure the field at each of the 17 trolley probe locations, using a three dimensional motion system. By using these two probes, the calibration for the free proton precession frequency can be transmitted to each of the trolley probes, providing an absolute scale for the measurements inside the muon storage region. This calibration procedure is estimated to take up about half of the target systematic uncertainty of 70 ppb at 35 ppb.

Other pieces of the systematic uncertainty include the calibrations of the probes, errors in the trolley measurements, the interpolation with the fixed probes, the uncertainty relative to the muon distribution, and others such as time dependent external magnetic fields, Table 2.1.

<b>Magnetic Field Measurement Uncertainties</b>	
Source of uncertainty	E989 Goal (ppb)
Absolute calibration of standard probe	35
Calibration of trolley probes	30
Trolley measurements	30
Fixed probe interpolation	30
Muon distribution weighted average	10
Time dependent external fields	5
Others	30
Quadrature sum	70

Table 2.1: Systematic errors in the magnetic field measurement. Unlisted sources of error include the measurement of higher field multipoles, trolley temperature and power supply voltage response effects, and eddy currents from the kicker, among others.

### 2.3 Production of polarized muons

As explained in Section 2.1, the number of detected high energy positrons depends on the muon spin at the time of decay. In order for this detected quantity to be meaningful, the muon spins themselves need to be highly polarized. Using the same parity-violation and spin momentum conservation logic as expounded upon in muon decay, it is determined that pion decay produces muons that are 100% polarized in the pion rest frame, due to the pion having zero spin. It's also important to note that pions decay to muons with a  $\sim 99.98\%$  branching ratio due to the parity violating nature of the weak interaction, and thus a preference for the heavier muon over the electron [39]. These two facets of pion decay are used to construct polarized muon beams.

In order to measure  $g - 2$  to high precision, a very large number of positrons need to be detected as described in Section 2.1, and hence a large number of highly polarized muons injected into the storage ring. The BNL E821 experiment observed

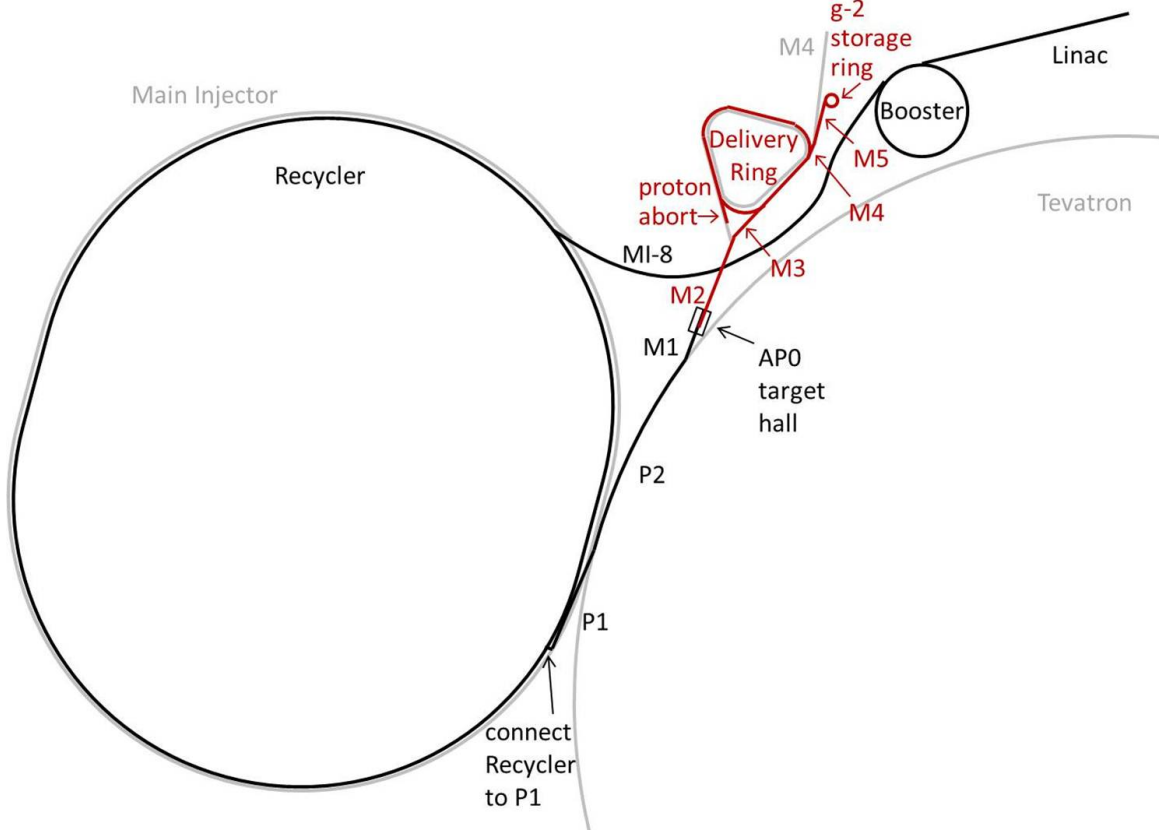


Figure 2.8: The layout of accelerator beam-line components Fermilab uses to provide polarized muons to E989. Protons start in the Linac, traverse around the Booster and then Recycler, and are converted to pions at AP0. The pions are gathered and then decay to muons in the Delivery Ring before being sent to the  $g - 2$  storage ring. [37].

on the order of 10 billion positrons above threshold, and its final result was statistics limited. In order to reach the goal of 140 ppb, approximately 20 times that number of statistics needs to be gathered. Fermilab has the facilities to produce such a high number of polarized muons.

The Fermilab accelerator complex produces polarized muons for E989 in a number of stages. A map of the various relevant accelerator beam-line components is shown in Figure 2.8. Details of the full accelerator production of polarized muons can be found in Reference [40], and here a summary of the process will be given. First,

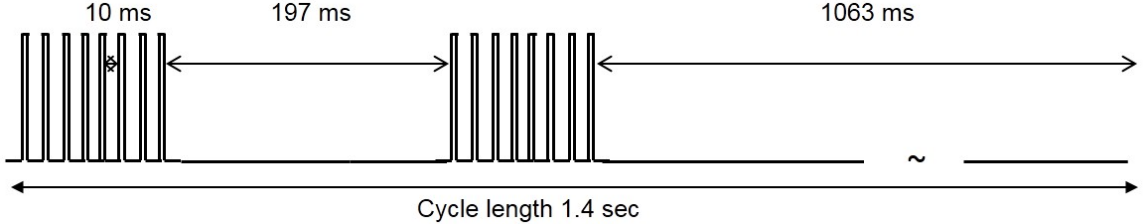


Figure 2.9: General timing structure of beam pulses sent to E989.

protons are generated and accelerated in a linear accelerator. They are transported to a 75 m radius circular ring called the “booster,” which accelerates them up to 8 GeV and batches them together. A single booster batch contains on the order of  $4 \times 10^{12}$  protons. The protons are then injected into a ring called “recycler,” which re-bunches them into four separate bunches of  $1 \times 10^{12}$  protons, each with a time width of approximately 120 ns. (This is less than the cyclotron period of the storage ring of 149 ns.) This rebunching process is done in order to reduce the level of pileup in the  $g - 2$  detectors, see Section 3.2.1. For a single accelerator supercycle of 1.4 s, E989 receives four booster batches of particles corresponding to sixteen bunches at an average rate of 11.4 Hz, with the time separation between bunches greater than 10 ms. The timing structure is shown in Figure 2.9. The sets of eight bunches are sometimes referred to as pulses, and the gathered data is tagged by which bunch or pulse it originates from. Depending on the accelerator requirements of other experiments, this timing structure is modified appropriately, though it is relatively constant.

Each bunch is selected one at a time and sent to a target hall, where it is directed on to an Inconel target. This Inconel target is made up of a nickel and iron alloy optimized for producing a large number of pions with a small momentum spread, approximately  $1 \times 10^{-5} \pi^+$  per proton on target with  $|dp/p| < 2\%$  [40]. The resulting pions are focused just after production by a lithium lens. This lithium lens is a 1 cm radius and 15 cm long piece of lithium designed to carry high current which provides a

radial focusing effect for particles passing lengthwise down the cylinder [41]. A pulsed magnet just after the lithium lens is then used to select pions centered at 3.115 GeV.

In a pion beam the highest and lowest energy decay muons are forwards and backwards polarized, respectively. The pion beam and any residual protons or secondaries are injected into another ring called the “delivery ring”. By the time the pions have gotten to the delivery ring, most of them have decayed to muons. The delivery ring is used to select the polarized muons and separate out the non-desired particles [40]. Forward emitted polarized muons are momentum selected at 3.094 GeV with  $\Delta p/p = 2\%$ . The remaining muons, protons, and other secondary particles are re-routed to a beam dump which reduces the contamination in the final polarized muon beam. This polarized muon beam is then sent to the  $g - 2$  building where it passes through four magnetic quadrupole focusing magnets before being injected into the storage ring.

## 2.4 Injection of muons

The injection of the muon beam into the  $g - 2$  storage ring is a specialized process. In order to measure the magnetic field to the precision described in Section 2.2, the  $g - 2$  storage ring must be a single monolithic magnet with no end effects. This prohibits the usual design of separated magnetic elements through which the muons might be injected. Therefore we use a specialized magnet called the “Superconducting Inflector” magnet, or just inflector. This inflector is placed just after a bored out tunnel in the storage ring magnet, on the inside of the C shape. See Figure 2.10 for a view of the injection point. The inflector has a very tight 18 mm wide by 56 mm high aperture through which the muons must pass down its 1.7 m length. The inflector is made up of superconducting coils wrapped in a double cosine theta design around an aluminum mandrel [42]. See Figure 2.11. This design serves to contain the majority

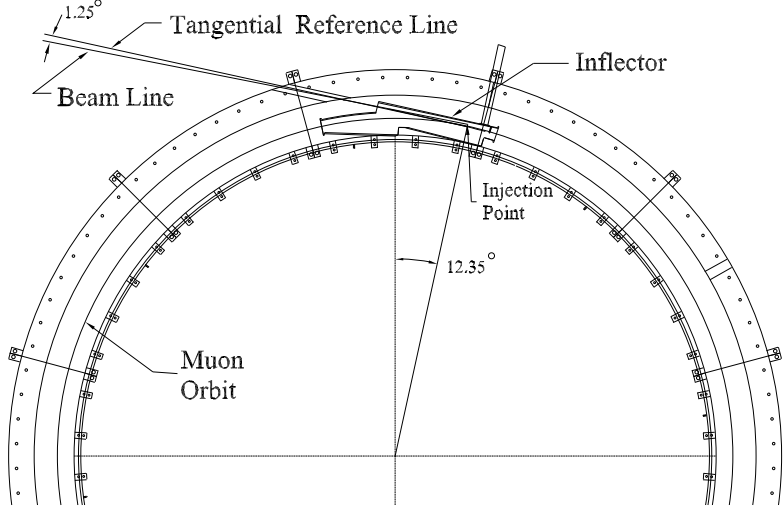


Figure 2·10: A plan view of the inflector and injection point into the storage ring [42].

of the inflector magnet field, while eliminating the the storage ring field for the muons passing down its length, such that they are not lost due to motion induced by said field. The inflector is contained within a superconducting shield which traps the fringe field of the inflector such that the storage ring magnet field is unaffected. As shown in Figure 2·11, both sides of the inflector are closed such that an appreciable fraction of muons are lost due to multiple scattering before being injected into the ring. A new inflector magnet is being designed with open ends in order to increase the muon flux for future runs of  $g - 2$  [37].

## 2.5 Storage of muons

The E989 experiment and storage ring are shown in Figure 2·12. Once the muons have been injected into the ring, they will begin orbiting clockwise around the ring, decaying with a lifetime of  $64.4\ \mu\text{s}$ . By necessity, the inflector must be out of the stored muon beam path, otherwise a large fraction of the muons would be lost upon the return to the injection point as the muons would strike the inflector. Therefore

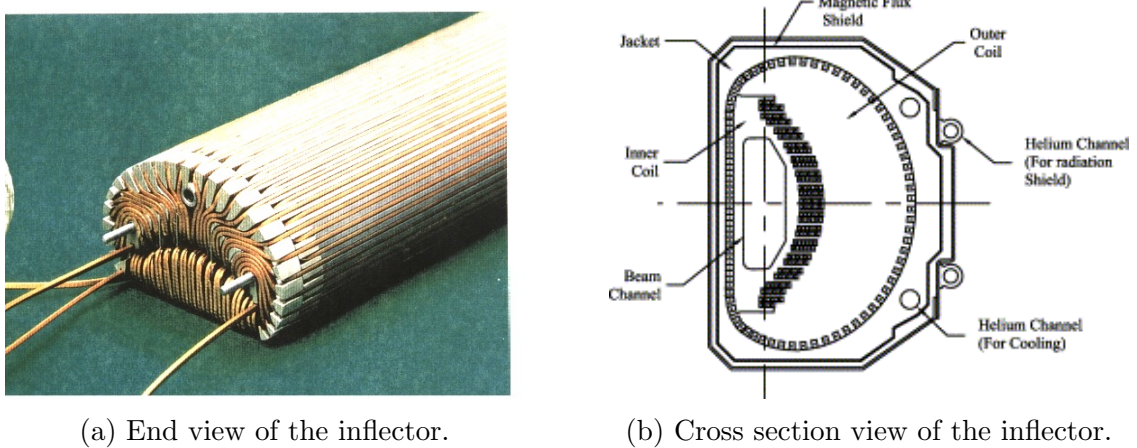


Figure 2.11: The inflector magnet (left) and a cross section view of the inflector windings and associated shield (right) [42].

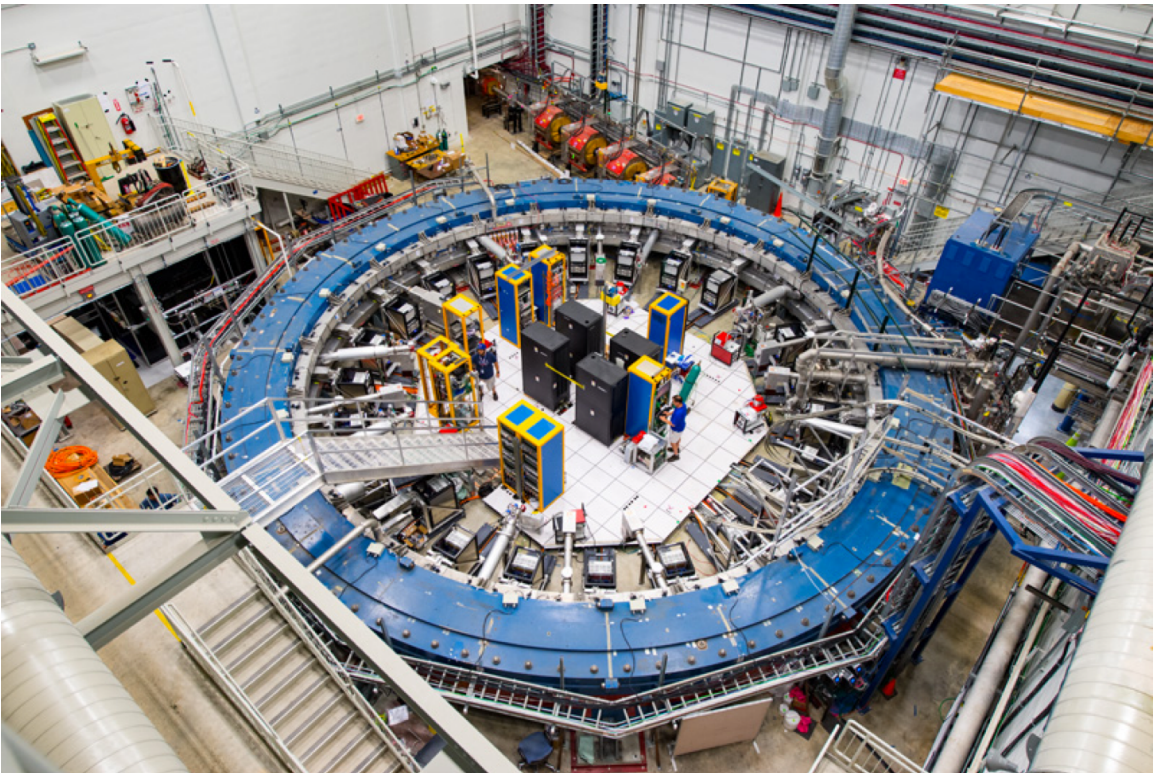


Figure 2.12: The E989 experiment. The blue painted storage ring can be seen to surround a variety of detectors and electronics. Muons come in at the top of the picture through a series of magnetic quadrupoles from the accelerator and are injected into the ring, where they orbit in a clockwise direction. There are some people located inside the ring which gives a sense of scale to the picture.

the muon beam must be manipulated to move the beam path from the injection orbit onto the central orbit of the storage ring. The muon beam must also be contained vertically. To perform the former, a magnetic “kicker” is used to shift the orbits of the muons. To perform the latter, a series of electrostatic quadrupoles focus the beam vertically. Approximately 2% of the injected muons are stored with  $\Delta p/p = 0.1\%$  centered around 3.094 GeV, corresponding to a design goal of  $\mathcal{O}(10,000)$  stored muons per fill.

### 2.5.1 Kicker

The kicker is made up of three separate pulsed magnets located  $90^\circ$  from the exit of the inflector, where the inflector orbit crosses the central orbit. The placement of the kickers is shown in Figure 2.13. The kicker must be located within the uniform magnetic field of the ring, and must therefore contain no magnetic elements in the hardware itself. For this reason each kicker magnet is made up of two thin 1.27 m long aluminum plates, separated by 10 cm, which carry the current used to create the kicking magnetic field. Due to the bunched nature of the muon beam and the short cyclotron period of 149 ns, ideally the kicker moves all stored muons onto the central orbit and then turns off quickly such that by the time the muons orbit back around to the kicker there is no residual kick to the beam. Any residual eddy currents must die away quickly enough such that the magnetic field seen by the stored muons is unperturbed. The design kick to the beam is approximately 10 mrad using a vertical pulsed field of around 300 Gauss (corresponding to kicker plate voltages of  $\mathcal{O}(155 \text{ kV})$ ) with a pulse length of about 120 ns [37]. The operational kicker performance in Run 1 was less, as described in Section 2.8.

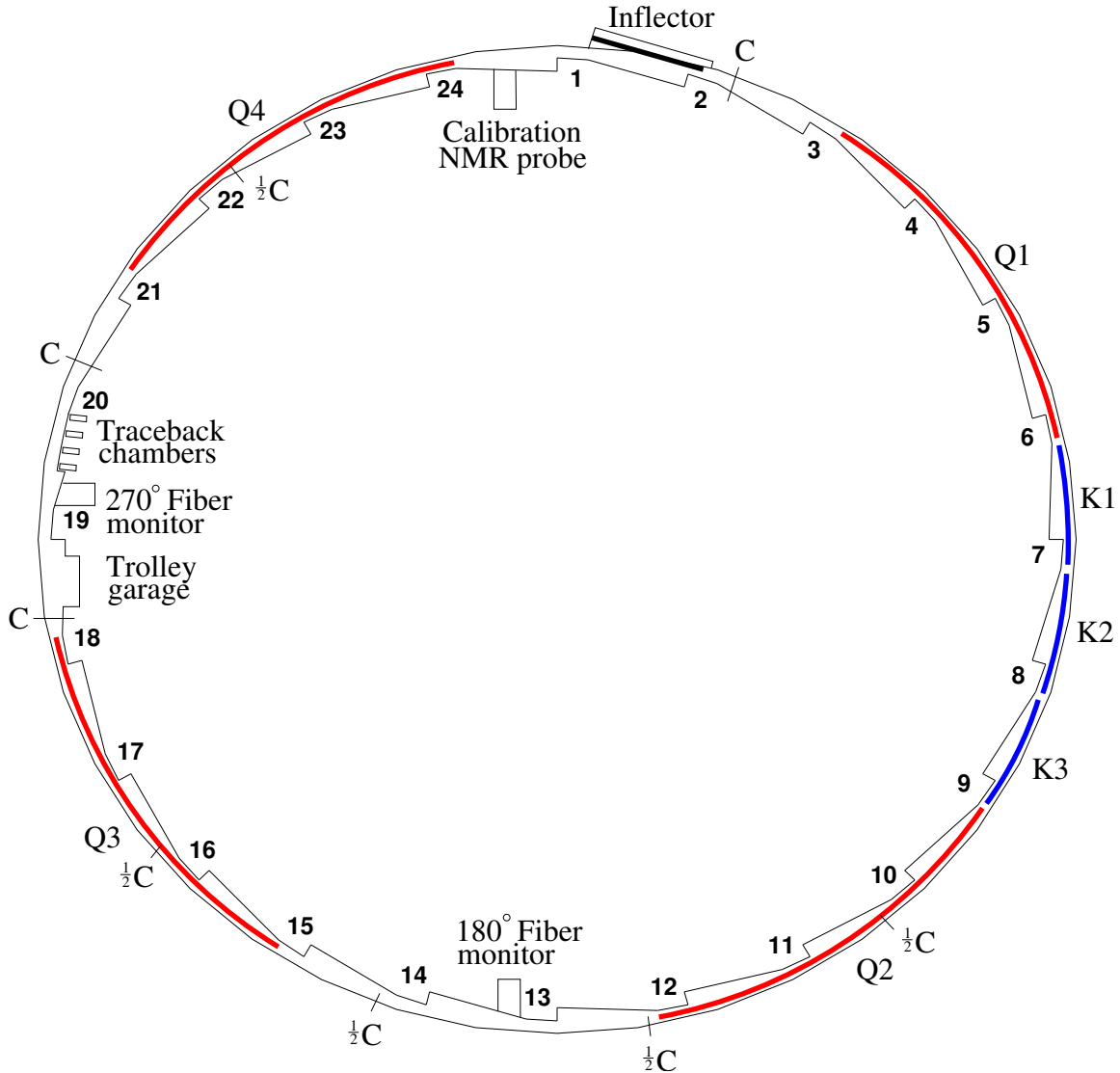


Figure 2·13: A map of the vacuum chambers in E989. K1-K3 show the locations of the kicker magnets, while Q1-Q4 show the locations of the electrostatic quadrupoles. Also shown is the location of the inflector, the two fiber monitors, and one of the tracker stations.

### 2.5.2 Electrostatic quadrupoles

There are four electrostatic quadrupoles (quads) located around the ring as shown in Figure 2.13, which focus the beam vertically and defocus the beam horizontally. (The magnetic field of the ring serves to restore the beam radially in combination with the electric field.) Just as with the kickers, the quads must be operated in vacuum. E989 uses electrostatic focusing elements instead of magnetic ones in order to avoid magnetic field gradients which would limit the precision of the magnetic field measurement. Four quads were chosen in order to maximize the symmetry of the beam motion around the ring [37]. The quads occupy 43% of the ring circumference, leaving space for other elements around the ring. Each quad is made up of two segments, a short segment of  $13^\circ$  and a long segment of  $26^\circ$  corresponding to 1.61 m and 2.62 m respectively, with each segment consisting of four plates. The quads are made out of as little material as possible in order to reduce multiple scattering of decay positrons passing through them. A picture of the quads installed into one of the vacuum chambers is shown in Figure 2.14. A simulation of the equipotential lines of the quads is shown in Figure 2.15. The original design of the quads is detailed in Reference [43].

Some of the stored muons will be lost during data taking that can adversely affect the measurement of the spin difference frequency  $\omega_a$ . See Section 5.3. In order to reduce the number of lost muons, a procedure called “scraping” is used to remove those muons sitting at the edge of the storage region that are more likely to be lost at later times. This scraping procedure involves powering the quad voltages in an asymmetric way such that the beam is pushed to the outside of the storage region, where the edges of the beam will intersect copper collimators. Muons which hit the collimators will lose energy and be lost as they spiral out of the ring. The scraping procedure is performed early in the fill and ends at 8  $\mu\text{s}$ , such that by 30  $\mu\text{s}$  the beam

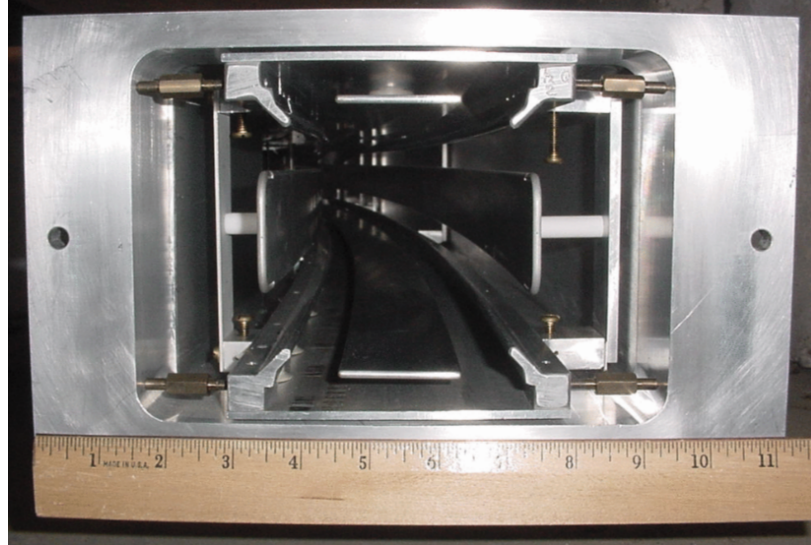


Figure 2·14: Electrostatic quadrupoles installed into a vacuum chamber [43]. There are four plates mounted to the chamber through insulator standoffs. Also shown are the rails that the magnetic field trolley rides on around the inside of the ring, and between the quad and kicker plates. The distance between opposing quad plates is 10 cm.

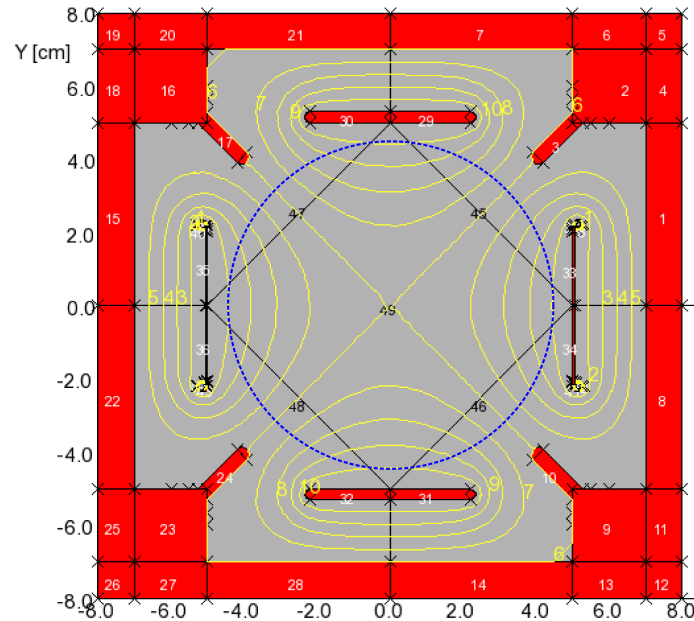


Figure 2·15: An OPERA model of the quads and their equipotential contours [37]. The top and bottom plates sit at positive voltage while the left and right plates are at negative voltage. The muon storage region is shown by the blue circle.

is stable and centered due to the characteristic RC time constant of the system. The operational performance of the quads in Run 1 is described in Section 2.8, where it was found that the quads had a longer RC time constant than the design.

## 2.6 Muon beam dynamics

Muons injected into the storage ring will occupy a region in phase space of momenta and positions defined by the injection and collimator apertures. Individual muons will undergo simple harmonic motion, or betatron oscillations, within the storage ring in both the vertical and horizontal directions. The horizontal ( $x$ ) and vertical ( $y$ ) equations of motion, including the effects of the discrete quadrupoles, are given by

$$x = x_e + A_x(s) \cos(\nu_x \frac{s}{R_0} + \phi_x), \quad (2.19)$$

$$y = A_y(s) \cos(\nu_y \frac{s}{R_0} + \phi_y), \quad (2.20)$$

where  $x_e$  is the radial equilibrium orbit of the beam relative to  $R_0$ ,  $A_x(s)$  and  $A_y(s)$  are the amplitudes of the motions containing the effects of the discreteness of the quads, and  $s$  is the arc length of the trajectory. Here  $\nu_x$  and  $\nu_y$  are the so-called horizontal and vertical “tunes” of the beam motion, which are ratios of the betatron frequencies to the cyclotron frequency  $f_c$ :

$$\begin{aligned} \nu_x &= f_{x_{BO}}/f_c = \sqrt{1-n} \\ \nu_y &= f_{y_{BO}}/f_c = \sqrt{n} \end{aligned} \quad (2.21)$$

These are related to the field index  $n$ , where the field index characterizes the strength of the electrostatic focusing in relation to the magnetic field strength:

$$n = \frac{\kappa R_0}{\beta B_0}, \quad (2.22)$$

Muon Beam Frequencies				
Name	Symbol	Expression	Frequency (MHz)	Period
$g - 2$	$f_a$	$a_\mu Be/2\pi mc$	0.23	4.365 $\mu$ s
cyclotron	$f_c$	$v/\pi R_0$	6.71	149 ns
horizontal betatron	$f_{x_{BO}}$	$\sqrt{1-n}f_c$	6.34	158 ns
vertical betatron	$f_{y_{BO}}$	$\sqrt{n}f_c$	2.21	452 ns
coherent betatron	$f_{CBO}$	$f_c - f_{x_{BO}}$	0.37	2.703 $\mu$ s
vertical waist	$f_{VW}$	$f_c - 2f_{y_{BO}}$	2.31	433 ns

Table 2.2: Frequencies seen in the  $g - 2$  experiment due to beam motion. Parameter values are from a subset of Run 1 corresponding to an  $n$  value of 0.108 or a quad voltage of 18.3 kV.

where  $\kappa$  is the electric quadrupole gradient,  $B_0$  is the magnetic field strength,  $R_0$  is the central storage ring radius, and  $\beta$  is the relativistic velocity of the muon beam. Technically  $n$  is the average field index around the ring, where this approximation is justified due to the four-fold symmetry of the discrete quadrupoles and the fact that the betatron oscillations have periods much greater than the length of the quads. A table of the important frequencies in E989 is shown in Table 2.2. Lastly, the maximum angular acceptance of the ring can be determined from the betatron oscillations and the field index as

$$\begin{aligned}\psi_{x_{max}} &= \frac{x_{max}\sqrt{1-n}}{R_0}, \\ \psi_{y_{max}} &= \frac{y_{max}\sqrt{n}}{R_0},\end{aligned}\tag{2.23}$$

where  $x_{max}$  and  $y_{max}$  are both equal to the radius of the storage ring aperture at 45 mm.

As the muon beam goes around the ring, the muons will experience local field gradients and inhomogeneities. The tunes are thus chosen to avoid resonances where muons might be lost from repeatedly passing through such perturbations. The muons within the ring should then sample the entire azimuth equally and remain stored. The

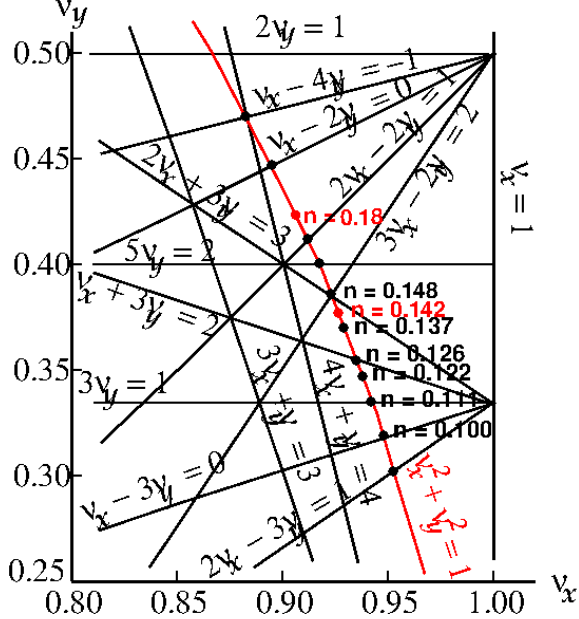


Figure 2.16: The tune plane, with the  $\nu_x^2 + \nu_y^2 = 1$  constraint in red. The chosen value of  $n$  lies on this circle. The original design goals for E989 were the  $n$  values as shown by the red points, but due to hardware issues smaller  $n$  values of 0.108 and 0.120 were chosen as described in Section 2.8.

general resonance condition is [44]

$$a\nu_x + b\nu_y = c, \quad (2.24)$$

where  $a$ ,  $b$ , and  $c$  are integers. We know from Equation 2.21 that

$$\nu_x^2 + \nu_y^2 = 1, \quad (2.25)$$

which constrains the available  $n$  values that can be chosen. Figure 2.16 shows the space relative to the tunes for which a chosen value of  $n$  will lie on a resonance. The operational  $n$  values and corresponding quad voltages in Run 1 are described in Section 2.8.

### 2.6.1 Coherent betatron oscillation

With each individual muon undergoing betatron oscillations, the muon beam as a whole will oscillate. The beam can be described as having a width and a mean dependent on the initial phase space parameters determined by injection and kicker effects. This overall distribution of the beam will oscillate coherently every betatron wavelength, thus moving around the ring at some frequency. Individual detectors around the ring measure the beam in discrete pieces based on their individual azimuthal acceptances, where these acceptances depend on the radial and vertical characteristics of the beam. Because the radial betatron frequency is larger than half the cyclotron frequency, there is an aliasing effect such that the radial betatron motion of the beam is instead observed as an apparent slow-moving oscillation. We call the measurable signal of this coherent radial motion coherent betatron oscillation (CBO). See Figure 2.17 for a pictorial view of this phenomena. The frequency of the CBO is just the beat frequency between the cyclotron frequency and the horizontal betatron frequency

$$f_{CBO} = f_c - f_{x_{BO}}. \quad (2.26)$$

There is also a vertical CBO effect, but the non-aliased rate of oscillation is fast enough such that the effect tends to average out. What can be seen in the data however is the vertical width of the beam, which is aliased in a similar way to the radial oscillation. Though the principles are the same, we call this effect the vertical waist (VW),

$$f_{VW} = f_c - 2f_{y_{BO}}, \quad (2.27)$$

where the term waist is used to describe the vertical width when its at its minimum. Both of these frequencies are included in Table 2.2. For an individual detector the

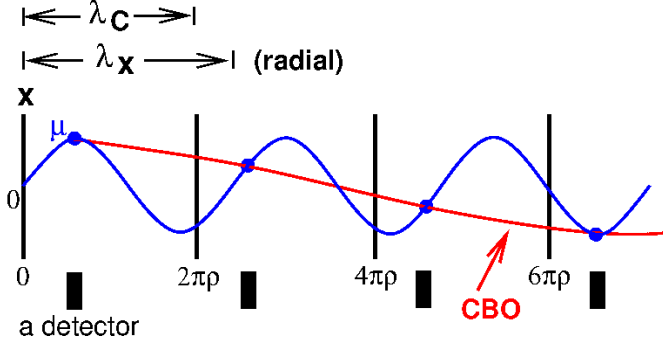


Figure 2.17: Marked by the black vertical lines are integer steps in the circumference of the ring, corresponding to the cyclotron wavelength  $\lambda_c$ . The blue line shows the motion of the beam due to the betatron oscillations  $\lambda_x$ . Since  $\lambda_x > \lambda_c/2$ , there is an aliasing effect in the observed signal, which is identified by the red line. The beam is thus seen as appearing to move back and forth with a slow oscillation, known as CBO.

CBO has a specific phase, which goes from 0 to  $2\pi$  around the ring. When adding all of the detector signals together, the CBO effect tends to cancel out. However, due to acceptance differences between the different detectors, the CBO effect is still observable in the data. When fitting the data to extract  $\omega_a$ , these effects need to be included as will be discussed in Section 5.4.1.

### 2.6.2 Beam debunching

As described in Sections 2.3 and 2.4, the muon beam is injected into the ring with a time spread of 120 ns and a range of momenta. At early times the beam will occupy a portion of the ring less than the whole since the cyclotron period is 149 ns. Therefore early in the fill the detectors located at discrete points around the ring will measure counts from the beam where there will be a fast oscillation in the signal due to this cyclotron period. As time increases throughout the fill, the momentum distribution of the muons will cause the beam to spread out within the storage ring until the entire azimuth is filled. Since almost all muons are at the same momentum, it turns out that the slower moving muons at smaller radii catch up to the faster moving muons at

the outer radii after many turns around the ring. By 30  $\mu\text{s}$  the muon beam has gone around the ring two hundred times. As the beam fills the storage ring, the cyclotron frequency in the data reduces and the beam is seen to debunch. This phenomena is referred to as the “fast rotation.” This debunching signal is seen in the data as shown in Figure 2.18. When dealing with the data and attempting to extract  $\omega_a$ , the typical procedure is to both bin out the fast rotation in periods of the cyclotron frequency, and to randomize each hit time by  $\pm T_c/2$  where  $T_c$  is the cyclotron period. In this way the fast rotation is removed entirely and the five parameter function described in Equation 2.14 remains satisfactory, barring other effects.

## 2.7 Corrections to $\omega_a$

Equation 2.3 is an idealized version of the spin difference frequency with no electric fields and motion perpendicular to the magnetic field. Including practical experimental concerns, there are two corrections that must be applied to  $\omega_a$ .

### 2.7.1 Electric field correction

In the presence of an electric field, the spin difference frequency is altered to

$$\vec{\omega}_a = -\frac{q}{m}[a\vec{B} - \left(a - \frac{1}{\gamma^2 - 1}\right)(\vec{\beta} \times \vec{E})], \quad (2.28)$$

where now there is an extra term dependent on the electric field strength and the momentum of the particles. This is necessary to include since we use electrostatic quadrupoles for vertical focusing as described above. The second term cancels to first order for a specific momentum or value of  $\gamma$ . This “magic momentum” can be understood as the momentum at which a relativistic particle moving through an electric field has its spin exactly follow its momentum. This magic momentum is 3.094 GeV for muons, hence the momentum value of the injected muons. This

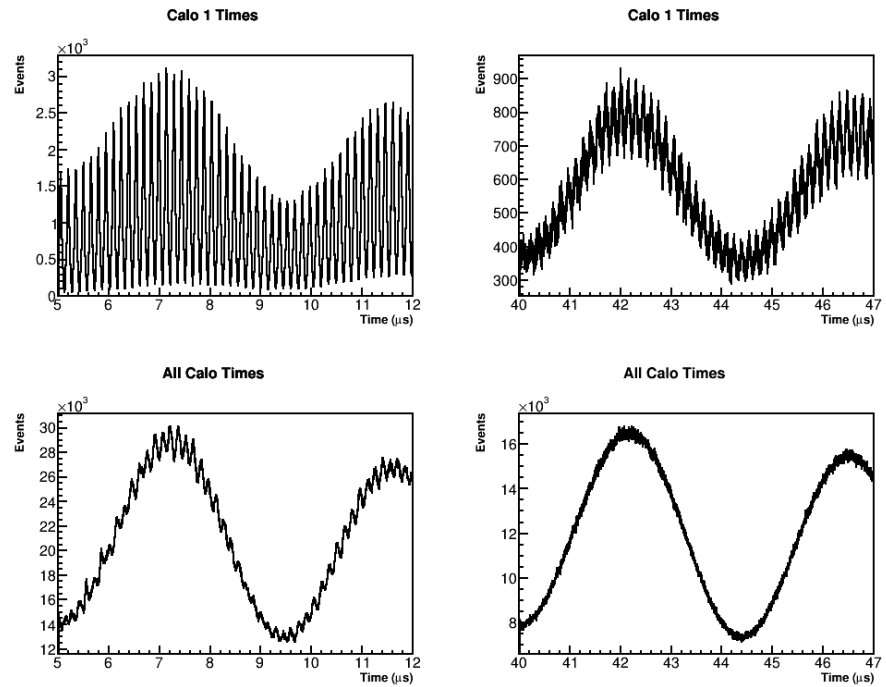


Figure 2.18: The fast rotation signal can be seen in the data as an oscillation with a period of 149 ns, corresponding to the fast oscillations in these plots. In individual calorimeters at early times the fast rotation signal is seen to be very large, as shown on the top left. As time passes and the beam debunches, the amplitude of the fast rotation signal diminishes as shown on the top right. When adding all calorimeters together, the signal reduces as shown in the bottom two plots. In all cases the slow oscillation is the  $g - 2$  frequency.

value sets the energy and time scales of the experiment and has driven many of the design constraints, including the size of the storage ring, choice of the magnetic field magnitude, etc.

Not all muons will have the magic momentum however as described in the Section 2.6.2, and therefore a correction to the measured  $\omega_a$  frequency needs to be applied. Approximating the storage ring as having an electric field applied over the whole azimuth of the ring, the spin difference frequency for muons with momentum  $p \neq p_m$  (where  $p_m$  is the magic momentum) becomes

$$\omega'_a = \omega_a \left[ 1 - \beta \frac{E_r}{cB_y} \left( 1 - \frac{1}{a\beta^2\gamma^2} \right) \right]. \quad (2.29)$$

Here the motion of the beam is assumed purely azimuthal. This additional term is the electric field correction that then serves to lower the measured  $\omega_a$  frequency. Using the relation  $p = \beta\gamma m = (p_m + \Delta p)$ , after a little bit of simplification the electric field correction can be written as

$$C_E = \frac{\Delta\omega_a}{\omega_a} = -2 \frac{\beta E_r}{cB_y} \frac{\Delta p}{p_m}. \quad (2.30)$$

The last fraction can be related to the field index described in Equation 2.22 by

$$\frac{\Delta p}{p_m} = (1 - n) \frac{\Delta R}{R_0} = (1 - n) \frac{x_e}{R_0}, \quad (2.31)$$

since we know that the magic momentum muons live at the center of the storage ring radius  $R_0$ . In this equation  $x_e = \Delta R$  is the equilibrium radius of the muon relative to the central storage radius. Noting that the electric field strength for a quadrupole is

$$E = \kappa x = \frac{n\beta c B_y}{R_0} x, \quad (2.32)$$

and assuming that it is perfectly radial, the electric field correction can be reduced to

$$C_E = -2n(1-n)\beta^2 \frac{xx_e}{R_0^2}. \quad (2.33)$$

Taking the time average of the beam motion, where  $x$  is simply equal to  $x_e$ , then the correction becomes

$$C_E = -2n(1-n)\beta^2 \frac{\langle x_e^2 \rangle}{R_0^2}. \quad (2.34)$$

Since the equilibrium radius of the beam is set by the momentum distribution of the muons, this electric field correction can be determined by a measurement of the momentum spread of the beam which comes from an analysis of the fast rotation [45, 46]. For the precision goal of E989, the assumptions made in this derivation are acceptable [37] and results will be cross-checked with spin-tracking simulations as was done in E821 [28]. In E821 the electric field correction was approximately 500 ppb on  $\omega_a$  [28]. In E989 the scale of the correction will be the same considering the experimental principles are identical.

### 2.7.2 Pitch correction

Particles injected into the  $g - 2$  storage ring will have some motion component that is vertical, or parallel to the magnetic field vector (hence the need for vertically focusing electrostatic quadrupoles). This will slightly reduce the magnetic field seen by the muons in their rest frame. Including this motion into the spin difference frequency,  $\omega_a$  becomes

$$\vec{\omega}_a = -\frac{q}{m} [a\vec{B} - a\left(\frac{\gamma}{\gamma+1}\right)(\vec{\beta} \cdot \vec{B})\vec{\beta}], \quad (2.35)$$

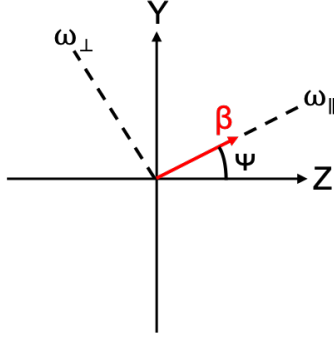


Figure 2.19: Beam motion  $\beta$  relative to the vertical and azimuthal axes Y and Z respectively.  $\psi$  is the pitch angle of the beam, and the dashed lines represent the parallel and perpendicular motions of the beam.

where now there is an extra term dependent on the vertical betatron motion of the beam. Similar to the electric field case, this term can be neglected to first order as the muon momentum is nearly all perpendicular to the field, but a correction again needs to be applied to  $\omega_a$  to account for this effect.

Since the muons in the storage ring will be oscillating vertically as they are focused by the quads, their momentum vectors will be pitching up and down relative to the azimuthal motion. This pitch angle will oscillate as

$$\psi = \psi_0 \cos(\omega_y t), \quad (2.36)$$

where  $\psi_0$  is the amplitude of the oscillation and  $\omega_y$  is the vertical betatron frequency. Shown in Figure 2.19 is an exaggerated example of the beam motion relative to the vertical and azimuthal axes. Assuming that the field is purely vertical,  $\vec{B} = B_y \hat{y}$  and that the beam motion is in the vertical-azimuthal plane,

$$\vec{\beta} = \beta_y \hat{y} + \beta_z \hat{z} = \beta \sin(\psi) \hat{y} + \beta \cos(\psi) \hat{z}, \quad (2.37)$$

then  $\omega_a$  becomes

$$\vec{\omega}_a = -\frac{q}{m}[aB_y\hat{y} - a\left(\frac{\gamma}{\gamma+1}\right)\beta_yB_y(\beta \sin(\psi)\hat{y} + \beta \cos(\psi)\hat{z})]. \quad (2.38)$$

Using the small angle approximation such that  $\cos(\psi) \approx 1$  and  $\sin(\psi) \approx \psi$ ,  $\vec{\omega}_a$  can be separated into its vertical and azimuthal components

$$\omega_{ay} = \omega_a \left[ 1 - \left( \frac{\gamma-1}{\gamma} \right) \psi^2 \right], \quad (2.39)$$

$$\omega_{az} = -\omega_a \left( \frac{\gamma-1}{\gamma} \right) \psi. \quad (2.40)$$

Looking at Figure 2.19 again, it can be seen that the spin difference frequency can be resolved into its parallel and perpendicular components  $\omega_{\parallel}$  and  $\omega_{\perp}$  respectively. As the pitch angle of the beam motion oscillates about the azimuthal axes at a frequency much greater than the  $g - 2$  frequency, it can be seen that the parallel component averages to 0 over time. We then only care about the perpendicular oscillation of the beam, which can be determined with a simple rotation matrix such that

$$\omega_a \approx \omega_{\perp} = \omega_{ay} \cos(\psi) - \omega_{az} \sin(\psi) \approx \omega_a \left[ 1 - \frac{\psi^2}{2} \right], \quad (2.41)$$

where in the last approximation the small angle approximation was used once again, but this time with  $\cos(\psi) \approx 1 - \psi^2/2$ . The pitch correction then is the additional term which serves to lower the measured spin difference frequency. Taking the time average,

$$C_P = \frac{\Delta\omega_a}{\omega_a} = -\frac{\langle \psi^2 \rangle}{2}. \quad (2.42)$$

The pitch angle of the beam cannot be measured directly, however we know from Equation 2.23 that the angle of the beam can be related to the vertical distribution

of the beam, such that

$$C_P = -\frac{n}{2} \frac{\langle y^2 \rangle}{R_0^2}. \quad (2.43)$$

Once again  $n$  is the field index,  $R_0$  is the radius of the ring at the center of the storage region, and  $\langle y^2 \rangle$  is the vertical width of the beam. The first two are known and the last can be measured experimentally. Just as in the case of the electric field correction, the assumptions made in this derivation are acceptable for the precision goal of E989, and results will be cross-checked with spin-tracking simulations. In E821 the pitch correction was approximately 300 ppb on  $\omega_a$  [28], and the scale for the E989 correction will be the same.

## 2.8 Run 1 in E989

Run 1 for E989 was conducted in the first half of 2018. Production data was gathered from March 22nd through June 29th. Because of accelerator, experimental, and practical concerns production data taking was interrupted at various dates. Due to hardware issues both kicker and quad voltages were originally lowered from their technical design values. Various voltage set points for both systems were identified and used in separate periods of the data taking, depending on the stabilities of the systems. The distinct designated datasets gathered by E989 and their associated parameters are shown in Table 2.3.

Due to the lower kicker voltages, the muon beam was stored on a central radius  $\sim 6$  mm offset from the central orbit of the storage ring, as shown in Figure 4.23. The chosen quad  $n$  values were 0.108 and 0.120<sup>1</sup>, corresponding to quad voltages of 18.3 and 20.4 kV respectively [47]. During Run 1 it was discovered that some of the quad resistors were damaged, leading to longer RC time constants such that the

---

<sup>1</sup>The associated betatron wavelengths are 1.06 and 3.04 times the circumference of the storage ring respectively.

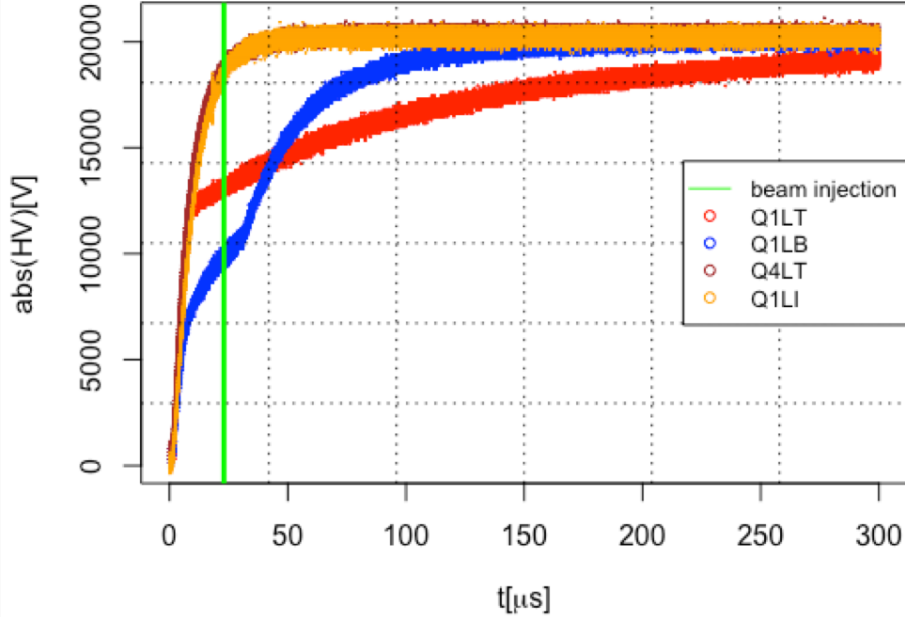


Figure 2.20: Traces for the high voltages as a function of time on some of the quad plates. The different plates are identified in the legend, where for instance Q1LT stands for the top long plate of quad 1. The beam is injected at the green line and the scraping procedure occurs until the quad voltages reach their design values, in this case 20.4 kV. As shown some of the high voltage traces do not behave in a smooth and fast exponential manner, due to damaged quad resistors. The traces in orange and brown are for good quad resistors, while the traces in red and blue show the results from damaged quad resistors.

quad voltages had not reached storage nominal at the beginning of the designated analysis portion of the data at 30  $\mu$ s, and were still changing over the course of a fill. See Figure 2.20. The muon beam was therefore seen to move as a function of time in-fill. See Section 4.4 for a summary of the muon beam characteristics for Run 1. As described in various sections in this chapter and in Section 4.4, these muon beam characteristics fold into the measurement of  $g - 2$  in a variety of ways, for which work is still on-going. The associated number of stored muons per fill for Run 1 as a result of these effects combined with injection was  $\mathcal{O}(4,000)$ , down from the  $\mathcal{O}(10,000)$  design goal.

All data listed in Table 2.3 was quality checked. If run conditions were found to be unstable or wrong in some way, the associated data was flagged and ignored in the analysis. A summary of the data quality control procedure is given in Reference [48], and the exact data quality parameters for the 60H dataset is detailed in Reference [49]. The total number of detected positrons above threshold that passed the data quality control was approximately  $1 \times 10^{10}$ , corresponding to a statistical error on  $\omega_a$  of  $\sim 400$  ppb, as calculated with Equation 2.17. See Chapter 6 for the final value for  $\omega_a$ .

Run 1 Datasets					
Name	Number $e^+ > E_{\text{Th}}$	$n$	Value	Quad Voltage (kV)	Kicker Voltage Range (kV)
60H	$9.3 \times 10^8$	0.108	18.3	128 – 132	0.37
HighKick	0.120	20.4	20.4	136 – 138	
9d	$2.2 \times 10^9$	0.120	20.4	128 – 132	
LowKick	0.120	20.4	20.4	123 – 127	
SuperLowKick	0.108	18.3	18.3	117 – 119	
Endgame	0.108	18.3	18.3	122 – 127	
Total Positrons Above Threshold					

Table 2.3: The different designated datasets acquired during Run 1 of E989 and their associated parameters [50]. Update the number of positrons column once all of the datasets have been opened and energy thresholds chosen. Potentially also add further columns of interest or split into multiple tables.

# Chapter 3

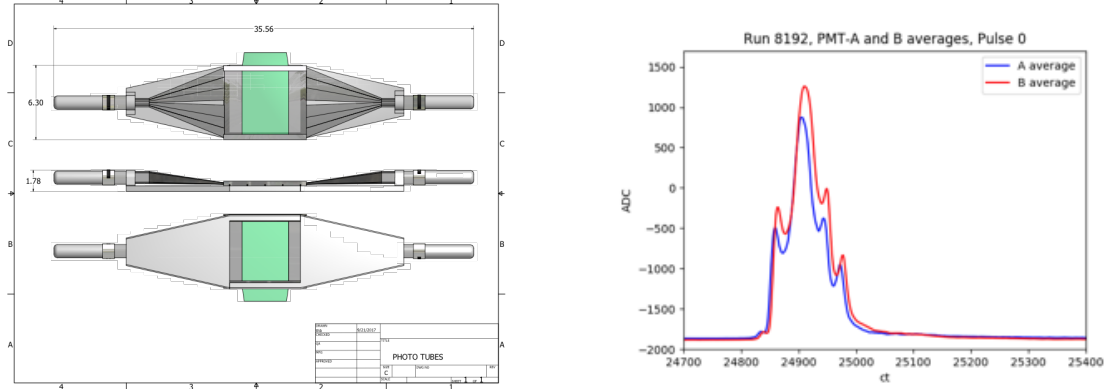
# Detector Systems

There is a variety of different detector systems used in E989. The primary detectors are the calorimeters which measure the  $\omega_a$  signal. In support of that measurement there are several auxiliary systems used for monitoring injection and beam dynamics. These include the T0, IBMS, and fiber harps. There is also a straw tracking detector which measures decay positron trajectories which can be related to muon beam dynamics and calorimeter measurements. Each of these systems will be described in the following sections.

## 3.1 Auxiliary detectors

### 3.1.1 T0

During data taking, a reference time must be chosen so as to align all different detector systems in time. When taking data from fill to fill, decay positron spectra must be aligned in phase. Without this functionality, analyzing the data from different systems and comparing them would be impossible. To do this a “T0” counter is placed just on the outside of the ring before the inflector. It is made up of a scintillating paddle connected to two photo-multiplier tubes (PMTs) [51, 52]. See Figure 3·1a. One PMT, PMT A, has a 1% neutral density filter resulting in low photo-electron statistics, and acts primarily as a timing measurement. The other, PMT B, has a 10% neutral density filter resulting in higher statistics, and acts as a shape counter and proxy for fill intensity. (In general the signals are very similar.) Together they provide a



(a) The T0 counter is made up of a scintillator in the middle shown in green, which connects with light guides to PMTs on the left and right.

(b) Time profiles for the two PMTs in the T0 counter for one of the eight bunches we receive at a time as described in Section 2.3. Each profile is an average of 100 such profiles. The x axis is in clock ticks, each of which is 1.25 ns.

Figure 3.1: A model of the T0 detector (left) and the signal it measures per fill (right).

measure of the injected beam profile in time, allowing to align the detectors each fill, and the data from fill to fill. Some measured T0 pulses are shown in Figure 3.1b. The shape of the incoming pulses has a somewhat trident-like shape, with a very large spike in the middle of the time width, and two spikes on the outside edges. This shape owes itself to the accelerator complex, and varies from bunch to bunch.

### 3.1.2 Inflector Beam Monitoring System

While the T0 provides timing and intensity measurements, the inflector beam monitoring system (IBMS) provides measurements of the beam position properties as it passes through the inflector. This is useful because the injection aperture is so tight, and incoming beam parameters are tightly constrained. The IBMS system serves to provide a direct diagnostic handle on the phase space matching between the last accelerator components and the  $g - 2$  storage ring, helping to optimize the number of stored muons per fill [53]. The IBMS is made up of two scintillating fiber detectors,

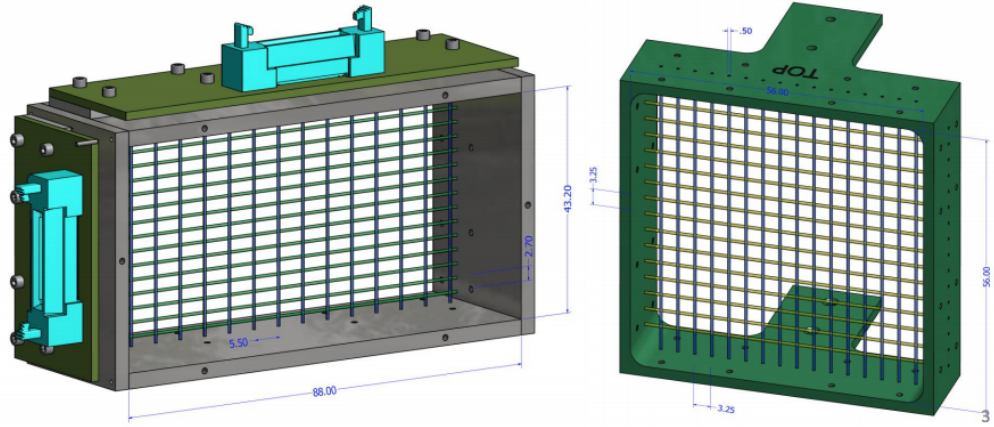


Figure 3.2: Models of the IBMS 1 and 2 detectors. Scintillating fibers form an array which detect particles as they pass through them.



Figure 3.3: The positions of IBMS 1, 2, and the planned 3rd device are shown with respect to the vacuum chamber and inflector.

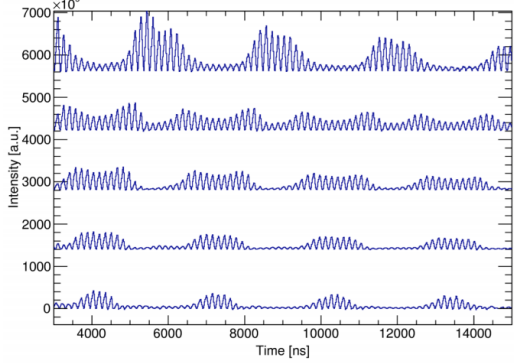
as shown in Figure 3.2. These devices are placed at the outside of the magnet yoke before injection into the back hole of the magnet, and at the entrance to the inflector [54]. A third device is planned to be at or near the downstream end of the inflector. See Figure 3.3.

### 3.1.3 Fiber harps

The last auxiliary detector is the so called “fiber harp” system. It is made up of four scintillating fiber detectors located within the ring that serve to measure the beam intensity as a function of time and position [55]. Two of the detectors measure the ra-



(a) Picture of one of the fiber harps. A row of seven scintillating fibers measures the beam intensity as a function of time at vertical or horizontal positions depending on which fiber harp is inserted.



(b) Shown are fiber harp beam intensity measurements for the horizontal fiber harp. Each spectra is from a single fiber, with the spectra at the top being at the greatest radial positions. The fast oscillations of the cyclotron frequency can be seen along with the slower oscillations of the CBO.

Figure 3·4: Fiber harp detector (left) and a sample of fiber harp measurements (right). **Figure out how to move left picture up, or maybe rethink this figure entirely.**

dial components of the beam, and two measure the horizontal components. The fiber harps are located at positions  $180^\circ$  and  $270^\circ$  clockwise from the inflector. One of these devices is shown in Figure 3·4a. The fiber can measure beam properties throughout the fill, providing a diagnostic tool which is sensitive to the scraping procedure and the CBO properties of the beam. An example of fiber harp measurements is shown in Figure 3·4b. However because the fiber harps are a destructive measurement of the beam due to multiple scattering in the fibers, the system was designed to be retractable. They are inserted during special diagnostic or systematic runs, and are pulled out of the beam path during production data taking.

## 3.2 Calorimeters

Electromagnetic calorimeters are the primary detector in the E989 experiment, responsible for the  $\omega_a$  measurement. They measure hit times and energies of decay positrons as they curl inward from the storage region.

### 3.2.1 Requirements and systematic effects

In order to determine  $\omega_a$  to the precision goal, there are specific requirements on the performance of the calorimeters. First, they must have a relative energy resolution of better than 5% at 2 GeV, in order for proper event selection above threshold [37]. The energy resolution requirement is modest but not strict because the important observable is the number of detected positrons above some energy threshold, where the optimal energy threshold can be determined empirically.

Second, they must have a timing resolution of better than 100 ps for positrons with energy greater than 100 MeV [37]. The calorimeters must be able to resolve multiple incoming hits through temporal or spatial separation at 100% efficiency for time separations of greater than 5 ns, or 66% of hits for time separations less than 5 ns, in order to reduce the pileup systematic effect. Pileup is the term used for when multiple particles impact the detector within the deadtime of the detector such that they are registered as a single hit. Unresolved pileup means that the number of detected positrons above threshold is mis-measured. Since pileup is a time-dependent effect, where pileup decays at some lifetime approximately equal to half the muon lifetime, this leads to a mis-measurement of  $\omega_a$ . The requirements stated here assist in reducing the pileup systematic error below a target goal of 40 ppb.

Third, the energy response of calorimeters for measured hits must be stable to  $< 0.1\%$  over a fill (700  $\mu$ s) [37]. The long term energy response stability over a time period of order seconds must be  $< 1\%$ . The energy response of a detector as a

function of time is typically referred to as the gain of the detector, where technically the gain refers to the amount of current output per detected hit. The gain depends on the temperature stability and hit rate. After a hit, the measured energy fraction of a following hit drops sharply and then rises exponentially back to one. This is referred to as the short-term double pulse (STDP) effect. At injection many particles are injected into the ring and there is a large amount of secondary particles incident in the calorimeters. The accumulation of all the individual STDP effects ends up causing a large gain drop at the beginning of each fill. This is typically referred to as the in-fill gain (IFG) effect. Hits with mis-measured energies due to these effects can thus be excluded from the fitted histogram if their energies drop below threshold, leading to another systematic effect and subsequent error in the  $\omega_a$  measurement. (Temperature changes vary over time scales greater than a fill, so don't contribute to the systematic error.) The requirements stated here, along with the use of a laser calibration system (Section 3.2.3), assist in reducing the gain systematic error below a target goal of 20 ppb.

### 3.2.2 Harware

There are 24 calorimeters located symmetrically around the inside of the ring placed flush to the vacuum chamber wall, as shown in Figure 3.5a. (Indeed the shape of the vacuum chambers were designed so as to reduce multiple scattering of the decay positrons before entering the calorimeters.) Each calorimeter sits on a board extending out from a cart which contains the electronics that power the calorimeters and read out the data. The carts help to relocate magnetic materials away from the field region to avoid perturbing the magnetic field, and provide easy access to the electronics while removing them from the positron decay path region.

Each calorimeter consists of 54 channels of  $\text{PbF}_2$  crystals arrayed in a 6 high by 9 wide array, for a total of 1296 channels. Each crystal is  $2.5 \times 2.5 \times 14 \text{ cm}^3$  and



(a) In black are the calorimeter carts, which house the electronics for the calorimeters. They hold up a board upon which the calorimeter rests. The calorimeter as shown is pushed flush to the vacuum chamber on the left.

(b) Shown is the backside of a calorimeter. The clear blocks are the PbF<sub>2</sub> crystals, each of which has a SiPM mounted onto the back of them.

**Figure 3.5: Calorimeter systems relative to the vacuum chamber (left) and an individual calorimeter (right). probably update these pictures at some point**

is wrapped in black Tedlar® foil. The PbF<sub>2</sub> material has an index of refraction of 1.8, and emits Cerenkov light as incident positrons with energy greater than 100 keV pass through the crystals [56]. Cerenkov light is naturally fast which improves the timing resolution of the incoming hits. The high density of the PbF<sub>2</sub> gives it a short radiation length, such that the energy deposition from the incident positrons is nearly 100% over the length of the crystal. The black foil is used to reduce light transmission between crystals and improve position reconstruction, as well as reduce pulse width [57]. The energy deposition from the incident positrons is typically restricted to only one or two crystals. The segmentation of the calorimeter combined with the black wrapping helps the spatial and temporal resolution of the detected pulses. See Figure 3.5b for a picture of the calorimeter crystals.

Each crystal is paired with a large area silicon photo-multiplier (SiPM) sensor which reads out the emitted Cerenkov light. SiPMs are compact, operable in high

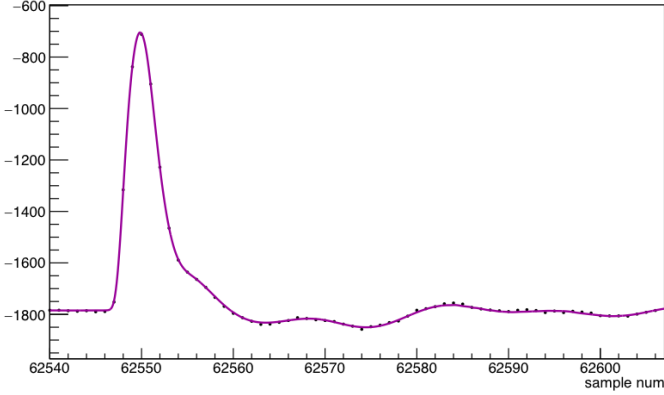


Figure 3.6: Output pulse from a SiPM in black dots, overlayed with a fit template.

magnetic field regions, have very linear responses for operation at MHz rates, are suited to measuring Cerenkov light due to their high photo-detection efficiency in the wavelengths of interest, and have a high degree of gain stability [57]. The SiPMs used are designed by Hamamatsu and detailed in Reference [57]. They sit on printed circuitry boards (PCBs) devoid of magnetic materials, which are designed to preserve the fast SiPM pulse shape. The combined properties of the chosen SiPMs, their electronic boards, and the  $\text{PbF}_2$  crystals results in an energy resolution of  $(4.6 \pm 0.3)\%/\sqrt{E/\text{GeV}}$ , a timing resolution of 20 ps, and a pulse width of 5 ns, satisfying the stated requirements earlier [56, 57]. Details of the pulse fitting algorithms are shared in Section 5.1. The SiPMs can be seen in Figure 3.5b. Finally, 12-bit waveform digitizers (WFD) sample each SiPM channel at a rate of 800 mega-samples per second with a 1 Gb memory buffer and the data are transferred to a bank of GPU processors for on-line data processing [58]. The timing resolution of these WFDs is  $< 50$  ps for most pulse amplitudes. A typical pulse from an incident positron is shown in Figure 3.6.

### 3.2.3 Laser calibration system

In order to satisfy the gain requirements of the calorimeter detectors, a laser calibration system is used. This system monitors the SiPM responses over short and long time scales to  $< 0.04\%$  [59]. The system consists of six different lasers and a suite of optical devices. The light from the six lasers is piped to a board mounted on the front face of each calorimeter through optical fibers. This board contains right-angle prisms which it uses to deflect the laser pulses directly into each calorimeter crystal, for all 1296 channels. The lasers can be pulsed at various intensities, both in-fill to monitor the STDP or IFG effects, and out-of-fill to monitor for long term drifts due to changing temperatures or detector degradation. The SiPM measured response is compared to local known source monitors in order to calibrate the SiPM energy response. Corrections to the gain of the calorimeters can thus be determined and applied to the hit energies. Simultaneously the laser system allows for measuring the timing resolution of the SiPMs, and in general performing diagnostic tests with the calorimeter. Lastly, the laser system is used to time align the different calorimeter channels by outputting a sync pulse to each channel at the beginning of every muon fill.

## 3.3 Straw trackers

As described in Section 2.6, the muon beam moves as a whole within the storage ring. As explained in Section 2.2, the muon beam distribution ties into the measurement of the magnetic field. The primary detector system used to measure this behavior and determine the muon beam distribution is the “straw tracker” system. The straw trackers characterize the beam in a non-destructive fashion by measuring decay positron trajectories and extrapolating them back into the storage ring. They serve to provide the direct measurement of the pitch correction as described in Section 2.7.2,

determine the momentum distribution of the beam, and characterize parameters of the CBO which tie into the calorimeter  $\omega_a$  analysis. Decay positron trajectories can also be extrapolated forwards into the calorimeter, in order to cross-check calorimeter measurements to help resolve pileup. Finally, the trackers also serve as a measuring device to search for a possible muon electric dipole moment. The existence of such a thing would tilt the precession plane of the muons and subsequent decay positron trajectories which the trackers are sensitive to. Details of the beginnings of such a search are given in Reference [60]. The details of the track reconstruction and analysis will be given in Chapter 4. Here will be given a description of the detectors themselves and how they work.

In general, straw tracking detectors work by measuring hits in gas filled straws [61]. Each straw is made up of a cylindrical piece of thin conducting material, typically Mylar, and contains a wire at the center of the straw held at high voltage,  $\mathcal{O}(1000\text{ V})$ . The minimal amount of material in straw trackers serves to reduce multiple scattering of incident particles, and was the reason a straw tracker system was chosen over other tracker types. Fast moving particles ionize the gas as they pass through it, and the resulting ions are drawn to the wire and straw surface (positive and negative charges respectively). As the ions move to the wire, they enter a high electric field region which causes them to speed up, hit other gas molecules, and create more ions. This produces an avalanche gain effect which amplifies the original signal. Once the ions reach the wire and straw surface, a signal is read out telling what the drift time of the ions was, which can be related to the radius or distance of closest approach (DCA) the particle passed relative to the wire. The straws therefore measure drift circles in a plane perpendicular to their physical orientation. The calculations of these DCA's and their errors is done using a simulation program for gaseous detectors called Garfield [62, 63]. By combining several such measurements in time and space, we are

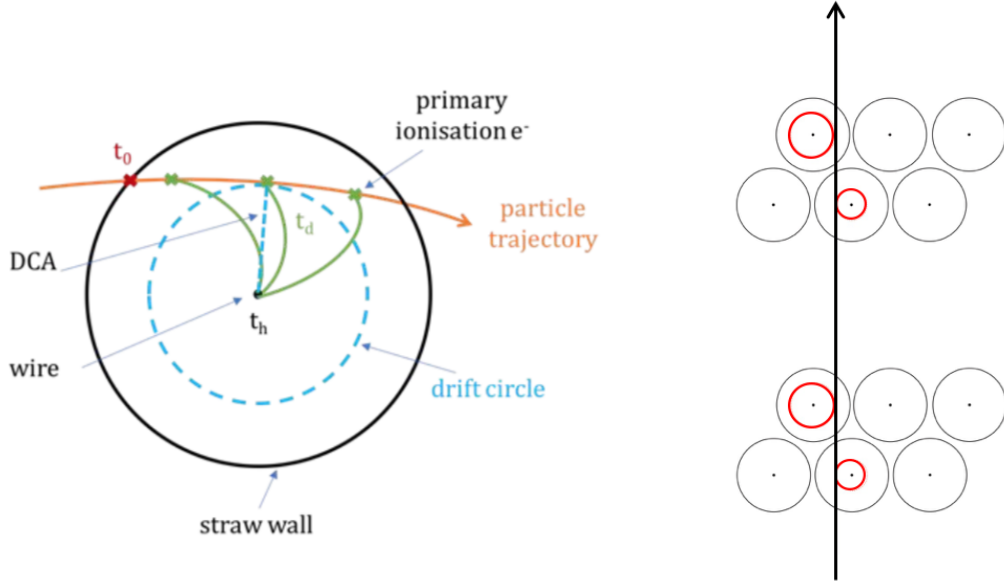


Figure 3.7: Diagrams showing the determination of a drift time  $t_d$  and hit time  $t_h$  from an incident ionizing particle (left) and the combination of several such hits to produce a track (right). Diagram on left courtesy of Saskia Charity.

able to reconstruct tracks of incident particles. See Figure 3.7.

Our straws are 5 mm in diameter and contain a 50:50 mixture of argon-ethane gas [64]. The argon component serves as the gas to be ionized. The fast moving ions near the wire in addition to producing more ions, will incite excited states of the gas, which emit photons when de-excited. These photons can restart the whole ionization and avalanche process over again as they can escape the avalanche region, leading to a break-down of the system. The ethane therefore serves to absorb the photons with its large number of molecular degrees of freedom and photo-absorption characteristics [64]. The wire has a radius of 25  $\mu\text{m}$  and is made up of gold-plated tungsten. The Mylar walls have a width of 15  $\mu\text{m}$  and are wound in a double spiral shape in order to improve the electrostatic shielding of the wire and reduce the gas leak rate of the straws [64]. The DCA resolution of hits within the straws is approximately 120  $\mu\text{m}$  to 150  $\mu\text{m}$ .

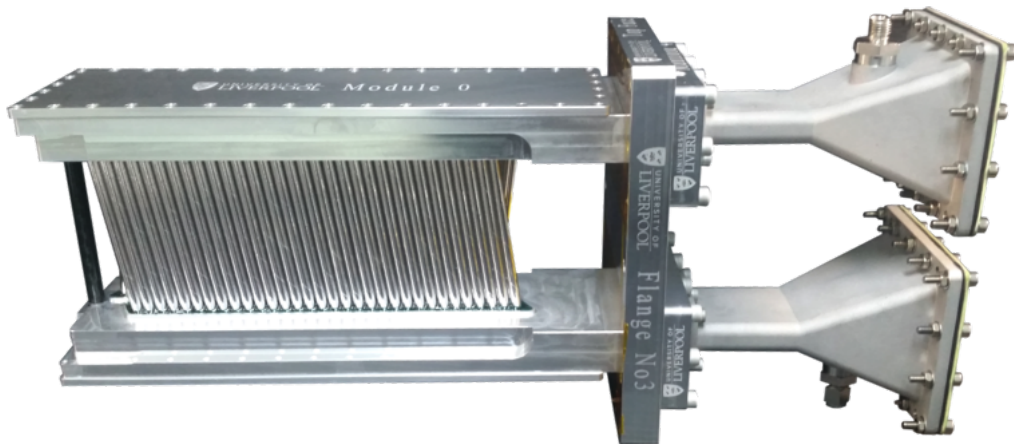


Figure 3·8: A straw tracker module. The first layer of silver Mylar straws with a stereo angle of  $7.5^\circ$  can be seen, with the other three straw layers hiding behind it. In black on the left is the carbon fiber post which holds the end of the module in a fixed position. Electronics live in the top and bottom manifolds above and below the straws, and cables connect from those electronics through small apertures to external electronics which plug in on the right.

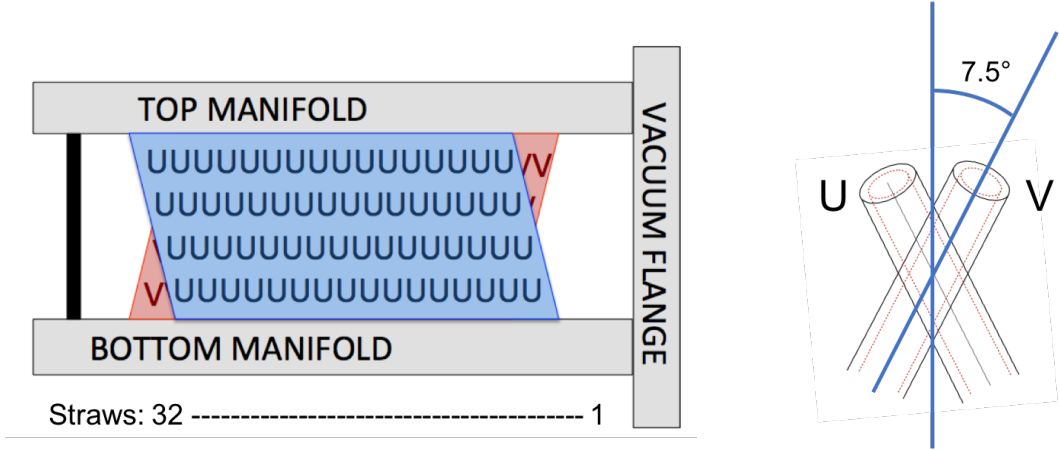


Figure 3.9: Orientation of U and V straws in the tracker module.

A single tracker module is shown in Figure 3.8. Each tracker module consists of 4 layers of 32 straws each with stereo angles of  $\pm 7.5^\circ$ , for a total of 128 straws per module. The first two straw layers are designated as “U” layers, and are oriented with the tops of the straws at a greater radial position than the bottoms of the straws. The second two layers are designated as “V” layers, and are oriented with the bottoms of the straws at a greater radial position than the tops. Both U or V layers are collectively referred to as the U and V views of the module respectively. See Figure 3.9. The two layers in each view are shifted half a straw diameter horizontally from one another in order to help resolve which side of the wire any incident particles passed, Section 4.2.6. The two types of layers are non-parallel to each other in order to resolve incident tracks in 2D space. The small stereo angle both improves the straw measurement area as electronics can be kept out of the positron decay path region, and improves the radial momentum resolution of the fitted tracks, since both views measure mostly in the horizontal plane. The active straw measurement area is approximately 10 cm high by 20 cm wide. A carbon fiber post sits at the outside end of the module to provide structural rigidity to the module, and keep the straw wires under tension.

There are two tracker stations, each consisting of eight tracker modules. The two stations live at positions in front of calorimeters 13 and 19, or at approximately  $180^\circ$  and  $270^\circ$  clockwise from the inflector. These are designated as Tracker Station 12 and Tracker Station 18 respectively, where the numbers come from which vacuum chamber the trackers reside in. There is also a third station just after the inflector, which currently sits empty of any tracker modules. The straw tracker modules sit inside the vacuum chamber in specially modified vacuum chamber sections in a staircase-like pattern that follows the curvature of the ring. See Figure 3.10. The number of modules and their orientation in each station was chosen to provide a long measurement arm for precise momentum measurement of the incident tracks. The modules sit inside the vacuum in order to eliminate multiple scattering in air and produce better reconstructed tracks. Due to their proximity to the storage region, the tracker modules also live in a region of high field non-uniformity. Though the acceptances between the trackers and calorimeters are not identical, their close proximity facilitates comparison between the two measurement devices. Finally, even though the tracker stations live at only two places in the ring, they measure the average beam distribution due to the CBO motion of the beam and the long extrapolation distance of the measured trajectories.

### 3.3.1 Tracker readout electronics

The readout electronics for the system are split into two groups, the front-end and back-end. The front-end electronics were built and tested at the Boston University Electronic Design Facility. They start with Amplifier Shaper Discriminator with charge (Q) (ASDQ) chips on boards that plug down directly onto the straws and provide the main signal. Each ASDQ plugs onto sixteen straws. These ASDQ boards are application specific integrated circuits (ASICs) which read out the signal from one end of the straws and shape and discriminate that signal, as well as providing

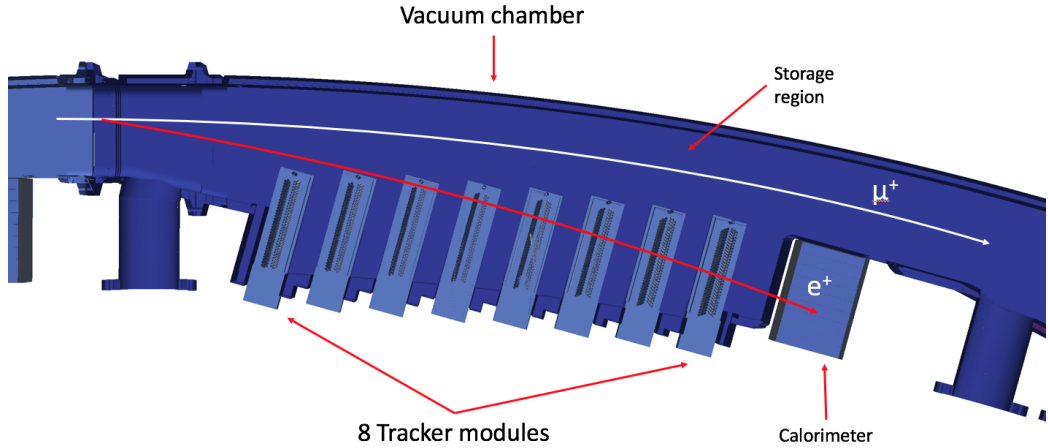


Figure 3·10: Birds eye view of a model of a vacuum chamber containing a tracker station, and the associated calorimeter. Each tracking station consists of eight tracker modules.

some baseline restoration and tail cancellation. The ASDQs and their associated components live in thin aluminum manifolds above and below the straws. The physical footprint of these boards and components was minimized in order to increase the straw measurement area. The signals from the ASDQs are passed through Flexi Cables to Time to Digital Converter (TDC) boards which time stamp the signals with 625 ps precision [64]. The Flexi Cables are flexible and thin such that the cables can be passed through the thin aperture shown on the right of Figure 3·8. High voltage is provided to the sense wires with high voltage boards, which pass the voltage through the ASDQs. A feedthrough board provides the interface between the TDCs and Flexi Cables, as well as the high voltage signal. They serve a dual purpose of providing the gas seal. Finally, there are logic boards that serve as the interface between the TDCs and the back-end electronics. They manage the clock and controls for the TDCs and store data onto FPGAs, which is piped out through a high throughput optical fiber connection. The logic boards, high voltage boards, and TDCs are all housed within an aluminum box which provides RF shielding. In each module there are eight ASDQs, four TDCs, two feedthrough boards, two high voltage boards, and two logic boards.

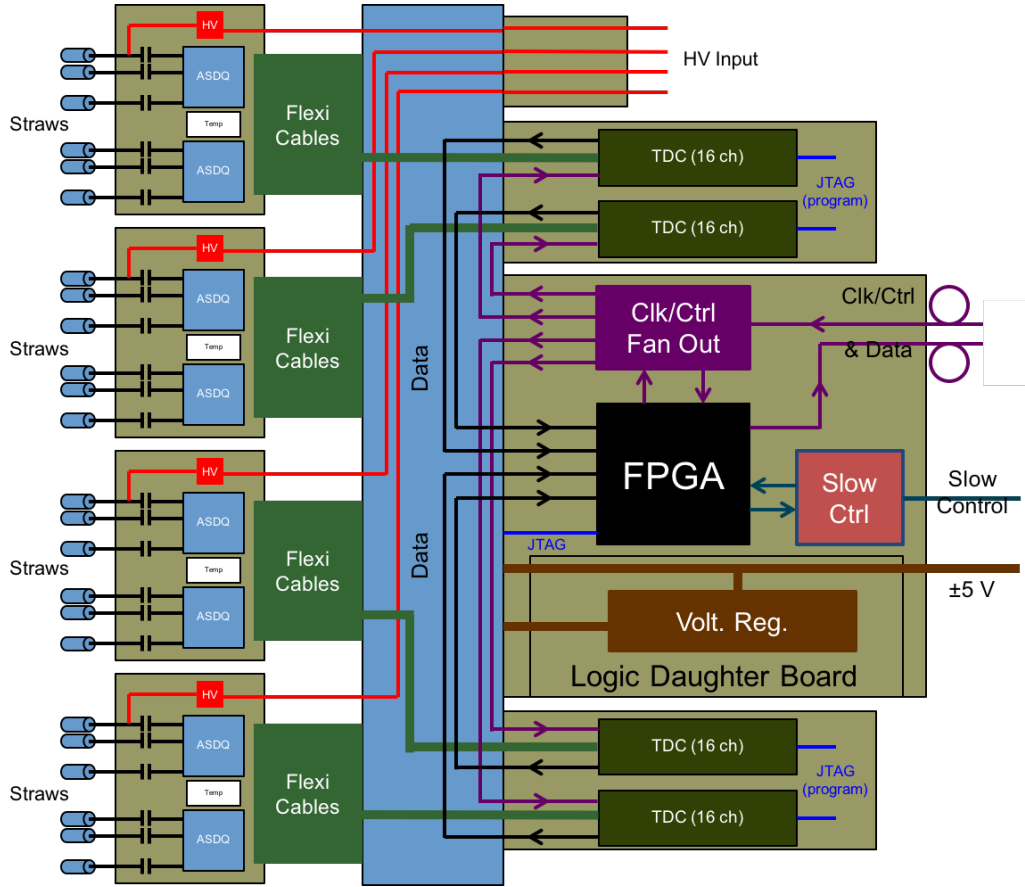


Figure 3.11: Front-end tracker electronics readout chain. Created by James Mott.

An overview diagram of the front-end readout chain is shown in Figure 3.11. The back-end electronics consist of FC7s, one per tracker station, and a single AMC13 for all tracker stations. These modules provide clock and DAQ services to the whole tracker system, and ultimately pipe out the data to where it can be saved on disk.

## Chapter 4

# Track Reconstruction and Analysis

As described in section 3.3, the straw trackers are used to provide information about the muon beam, important for the calorimeter  $\omega_a$  analysis, calculating the  $\omega_a$  pitch correction, and determining the spatially weighted magnetic field seen by the muons. The track reconstruction is performed in three stages: First, individual hits in the tracker are grouped into individual tracks in the finding stage. Second, a best trajectory is fit to grouped hits in the fitting stage. Third, the best fit trajectory is extrapolated back to the storage region or forwards to the calorimeter in the extrapolation stage. A fourth refinement stage is planned but not yet implemented, which would add or remove hits in the finding stage based on the results of the fitting and extrapolation stages.

As a brief aside, every stage of the track reconstruction is performed in the event-processing framework known as *art* [65]. The *art* framework is a collection of modularized stages in a C++ framework useful for reading, reconstructing, filtering, analyzing, and writing data, among other things. Most Fermilab experiments now use *art*, including E989.

### 4.1 Track finding

The track finding stage consists of pattern recognition routines in order to group individual hits into separate sets corresponding to individual incident tracks. The general implementation of these pattern recognition routines is relatively straightforward [66,

[67]. Hits across all modules are grouped in time windows called time islands, with an average width of 40 ns and a max width of 100 ns. Within those time islands hits are then grouped into clusters. Clusters consist of one or two hits for each U or V view per module. As a reminder the U and V views of a module consist of the two U or V layers in that module, Section 3.3. Hits are only clustered if they lie in close proximity in time and space to one another. The spatial constraint is defined as the difference in hit straw numbers, from 0 to 31 for the 32 straws per layer, which by default is limited to  $\leq 4$ . Neighboring hit clusters in the same module are then grouped to form seeds, one per module. Finally, seeds are grouped together module by module from one end of the tracker to the other to form what are called track candidates. The seeds are formed and grouped into track candidates again only if they lie close in time and space to one another. The entire track candidate formation process occurs for all hits in a time island to find as many real tracks as possible. See Figure 4.1.

After a track candidate has been formed a number of checks are made before passing it on to the fitting stage. If hits, clusters, or seeds are found to be shared among multiple track candidates, the candidates are dropped. Likewise, a track candidate is dropped if it is made from seeds consisting of only one type of view, or if the track candidate has less than six hits. There are also various small geometry and timing algorithms to improve the track candidates, such as removing hits from secondaries [68]. The  $t_0$  time for the track candidate is calculated as the mean time of all hits, with some fixed offset at the end. This  $t_0$  is helpfully constrained by geometry effects, where for a straight track passing through two layers in the same view, the sum of the drift times adds up to a constant. The track candidate is supplied with an original momentum and position guess at the start of the track by fitting a circle to the hit straw wires in the horizontal plane. The final track candidates are passed on to the fitting stage.

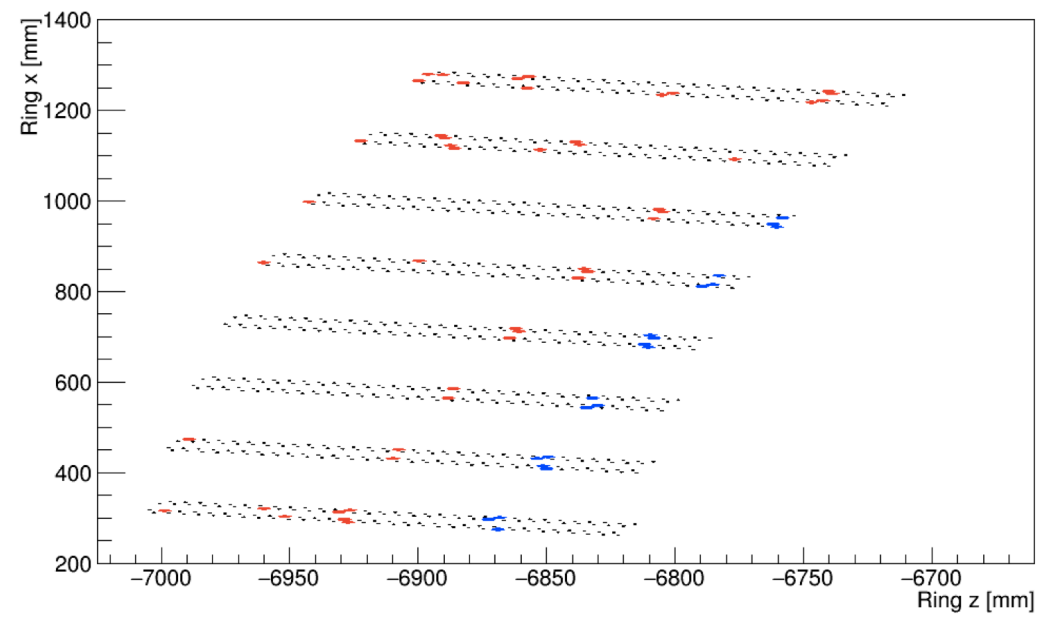


Figure 4·1: Hits in a tracker station in a single time island. The black dots indicate the position of the straw wires, while the blue and red points indicate hits. In blue is the first formed track candidate in the island, formed from separate seeds in different modules. The track finding algorithms will move onto the remaining hits in the time island to attempt to form other track candidates, one of which is easily observable by eye.

## 4.2 Track fitting

The track fitting stage takes the track candidates from the track finding stage, and outputs a best fit trajectory to those candidates. This includes optimal state vectors and error matrices for the track at each measurement plane and at a fictitious starting plane at the entrance to the straw tracking detector. The track fitting routines can roughly be split into two parts, error propagation and the actual fitting and improvement of the track. The implementation of these parts go hand in hand, and will be described in turn. Details of the track fitting code itself is described in Reference [69].

### 4.2.1 Error propagation and coordinate systems

The process of error propagation involves taking track parameters and error matrices (which describe the spread in those track parameters) and transporting them along discrete steps from one point to another, accounting for changes due to any present magnetic fields or material along the step paths. There is a set of error propagation routines originally written in Fortran by the EMC collaboration, called “Geometry and Error Propagation” or Geane [70]. Geane works by propagating particles along their average trajectories neglecting the effects of discrete processes, using a helix equation along small enough steps where the change in the magnetic field is small. These routines were used in the E821 experiment as well as the PANDA and FINUDA experiments with some success [71]. The Geane routines were at one point converted to C++ and added to Geant. The strength of using Geane within a Geant simulation lies in its direct access to the Geant geometry and field. This is crucially important for the E989 track fitting because the trackers live in a region of high field non-uniformity. Shown in Figure 4.2 is the location of the tracker with respect to the radial and vertical fields as calculated in Opera2D and included in the E989 Geant4

simulation. As shown the radial field in the tracker region rises from 0 T at the outer ends to roughly 0.3 T at the inner top and bottom ends, and the vertical field drops approximately 50% from the storage dipole field of 1.451 T. These large field gradients over the tracking measurement space must be handled appropriately, which Geane does nicely.

Predicted track parameters in Geane are a function of path length

$$p_l = F_{l,l_0}(p_0), \quad (4.1)$$

where  $p_0$  are some original tracker parameters and  $p_l$  are the updated ones. The path length  $l$  can be defined or limited how one wishes, and typically corresponds to a single step in the Geant4 simulation. The track parameter vectors  $p$  are defined in some coordinate system. In the Geane routines these track parameters are  $5 \times 1$  vectors either defined in the “free” (curvilinear) system

$$\frac{1}{p}, \lambda, \phi, y_\perp, z_\perp, \quad (4.2)$$

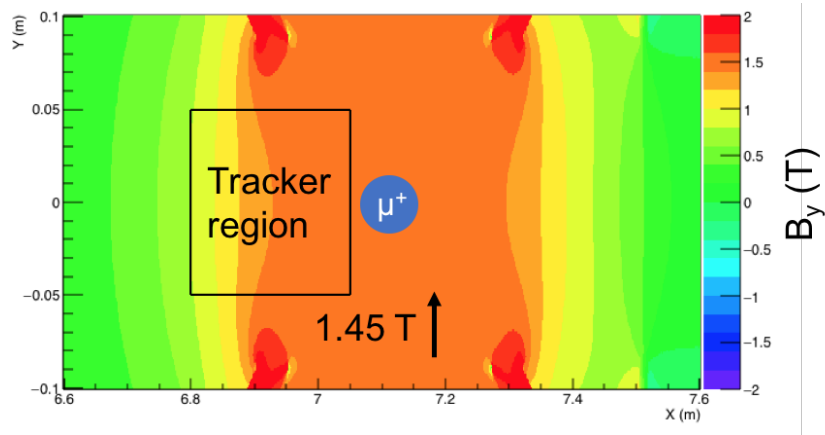
or the “surface” (detector) system

$$\frac{1}{p}, \frac{p_v}{p_u}, \frac{p_w}{p_u}, v, w. \quad (4.3)$$

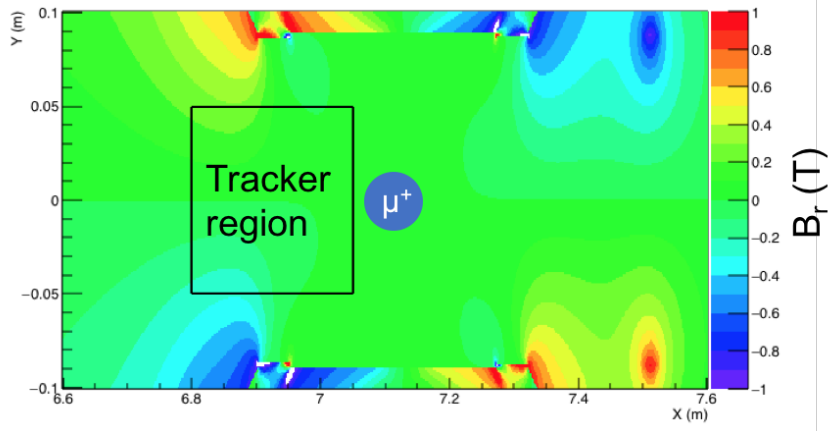
In the free system, the  $\lambda$  and  $\phi$  parameters are the dip ( $\pi/2 - \theta$ ) and azimuthal angles respectively, while the  $y_\perp$  and  $z_\perp$  parameters are defined as being in the  $XY$  or  $XZ$  global Geant4 planes and orthogonal to  $x_\perp$ , where  $x_\perp$  is defined as being along the momentum vector of the particle. See Figure 4.3. In the surface system, the UVW coordinates are defined with any two orthogonal vectors  $V$  and  $W$ <sup>1</sup>. The surface system is most usefully defined in the tracker reference frame, where the modules are

---

<sup>1</sup>For clarification, the UVW surface system has nothing to do with the UV orientations of the straws at this time.



(a) Vertical magnetic field



(b) Radial magnetic field

Figure 4.2: Shown are the vertical (top) and radial (bottom) magnetic fields of the storage ring magnet in and around the storage region as calculated in Opera 2D. The horizontal and vertical axes are the radial and vertical coordinates of the ring respectively. The center of the storage region lies at 7.112 m along the horizontal axis. The contours represent the strengths of the vertical and radial magnetic fields. The black box shows the rough location of the tracker with respect to the ring. It can be seen that there is a large field non-uniformity within the tracker space.

staggered in a local Z coordinate, the local Y coordinate is vertical, and the local X coordinate increases with straw number. See Figure 4.4. The surface system is then defined as

$$\frac{1}{p}, \frac{p_x}{p_z}, \frac{p_y}{p_z}, x, y. \quad (4.4)$$

In both free and surface systems the track is represented by one momentum parameter, two directional parameters, and two position parameters. Needing six independent parameters to describe a particle in space and momentum (three momentum and three position parameters), one parameter is left out and taken as a known variable. For Geane this is taken either as a known path length in the free system, or a known U coordinate in the surface system (or known Z coordinate in our tracker reference frame). In our tracker reference frame, the 32 straw layers corresponding to a tracking station are defined at known local Z coordinates. The path lengths for steps in Geane can be set to be equal to the distance for a track to travel between between detector planes, and therefore the track parameter dependence on the path length can instead be replaced by a dependence on plane number. The number of degrees of freedom per track is the number of measurement planes it hits,  $N$ , minus 5 for the number of track parameters.

The  $5 \times 5$  error matrix on a plane calculated in Geane describing the expected distribution in true parameters about the average ones is defined as

$$\sigma_N^{ij} = \langle p_N^i p_N^j \rangle - \langle p_N^i \rangle \cdot \langle p_N^j \rangle, \quad (4.5)$$

where i and j are track parameter indices and  $N$  is some plane number. This error matrix will include effects from multiple scattering, delta ray production, ionization, and bremsstrahlung [70, 71, 72]. These matrices are transported from plane to plane by what are called transport matrices, where the  $5 \times 5$  transport matrix elements

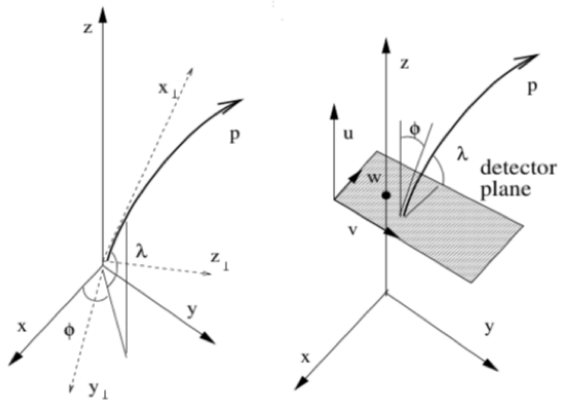


Figure 4.3: Free (left) and surface (right) tracking coordinate systems.

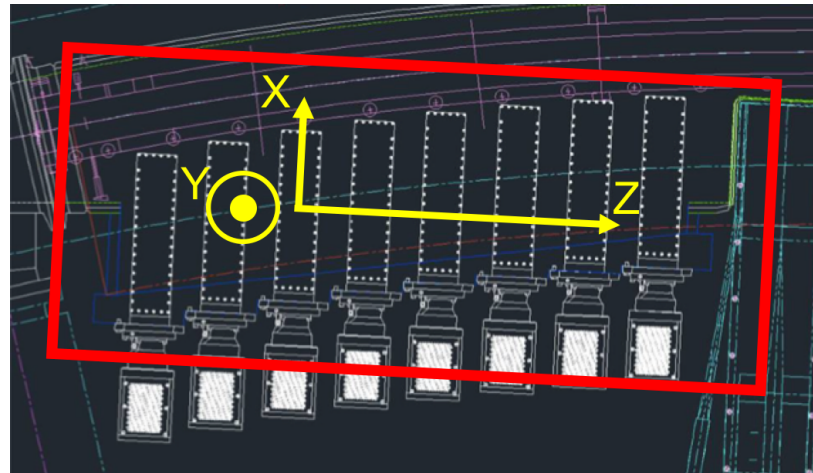


Figure 4.4: Shown is a model view of a tracker station in relation to the magnetic ring. Tracker modules are shown in white. Around the tracker measurement area is defined a coordinate system called the tracker reference frame. In that frame, the X coordinate is directed outward along the straws nearly radially, the Y coordinate is directed vertically up, and the Z coordinate is directed along the direction that the tracker modules are staggered.

between two planes are defined as

$$T_{N,N-1}^{i,j} = \frac{\partial p_N^i}{\partial p_{N-1}^j}. \quad (4.6)$$

The transport matrix  $T$  is a Jacobian between planes which expresses the infinitesimal changes in parameters at some plane (or path length) with respect to the parameters at some previous plane (or previous path length):

$$\delta p_N = T_{N,N-1} \delta p_{N-1} \quad (4.7)$$

Note that the transport matrix does not propagate the track parameters themselves as does an equation of motion. The error matrix is propagated forward from one plane to another by

$$\sigma_N = T_{N,N-1} \sigma_{N-1} T_{N,N-1}^T + \sigma_{\text{material}}, \quad (4.8)$$

where  $\sigma_{\text{material}}$  is the added error due to material effects between the planes. See Figure 4·5. The calculation of the transport matrices themselves is done within the Geane routines in the free system on a step by step basis, where the derivation of the transport matrix elements is given in Reference [73]. It should briefly be pointed out that the transport matrix between any two planes (or number of steps) is the multiple of all intermediate transport matrices,

$$T_{N,N-2} = T_{N,N-1} T_{N-1,N-2}, \quad (4.9)$$

regardless of what reference system the matrices are defined in (as long as they are all consistent). Geane can convert the transport matrices between the free system and the surface system using further Jacobians, also derived in Reference [73]. When

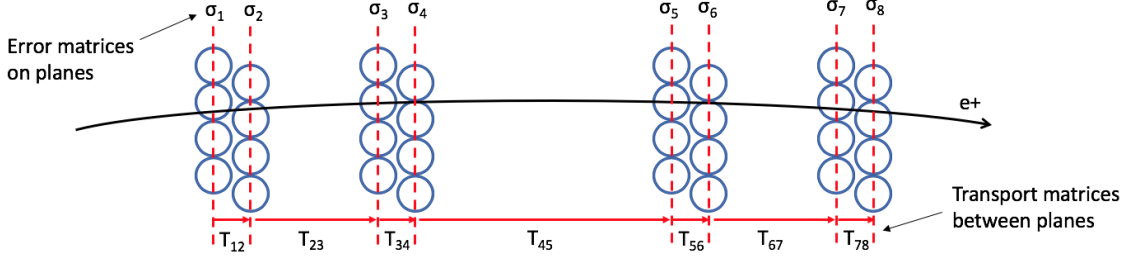


Figure 4·5: Transport matrices are defined between straw planes, and error matrices are defined on the planes.

converting a transport matrix from one reference system to another,

$$T_{N,N-1}^s = A_N T_{N,N-1}^f A_{N-1}^{-1}, \quad (4.10)$$

where the  $s$  and  $f$  superscripts stand for the surface and free reference systems respectively, and  $A$  is the Jacobian between reference frames which is defined at a specific point or plane ( $A_N \neq A_{N-1}$ ). The error matrices are converted between reference frames in the usual way,

$$\sigma_N^s = A_N \sigma_N^f A_N^T. \quad (4.11)$$

Finally, while the tracker reference frame is nominally defined in the local XYZ coordinates as described previously, the straws themselves don't measure in that frame directly. As described in Section 3.3, the straws measure drift circles in planes perpendicular to the straws themselves. The measurements from U and V straws therefore lie on the U and V measurement axes shown in Figure 4·6, where the measurement of the drift circle is instead taken as a U or V coordinate to the left or right of the straw wire. To first order the U or V coordinate is the DCA of the hit, which can be corrected with the angle of the track to get a better estimate, as shown in Appendix B. It's important to note that out of the five track parameters each straw only measures a single U or V position. The new coordinate system is

defined as

$$\frac{1}{p}, \frac{p_u}{p_z}, \frac{p_v}{p_z}, u, v, \quad (4.12)$$

where this  $Z$  variable is the tracker reference frame  $Z$ , and the U and V coordinates here are non-orthogonal and different to those in Equation 4.3. The transformation between the  $XYZ$  and  $UVZ$  systems is given by

$$p^{UV} = J_5 p^{XY} \quad (4.13)$$

$$(4.14)$$

where  $J_5$  is a  $5 \times 5$  matrix defined by

$$J_5 = \begin{pmatrix} 1 & 0 & 0 \\ 0 & J_2 & 0 \\ 0 & 0 & J_2 \end{pmatrix} \quad (4.15)$$

and  $J_2$  is a  $2 \times 2$  matrix given by

$$\begin{pmatrix} u \\ v \end{pmatrix} = J_2 \begin{pmatrix} x \\ y \end{pmatrix} = \begin{pmatrix} \cos \theta & -\sin \theta \\ \sin \theta & \cos \theta \end{pmatrix} \begin{pmatrix} x \\ y \end{pmatrix}. \quad (4.16)$$

$J_2$  is easily determined from Figure 4.6. In order to transform the transport or error matrices from the tracker reference frame to the tracker measurement frame, the same relations as in Equations 4.10 and 4.11 apply,

$$T_{N,N-1}^{UV} = J_5 T_{N,N-1}^{XY} J_5^{-1} \quad (4.17)$$

$$\sigma_N^{UV} = J_5 \sigma_N^{XY} J_5^T \quad (4.18)$$

where the superscripts of  $XY$  or  $UV$  identify which coordinate system the objects belong to.

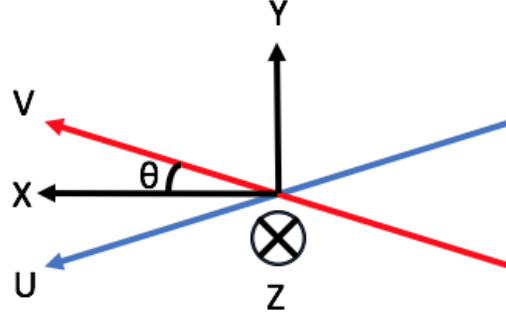


Figure 4.6: The straw tracker measurement reference system. The XYZ system here is the straw tracker reference frame.  $\theta$  is the same angle as the stereo angle of the straws, at  $7.5^\circ$ . U straws measure along the U axis and V straws measure along the V axis.

#### 4.2.2 $\chi^2$ minimization

The method for fitting and improving the track is a global  $\chi^2$  minimization algorithm that uses the transport and error matrices as described previously [70, 74]. This straightforward global fitting algorithm works because of the minimal amount of material contained within the tracker and the resulting small correlations between planes. For denser detectors with greater correlations, other fitting algorithms such as a Kalman filter should be used [71]. The following derivations and minimization assume measurements on planes in the tracker measurement frame described by Equation 4.12, but it should be noted that the results apply to any reference frame. A derivation for a  $\chi^2$  including no material correlations is presented followed by one which includes material correlations.

The  $\chi^2$  for a track is defined as the residuals between predicted and measured parameters on a measurement plane, divided by their errors, summed over all hit planes:

$$\chi^2 = \sum_{i=1}^N [(p_i(p_s) - x_i)^T (\sigma_i^{-1})(p_i(p_s) - x_i)] \quad (4.19)$$

$x_i$  are vectors of the measured track parameters on plane  $i$ ,  $p_i$  are vectors of the average predicted track parameters which stem from some general starting parameters  $p_s$ , and  $\sigma_i$  are the  $5 \times 5$  error matrices on the planes<sup>2</sup>. To first order the error matrices consist only of the measurement errors on the U and V parameters and exclude the effects of random material processes. These errors are located in the U and V diagonal elements (3, 3) and (4, 4) respectively, with corresponding resolutions of approximately 150  $\mu\text{m}$  as described in Section 3.3. At second order the material error matrices as calculated by Geane are added to the measurement errors. Because the measured parameters consist of solely U or V measurements, the  $x_i$  vectors are  $5 \times 1$  objects where only the (3) or (4) elements have any meaning respectively<sup>3</sup>. The errors on the non-measured parameters in the diagonals of the error matrix are taken as infinite, such that when the error matrix is inverted all corresponding rows and columns of the final matrix calculation on each plane reduce to zero and contribute nothing to the  $\chi^2$ .

By minimizing this  $\chi^2$  with respect to the starting parameters  $p_s$ , and evaluating it at the target best starting guesses  $p'_0$ , which are the parameters of interest, the track can be fit:

$$\begin{aligned} \frac{\partial \chi^2}{\partial p_s} \Big|_{p_s=p'_0} = 0 &= \sum_{i=1}^N \left[ \left( \frac{\partial p_i(p_s)}{\partial p_s} \Big|_{p_s=p'_0} \right)^T (\sigma_i^{-1}) (p_i(p'_0) - x_i) \right. \\ &\quad + (p_i(p'_0) - x_i)^T \left( \frac{\partial (\sigma_i^{-1})}{\partial p_s} \Big|_{p=p'_0} \right) (p_i(p'_0) - x_i) \\ &\quad \left. + (p_i(p'_0) - x_i)^T (\sigma_i^{-1}) \left( \frac{\partial p_i(p_s)}{\partial p_s} \Big|_{p_s=p'_0} \right) \right] \end{aligned} \quad (4.20)$$

The middle term is small and can be neglected assuming that the error matrix doesn't change much with respect to the choice of starting parameters. This is true

---

<sup>2</sup>The vector  $p_s$  has no numerical value at this time.

<sup>3</sup>A straw tracker module as a whole can be approximated as measuring in 2D space, but this leads to correlations between measured parameters which must be taken into account, as compared to the natural tracker measurement frame in 1D space of U or V for which there are no measurement correlations [75]. A fitting algorithm which fits the true measurement space of the drift circles themselves would be even better.

as the error matrix is already small due to the low amount of material in the tracker. (In tandem the error matrix doesn't change much from one fitting iteration to the next as long as the path length through the material remains about the same.) The first and third terms are identical in value, and so must therefore both separately be equal to zero. Equation 4.20 is therefore reduced to

$$0 = \sum_{i=1}^N T_{i0}^T \sigma_i^{-1} (p_i(p'_0) - x_i), \quad (4.21)$$

where  $T_{i0}$  is the transport matrix between the point at which the starting parameters are defined and plane  $i$  given by Equation 4.6:

$$T_{i0} = \frac{\partial p_i(p_s)}{\partial p_s} \Big|_{p_s=p'_0} \quad (4.22)$$

In minimizing the  $\chi^2$  the desire is to update some original set of starting track parameters  $p_0$  to the new best ones  $p'_0$ . This difference,  $\Delta p_0$ , can be determined by substituting the following into Equation 4.21,

$$p_i(p'_0) = p_i(p_0) + T_{i0}\Delta p_0, \quad (4.23)$$

which follows from Equation 4.7. After simplifying one arrives at

$$\Delta p_0 = \sigma_{p_0} \sum_{i=1}^N T_{i0}^T (\sigma_i^{-1}) (x_i - p_i(p_0)), \quad (4.24)$$

where

$$\sigma_{p_0} = \left[ \sum_{i=1}^N T_{i0}^T (\sigma_i^{-1}) T_{i0} \right]^{-1}. \quad (4.25)$$

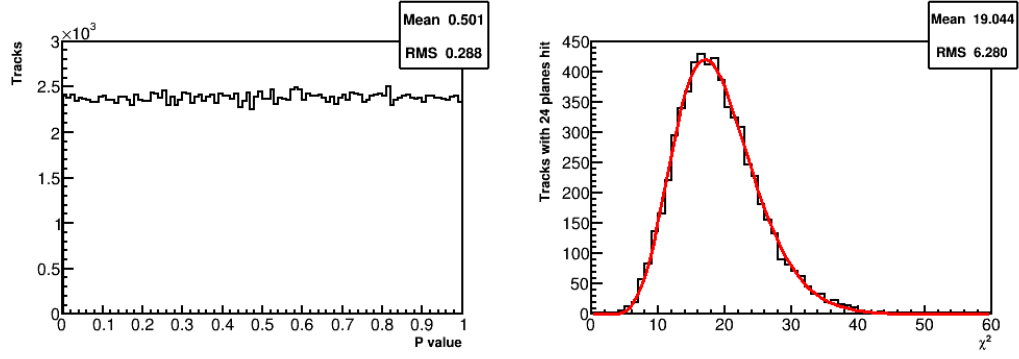
$\sigma_{p_0}$  is a  $5 \times 5$  covariance matrix of the starting fit parameters, where the diagonals describe the fit errors in the 5 track parameters at that point.

To summarize, an initial set of starting parameters  $p_0$  are propagated forwards

in Geant4 to produce predicted track parameters, transport matrices, and error matrices. These objects along with the measured parameters are plugged into the  $\chi^2$  minimization algorithm detailed here to provide a  $\chi^2$  describing the goodness of the fit corresponding to those original starting parameters, an improvement  $\Delta p_0$  to those starting track parameters, and the errors  $\sigma_{p_0}$  on those starting parameters. This consists of a single iteration of the track fitting. In order to determine the predicted parameters of the track corresponding to the improved starting parameters, the procedure needs to be repeated, or at least the error propagation part. The track fitting is iterated until the  $\chi^2$  no longer improves, at which point the track fitting is said to have converged. Typically three or four iterations are enough to get a best fit track, as shown in Figure 4.14. As a reminder the initial set of starting parameters is given by a circle fit to the hit straws as described at the end of Section 4.1. The starting parameters for a track are defined on a virtual 0 plane parallel to the measurement planes, where the placement of the 0 plane is defined based on a track by track basis and is placed at a point 1 cm in front of the first straw tracker module that was hit. Note that there is remarkable robustness with respect to the initial starting parameters in fitting the track. Of course if the initial starting parameters are too poor, then the fit will not converge.

#### 4.2.3 Fits to idealized tracks in vacuum

The tracking algorithm was first built and tested in a toy Monte-Carlo Geant4 simulation, and then ported over to the full E989 simulation in *art*. In the initial tests of the track fitting material was turned off and the measured hits were defined as the truth hits with some known smearing. (The truth hits are accessible within the Geant4 simulation by defined “dummy plane” detectors which record hits at the straw measurement planes.) Plots showing the goodness-of-fit for the fitted tracks are shown in Figure 4.7. Beyond the goodness-of-fit plots, the other measure of how good the track



(a) P value distribution for all tracks. (b)  $\chi^2$  distribution for tracks which hit 24 planes.

Figure 4.7: Goodness-of-fit distributions for fitted tracks in vacuum, with no material effects. The P value distribution is flat, and the  $\chi^2$  distribution matches a normalized  $\chi^2$  pdf for 19 degrees of freedom which is overlayed in red. ( $\chi^2$  distributions for tracks which hit other numbers of planes are very similar.) Only tracks which have failed due to Geant4 reasons are excluded.

fitting is performing is to plot the truth pulls of the fit parameters. The truth pulls are defined as the residual between the fitted parameter and the truth parameter, divided by the fit error on that parameter:

$$\frac{\Delta p_0^i}{\sigma_{p_0}^{ii}} = \frac{p_{0,\text{fit}}^i - p_{0,\text{true}}^i}{\sigma_{p_0}^{ii}} \quad (4.26)$$

Since the  $\chi^2$  minimization returns fit parameters and errors on the starting plane, this is where the truth pulls are defined. Plots of the truth pulls for the five track parameters are shown in Figure 4.8, where each pull is a unit Gaussian as they should be for idealized results.

#### 4.2.4 Material correlations

Random processes due to material contribute to the error matrix in Equation 4.5 as described in Section 4.2.1. The random scattering of a particle trajectory at one plane means that there is an extra correlated error in all further planes, see

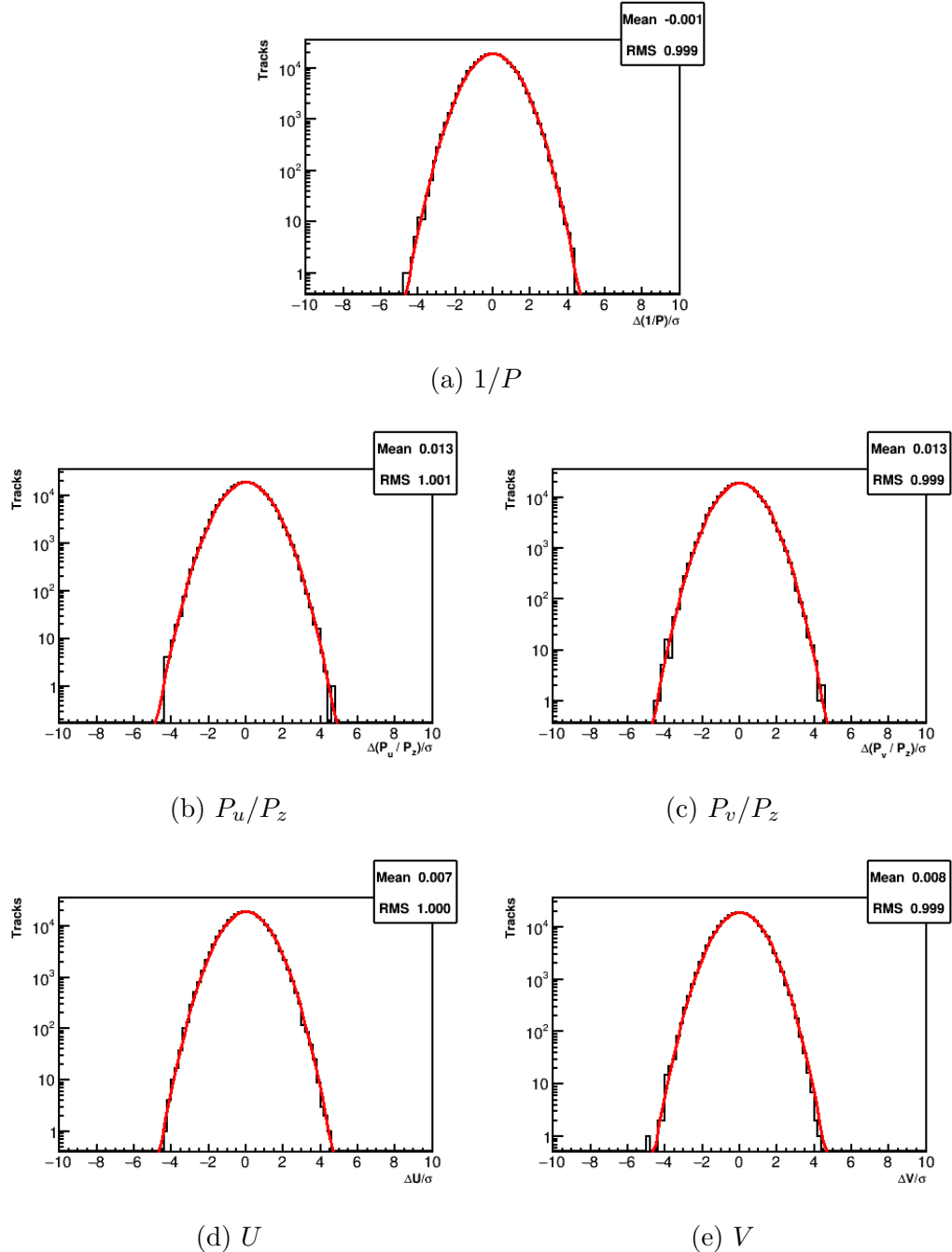


Figure 4.8: Truth pulls for the five fitted track parameters at the starting plane of the track, for tracks in vacuum with no material effects. The plots are shown on a log scale, and each are fit to a Gaussian in red. Each fit is consistent to a unit Gaussian with a mean of zero and an RMS of 1, showing that the track fitting is working properly. Only tracks which have failed due to Geant4 reasons are excluded.

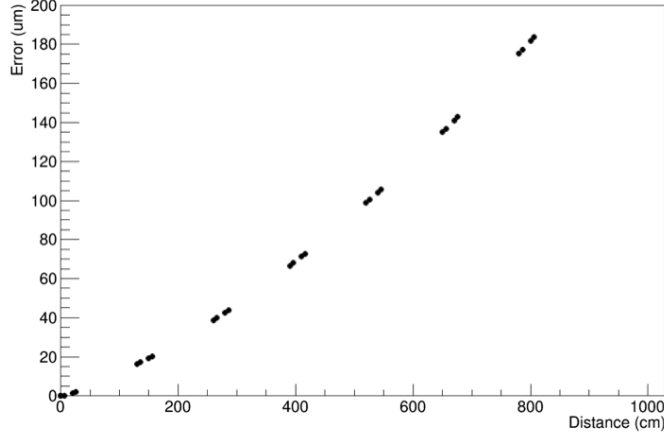


Figure 4.9: RMS error between the true track position and the average track position as a function of distance through the tracker. This error increases as a particle passes through more and more material. Each black point indicates the location of a straw measurement layer. If a track goes through the whole detector, on average the true position is nearly 200  $\mu\text{m}$  different from the average one.

Figure 4.9. Equation 4.19 does not take into account these material correlations between measurement planes when fitting the track. While it provides a decent approximation of the best fit track in the low material tracker, the  $\chi^2$  distribution is noticeably off as shown in Figure 4.10. To calculate a better estimate of the trajectory, a more general version of the  $\chi^2$  equation is used:

$$\chi^2 = (\vec{p} - \vec{x})^T (\sigma^{-1}) (\vec{p} - \vec{x}) \quad (4.27)$$

Here  $\vec{x}$  and  $\vec{p}$  are a  $5N \times 1$  vectors of the measured and predicted track parameters respectively, where  $N$  is the number of planes hit, and these objects are the combined vectors of the  $5 \times 1$  counterparts. Similarly,  $\sigma$  is a  $5N \times 5N$  matrix, where the  $5 \times 5$  diagonal block matrices are the individual plane error matrices described before, calculated between plane 0 and  $N$ . Calculating the  $\chi^2$  is now recasted from a sum over measurement planes into a single large linear algebra equation. At this point both calculations of the  $\chi^2$ 's are equivalent.

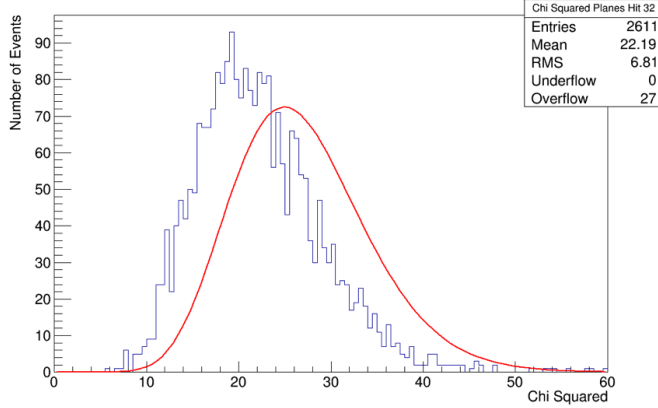


Figure 4.10: The  $\chi^2$  distribution for fitted tracks including material effects but excluding correlations in the calculation. The  $\chi^2$  distribution is noticeably different from the correct curve in red. **Axes labels and stats box don't look like previous plots, but not sure I can fix this besides overlaying stuff.**

The new format however allows for the material correlations between planes to be included, where these correlations are added as  $5 \times 5$  matrices in the off-diagonal blocks of the new large error matrix. The upper diagonals are given by

$$\sigma_{MN} = T_{MN}\sigma_N, \quad (4.28)$$

where  $\sigma_{MN}$  is the material correlation matrix between plane  $M$  and plane  $N$ ,  $T_{MN}$  is the transport matrix between the two planes, and  $\sigma_N$  is the ordinary error matrix as calculated from the 0 starting plane. **Need to cite or prove this equation, should do the latter but I can't quite remember the derivation at the moment.** The lower diagonals are just the transpose of Equation 4.28. The  $\chi^2$  is minimized in the same way as was done in the previous section such that the improvement to the starting track parameters  $\Delta p_0$  remains a  $5 \times 1$  vector and is given by

$$\Delta p_0 = \sigma_{p_0} \tau^T \sigma^{-1} (\vec{x} - \vec{p}), \quad (4.29)$$

$$\sigma_{p_0} = [\tau^T \sigma^{-1} \tau]^{-1}, \quad (4.30)$$

where  $\tau$  is a  $5N \times 5$  object of the individual transport matrices combined together.

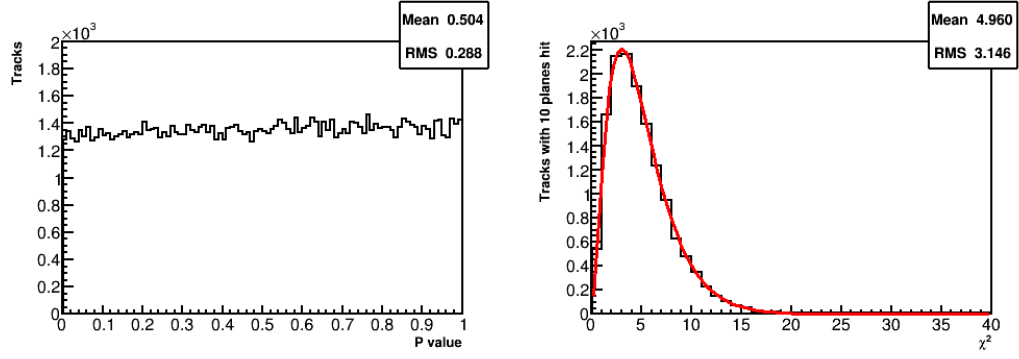
Because  $\sigma$  is such a large matrix,  $5N \times 5N$  where  $N$  ranges from 6 to 32, inverting it is a slow process. The tracking must have a certain amount of speed for the data to be efficiently processed and fit, which makes these inversions unfeasible. Note however that the diagonal errors of infinity values for non-measured parameters would reduce all the corresponding rows and columns to 0 after the inversion, in the same way as described before. This fact can be taken advantage of by removing said rows and columns that would contribute nothing to the  $\chi^2$  anyway, and thus reducing the  $5N \times 5N$  size to  $N \times N$ . The corresponding rows and columns of the unmeasured parameters in the combined transport matrix  $\tau$  and residual vector are also removed, resulting in an  $N \times 5$  matrix for  $\tau$  and an  $N \times 1$  vector for the residuals. The covariance matrix  $\sigma_{p_0}$  remains a  $5 \times 5$  matrix. This improves the speed of the  $\chi^2$  calculation dramatically, while leaving the final calculation unaffected<sup>4</sup>. All pieces of the  $\chi^2$  calculation and minimization is done with a C++ linear algebra library optimized for speed called Eigen3 [76].

#### 4.2.5 Fits to simulated tracks including material effects

Once the material correlations are properly included, the  $\chi^2$  distribution is repaired, as shown in Figure 4.11. The plots in this section show the results of the track fitting in the full  $g - 2$  Geant4 simulation with material effects turned on. Truth measurements with  $150 \mu\text{m}$  smearing are once again used as the measured hits, and a cut of 3 MeV on the true simulated energy loss is made to remove tracks which would result in poor fits anyways (from hard energy loss physics processes). The comparison between the simulated and reconstructed energy loss for fitted tracks is shown in Figure 4.12. While there is a noticeable difference, the energy loss in general

---

<sup>4</sup>Note that these element removals are done just before the final calculation of the  $\chi^2$  and fit to the track and not at the beginning of the algebra, otherwise the plane material correlations are not properly included.



(a) P value distribution for all tracks. (b)  $\chi^2$  distribution for tracks which hit 10 planes.

Figure 4.11: Goodness-of-fit distributions for fitted tracks in the full  $g - 2$  Geant4 simulation with material effects included. The P value distribution is flat, and the  $\chi^2$  distribution matches a normalized  $\chi^2$  pdf for 5 degrees of freedom which is overlayed in red.

is small so it is acceptable. Truth pulls for the tracks are shown in Figure 4.13. It can be seen that there is a slight spread in results due to the material effects. This is to be expected and the vast majority of tracks still fit well. The number of iterations it takes to fit a track is shown in Figure 4.14. The number of planes a track hits and the corresponding momentum dependence is shown in Figure 4.15. The total momentum distribution and residuals to truth are shown in Figure 4.16. The track fitting has a momentum resolution of approximately 2% with just a slight dependence on the momentum of the track.

After the track fitting has determined the best fit parameters in the  $UV$  space, the returned parameters can be turned back into the tracker reference frame coordinates. Plots for the fitted vertical and horizontal momenta, positions, and corresponding residuals are shown in Figures 4.17 and 4.18. The forward momenta plots are omitted since the majority of the total momenta is in the forward direction. More extensive plots than what is shown here can be found in Reference [69].

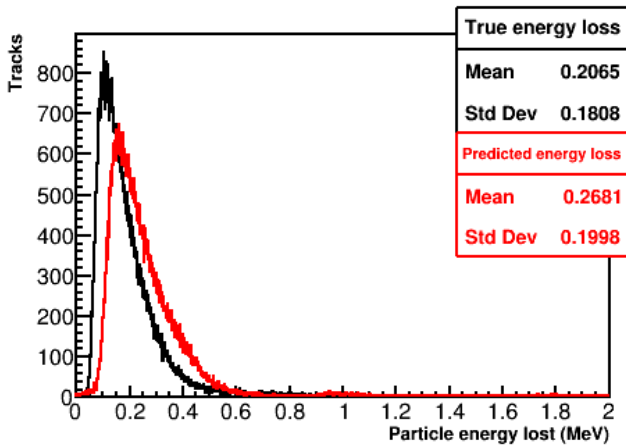


Figure 4.12: Simulated true energy loss (black) vs Geane predicted energy loss (red) for fitted tracks. As shown there is a mismatch between the two. This is acceptable as the energy loss is in general very small compared to the total momentum of each track,  $200\text{keV} \ll 2\text{GeV}$ . Sources of energy loss come from ionization and bremsstrahlung processes, which account for the long Landau tail running off to infinity. Originally the Geane physics calculations were taking too much energy away due to bremsstrahlung processes in our low material tracker, so the energy loss calculations were modified slightly [69].

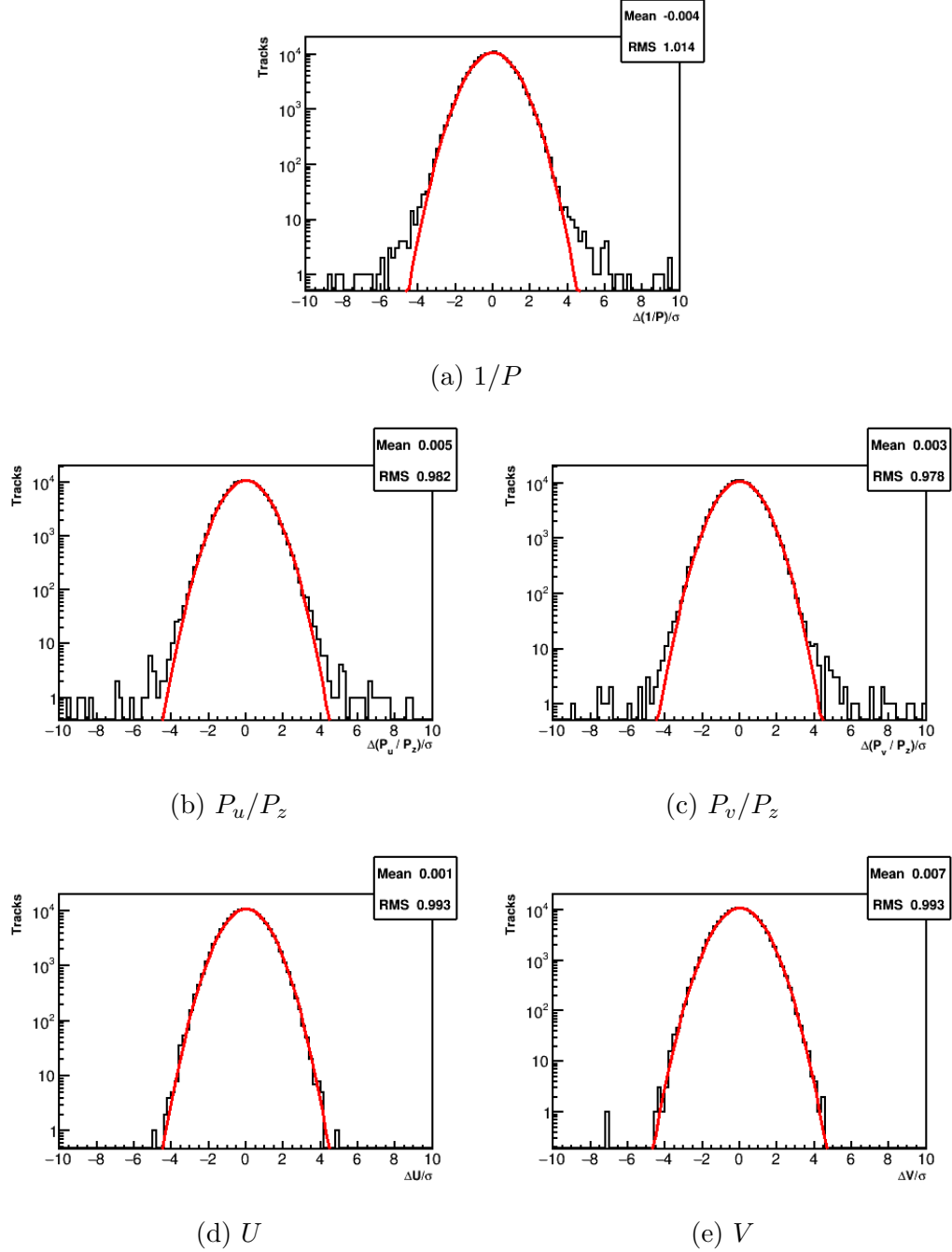


Figure 4.13: Truth pulls for the five fitted track parameters at the starting plane of the track for fitted tracks in the full  $g - 2$  Geant4 simulation with material effects included. The plots are shown on a log scale, and each are fit to a Gaussian in red. Each fit is close to a unit Gaussian with a mean of zero and an RMS of 1, but there are tracks which lie outside the Gaussian due to material effects and imperfect resulting fits.

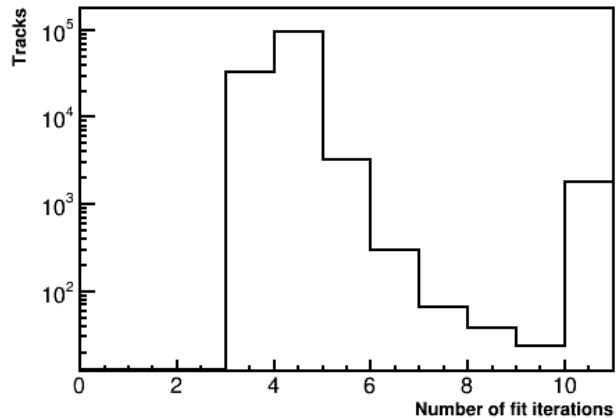
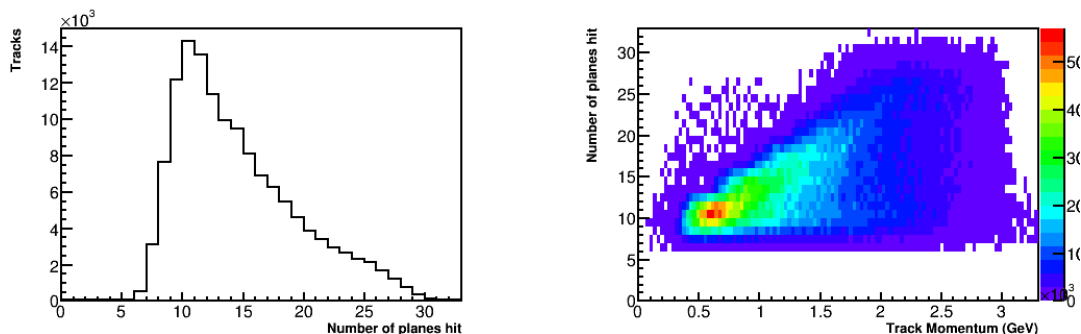


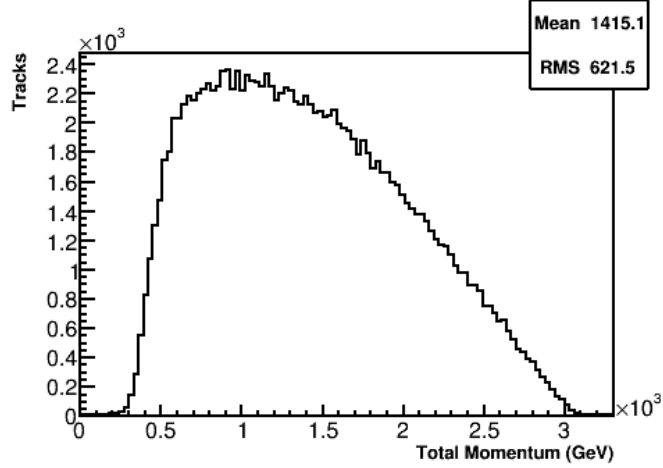
Figure 4.14: Number of iterations for the track fitting to converge per track. The track fitting does not take less than three iterations, and the number of iterations is capped at ten.



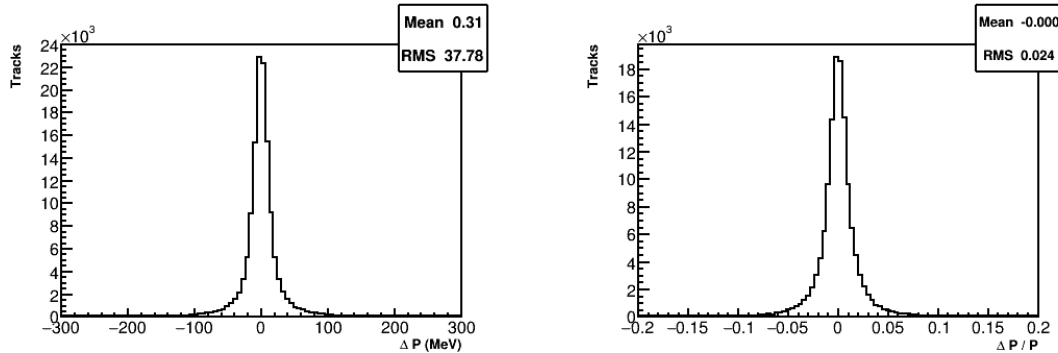
(a) The number of planes hit peaks at 10, and falls off to the maximum number of planes at 32.

(b) The number of planes hit vs the momentum of the track. Tracks with higher momentum in general hit more planes.

Figure 4.15: Number of planes hit per track (left) and the momentum dependence (right).



(a) The fitted momentum distribution for tracks which tails off at approximately the magic momentum of 3.094 GeV.



(b) The residual between the reconstructed and true total momentum. The RMS is approximately 40 MeV, though there are some tails which spread out from the distribution.

(c) The relative residual between the reconstructed and true total momentum. The RMS is approximately 2.4 %. This plot includes tracks of all momenta; in general the resolution of the total momentum is around 2% for all energies.

Figure 4.16: Fitted track momentum distribution and corresponding residuals to truth.

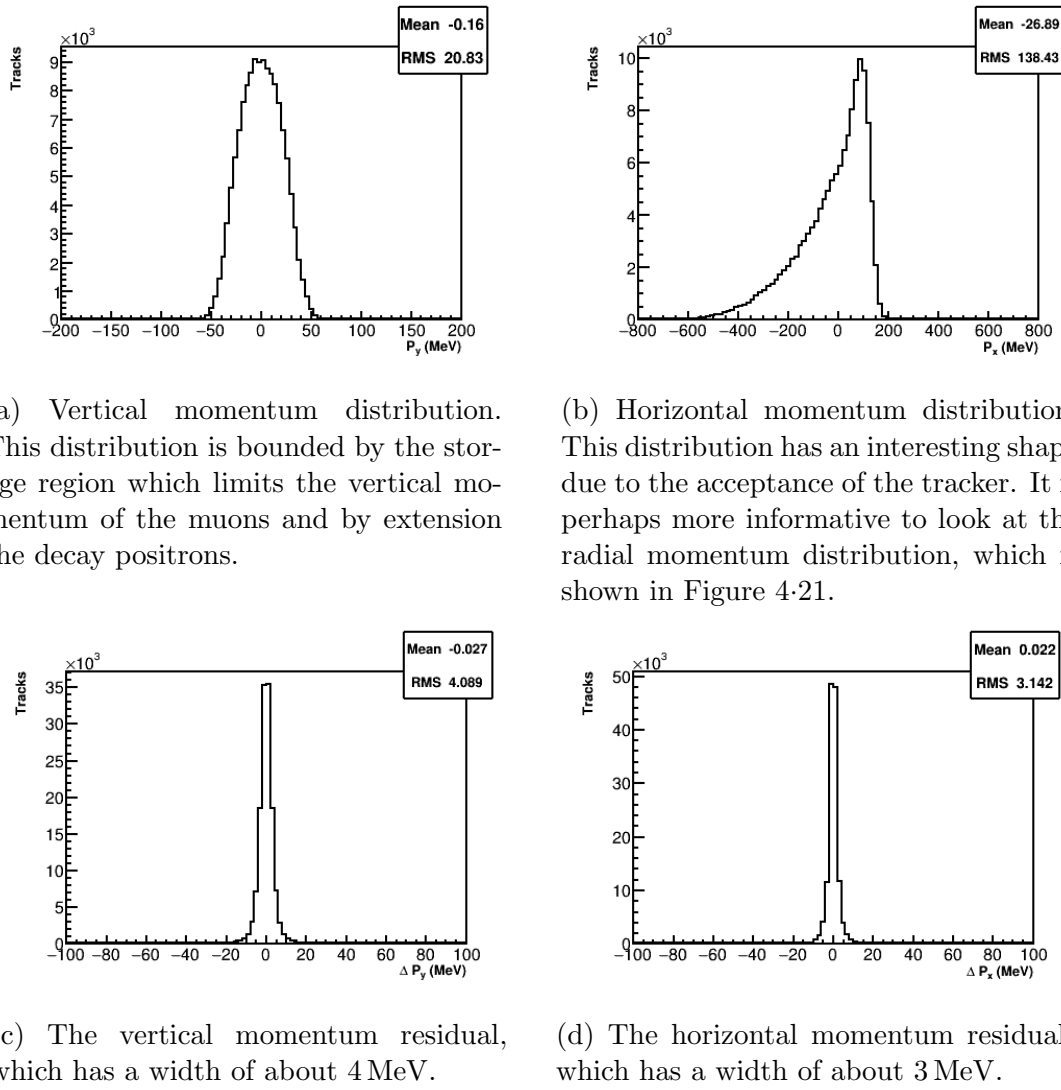
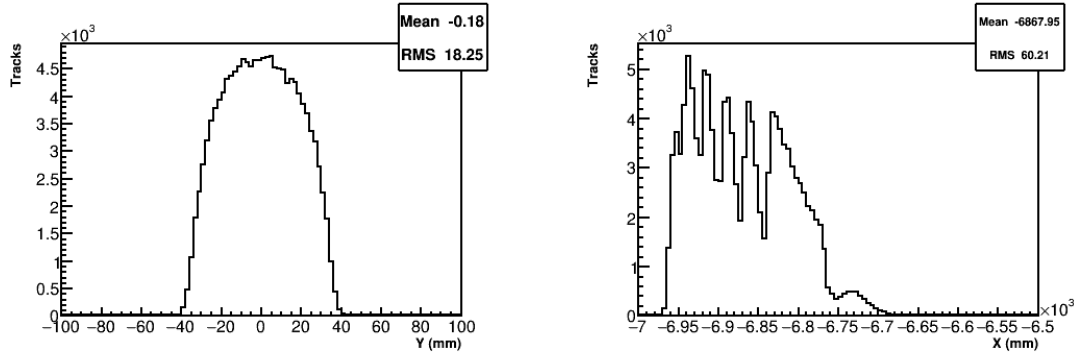
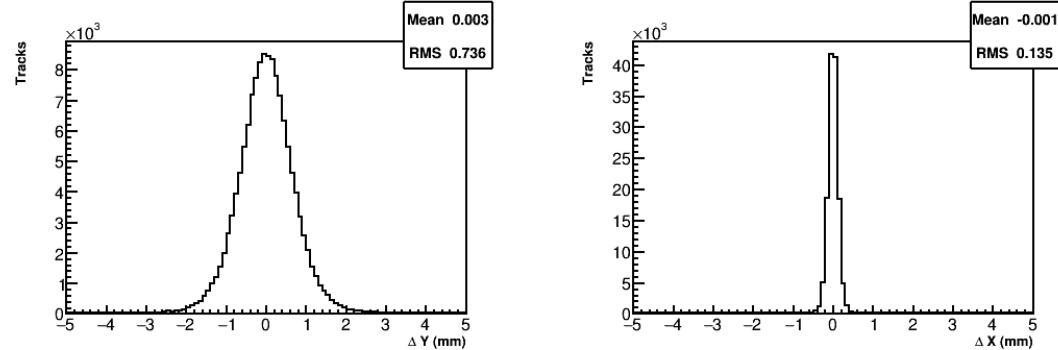


Figure 4.17: Shown are the fitted vertical and horizontal momentum components (top) for tracks at the entrance to the tracker, and their residuals to truth (bottom).



(a) Vertical position distribution. This distribution is bounded by the storage region which limits the vertical positions of the muons and by extension the decay positrons.

(b) Horizontal position distribution. This distribution has an interesting shape due to the acceptance of the tracker. It is perhaps more informative to look at the radial position distribution, which is shown later in Figure 4.21.



(c) The vertical position residual, which has a width of about 740  $\mu\text{m}$  at the entrance of the tracker. This is expected from geometry arguments with the angles of the straws which measure mostly horizontally.

(d) The horizontal position residual, which has a width of about 140  $\mu\text{m}$  at the entrance of the tracker. This is close to the input straw resolution of 150  $\mu\text{m}$  but slightly better due to the fact that both straws measure mostly horizontally.

Figure 4.18: Shown are the fitted vertical and horizontal position components (top) for tracks at the entrance to the tracker, and their residuals to truth (bottom).

#### 4.2.6 Left-right ambiguity and fit modes

Before actual data can be fitted, the left-right ambiguity problem needs to be dealt with. Since straws only measure drift circles and not actual U or V positions, and since tracks are in general passing forwards through the detector, there is an ambiguity as to which side of the wire a particle passed for each hit. In general if even a single left-right choice for a hit is wrong then a track will fit poorly. There are a couple of different track fitting modes used to deal with this problem, which are detailed in Reference [69] and summarized here and in Reference [77].

##### `wireFit`

The first fit to any set of tracks in data is to do a fit to the wire centers, which requires no left-right information. The errors on the measured hits are set as the RMS of a uniform distribution with a width of a straw diameter. After a wire fit, an approximation of the best fit track is acquired which provides some left-right information. The number of fitting iterations is capped at three for the wire fit.

##### `mainfit`

The primary fit mode for analyzing data is called `mainFit`. After the wire fit is completed, the predicted track parameters at each measurement plane are compared to the locations of the wires for the straws that were hit. The left-right choices for each hit are set depending on which side of the wire the predicted track passed. The measured hit positions and errors are updated from the wire values to the angular-corrected DCA values based on the the left-right choices of each hit, and the fitting is repeated. At each iteration of the fitting, the left-right choices for each hit are updated based on where the previous predicted track parameters ended up. This is the fastest fit mode and with this method about 66% of tracks fit well. Since there is no shortage when it comes to statistics for positron tracks, this is acceptable.

### `fullSeqFit`

The secondary fit mode is called `fullSeqFit`. This fit mode does a better job of determining the left-right choices for the hits in a track, but is much slower than `mainFit`. Here is given a short summary, see Reference [69] for more technical details on all parts of this fitting mode.

After a wire fit, the geometry of the straw layers is used to resolve some of the left-right choices for a hit on a track. The left-right ambiguity is partially resolved through the shift in layers for each view as detailed in Section 3.3, where if a particle passes straight through both layers in a view it can be seen to go to the left of one wire and the right of the other. This implies that for curved tracks with certain angles through tracker modules, the left-right choices for some hits are known precisely [78]. For these hit planes the left-right choices are locked in and taken as known for the rest of the fitting.

For the remaining hits where the left-right choices are unknown, an approximate  $\chi^2$  is calculated for each combination of left-right choices,  $2^{N_{\text{unknown}}}$ . This  $\chi^2$  is calculated using the same formula as in the full fitting with the measured parameters set to the different left-right combinations, Equation 4.27, but using the Geane transport and error matrices calculated by the wire fit instead of from a fit to the left-right choice measured parameters. Calculating this  $\chi^2$  for each combination is slow, so this process is sped up by only checking the left-right combinations for the U or V hit layers at a time respectively,  $2^{N_{\text{U,unknown}}} + 2^{N_{\text{V,unknown}}} \ll 2^{N_{\text{unknown}}}$ . This  $\chi^2$  calculation allows for a measure of how good a left-right combination is to be determined without having to propagate every track in Geane for the full fitting. The tracks with the best combinations and smallest approximate  $\chi^2$ 's are then fit with the full Geane propagation and  $\chi^2$  minimization algorithm. Typically the best 10 to 15 combinations are fit, and the final track with the best  $\chi^2$  is taken as the true track. This gets the

left-right choices for the fitted tracks right about 99% of the time with simulated data, but is very slow due to the combination checking and the Geane propagation for each of the best track left-right combinations. If the track fitting can be sped up significantly or a majority of the left-right choices constrained upstream somehow, then this fit mode would be more useful.

#### **4.2.7 Fits to tracks from data and comparison with Monte-Carlo**

Fits to data are done with `mainFit`. Due to imperfect left-right assignments and the use of real DCA and DCA error measurements, the tracks from data are naturally more messy. See Figure 4·19 for a plot of the goodness-of-fit for the tracks. While not all tracks are fit perfectly, enough of them are fit well in order to pass on the results to the extrapolation stage. Fitted tracks to Run 1 data are compared to results from Monte-Carlo. Track times and fitted total momenta are shown in Figure 4·20. Fitted track radial and vertical momentum and position distributions are shown in Figure 4·21. In general the results are very similar between the two. There are mismatches in the distributions because the idealized simulation did not reflect the real run conditions at the time of this track fitting analysis. As described in Section 2.8 and explored later in Section 4.4, the muon beam was imperfectly stored in the ring leading to the measured distributions here.

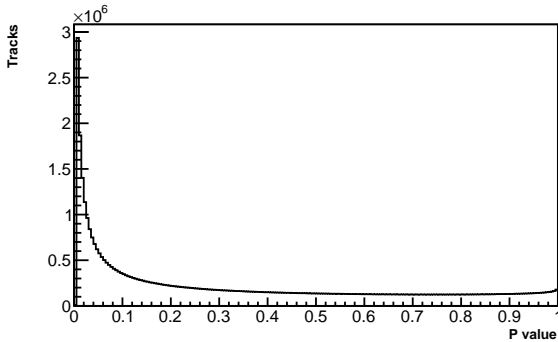
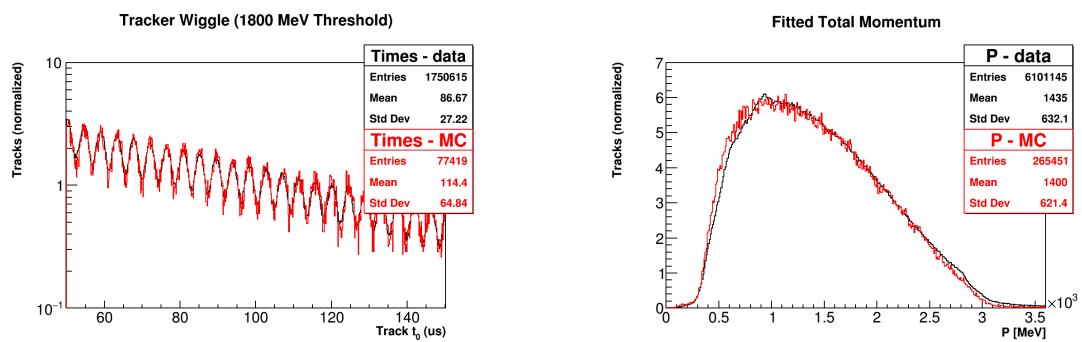


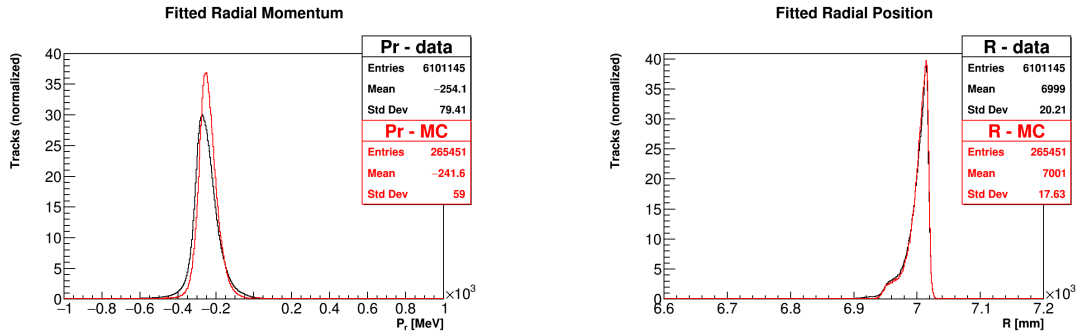
Figure 4.19: P value distribution for fitted tracks in data. A cut has been made at 1% to remove tracks which have entirely failed the fitting. The distribution can be seen to rise towards zero where tracks have been fit but imperfectly.



(a) Track times for tracks with energy greater than 1.8 GeV. The  $g - 2$  frequency can be seen in both the data and simulation.

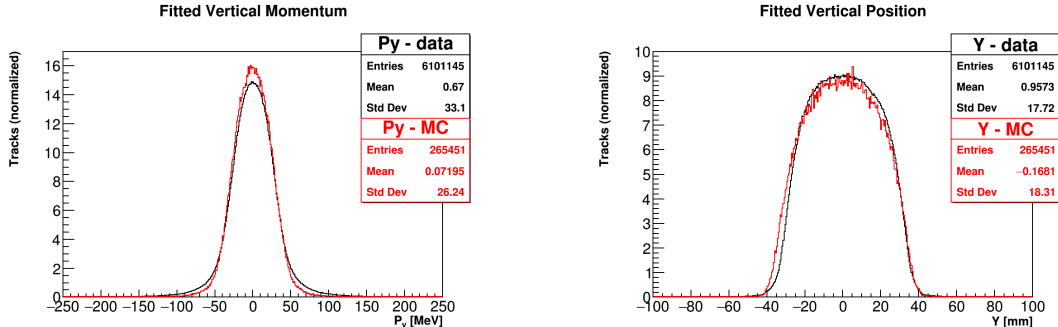
(b) Fitted track total momentum, there is a very slight mismatch between data and Monte-Carlo.

Figure 4.20: Fitted track results in data (black) vs Monte-Carlo (red). The amount of entries in each are normalized to each other so that they can be compared. Shape differences between the two are due to a mismatch between simulation conditions and the real experiment, and not any problem with the track fitting.



(a) Fitted track radial momenta. The radial momenta of the tracks are negative as particles are curving inwards through the tracker. There is a very noticeable difference between data and Monte-Carlo results.

(b) Fitted track radial positions. The shape depends on the acceptance of the tracker and in general lies below the magic radius of 7.112 m. Data and Monte-Carlo results match well.



(c) Fitted track vertical momenta. The momentum is bounded by the storage region, and data has a slightly wider width than Monte-Carlo.

(d) Fitted track vertical positions. The positions are bounded by the storage region. There is a noticeable difference between data and Monte-Carlo.

Figure 4.21: Fitted track results in data (black) vs Monte-Carlo (red). The amount of entries in each are normalized to each other so that they can be compared. Shape differences between the two are due to a mismatch between simulation conditions and the real experiment, and not any problem with the track fitting.

### 4.3 Track extrapolation

The last stage of the track reconstruction is the track extrapolation. The extrapolation takes the fitted track results and either extrapolates them back to the storage region to the approximate position of the muon decay point, or forwards to the face of the calorimeter sitting right behind the tracker. The extrapolation stage utilizes a fourth order Runge-Kutta Nyström algorithm [60] which discretely steps a trajectory through the magnetic field in the full  $g - 2$  Geant4 simulation, similar in some respects to the error propagation. At each step of the extrapolation, the updated track position and covariance matrix are compared to physical volumes in the simulation to flag tracks which have been reconstructed as likely originating from outside the storage region [60, 79]. Because there is no fixed interaction point in the storage region, tracks are extrapolated backwards to the point of tangency where the radial momentum is equal to zero. Studies were done to verify that this approximation for the muon decay point was sufficient using Monte-Carlo, and it was found that a simple 1.1 mm correction to the radial decay position could be applied regardless of the momentum of the track [60]. The vertical extrapolated distribution was found to have no biases. (What about the azimuthal point? Mentioned a little bit in DocDB 8564 but do I really want to go into it?) A birds eye view for tracks extrapolated back into the storage ring is shown in Figure 4.22.

### 4.4 Muon beam measurements

All stages of the track reconstruction have ultimately lead to the goal of determining the characteristics of the muon beam. As described in Section 2.6, the muon beam is not a fixed entity. Where the muons live and how they move in the storage region ultimately affect the calculation of the E-field and pitch corrections, the weighting of the muon distribution with respect to the measured field, and the calorimeter preces-

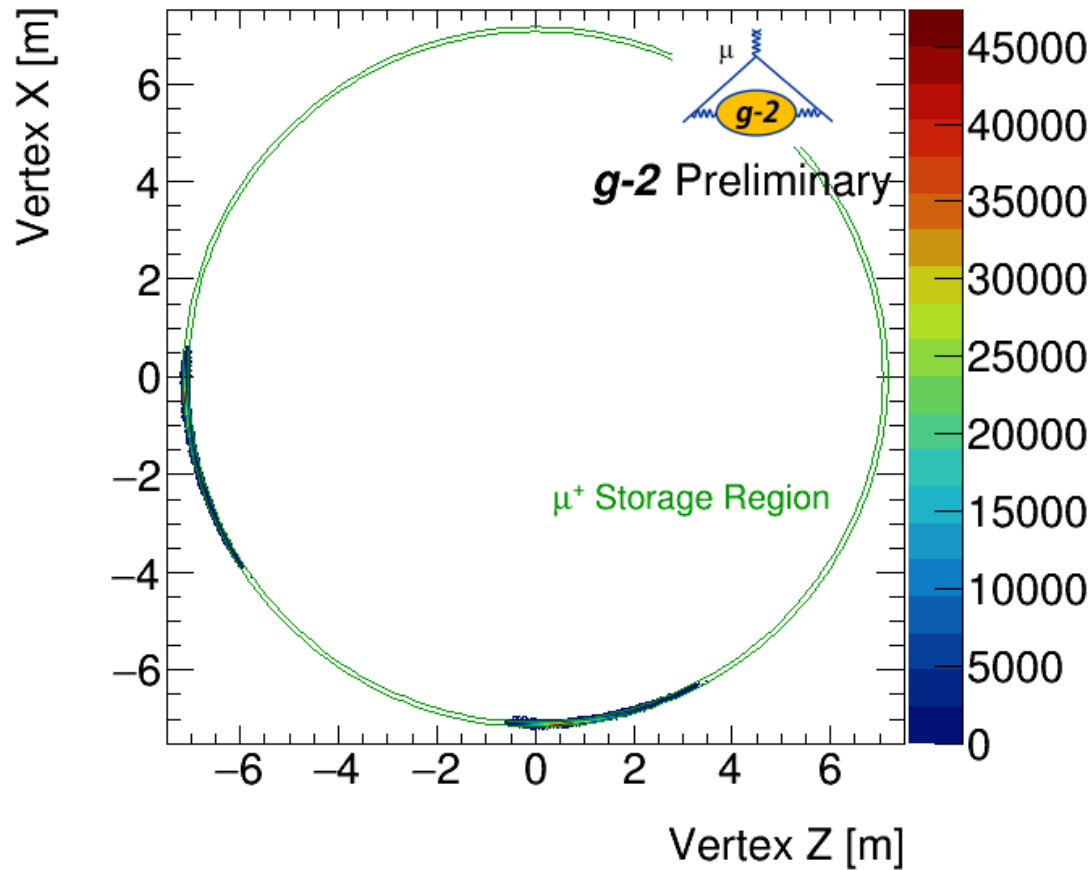


Figure 4.22: A birds eye view of the extrapolation results in the storage ring. The two distributions of extrapolated tracks can be seen at the left and bottom of the figure, where the tracker sits at the heads of the distributions. It can be seen that some tracks are extrapolated multiple meters back through the storage region. Plot courtesy of James Mott.

sion frequency analysis. Here are presented plots for the 60H dataset which describe the muon beam in the storage region, for those muons which decayed to positrons which then passed through the tracking detectors. There is still on-going work in regards to analyzing the acceptance differences between the tracker and calorimeter, in order to make sure that the correct muon beam dynamics are described in regards to those positrons which hit the calorimeters and are responsible for the measurement of  $\omega_a$ . Tracker-calorimeter matching studies will not be detailed here. A preliminary analysis is given in Reference [64].

The following cuts are applied to the track reconstruction [80, 81]:

- Non-failed track or vertex
- No volumes hit
- Number of tracking planes hit  $\geq 12$
- p value  $> 5\%$
- Vertical extrapolation uncertainty:  $0.5 < \sigma_y < 3.5$  mm
- Radial extrapolation uncertainty:  $0.5 < \sigma_r < 5$  mm
- Horizontal entrance into tracker:  $60 < X < 150$  mm
- Vertical entrance into tracker:  $-40 < Y < 40$  mm
- Drift time:  $0 < t_d < 70$  ns
- Track UV residuals  $< 500$   $\mu\text{m}$
- Fraction of missed planes  $< 30\%$
- $|\text{Number of U hits} - \text{number of V hits}| \leq 4$

These cuts remove failed or poorly fitted tracks, and cut out those tracks which end up in the tails of various quality checking distributions. By applying these cuts a clean sample of the extrapolated muon decay positions is extracted without biasing the results.

First, a radial slice of the extrapolated beam distribution is shown in Figure 4·23. As shown the beam is off-center due to kicker effects. The radial and vertical projections of this cross-section are shown in Figure 4·24. The vertical distribution is very similar to that from the track fitting results, while the radial distribution of the stored muons has a non-Gaussian shape due to the storage procedure of the muons. These two distributions in general appear wider than they actually are at a single point in time, because tracks of all times are included in these plots and the beam is moving in time. Figure 4·25 shows the radial and vertical distributions of the muon beam as a function of time in-fill, with the means plotted in Figure 4·26. Table 4.1 gives the measured values of the beam parameters corresponding to the various datasets. Because of the bad quad resistors, the beam was actually seen to start at a greater vertical position than the center of the storage ring, and slowly move downwards over the course of a fill. Similarly, the vertical width of the beam decreases slowly over the course of a fill. **Include plots for this or reference another document?**

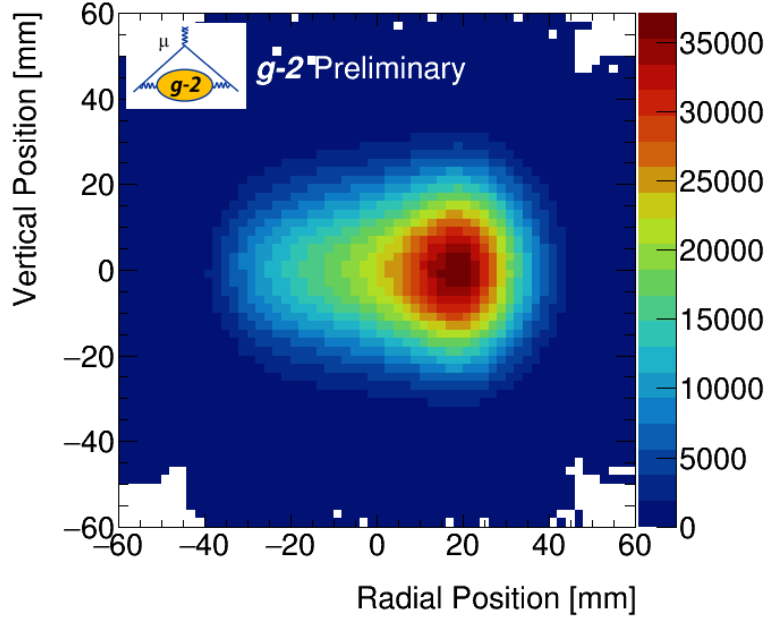
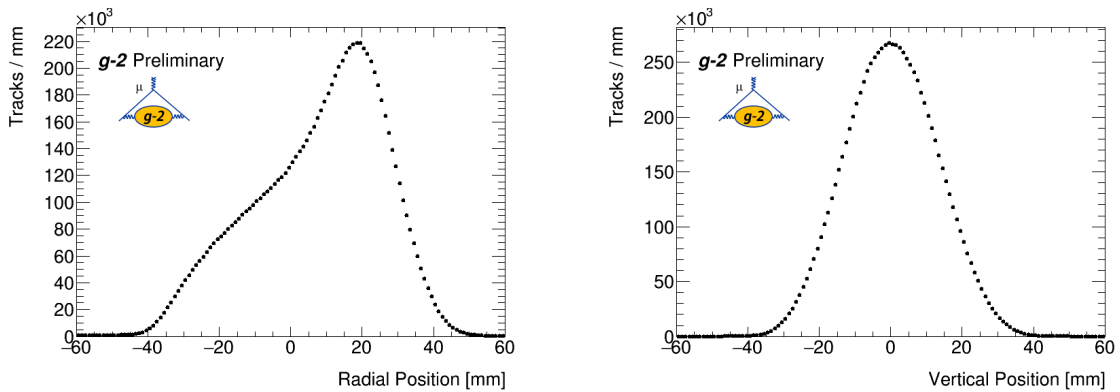


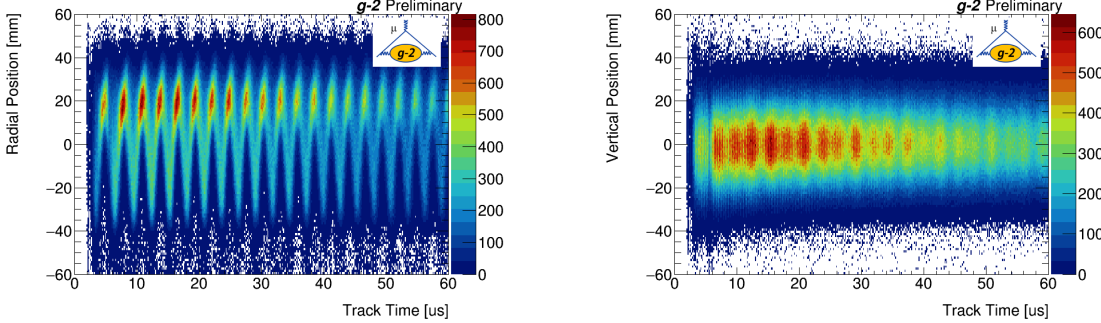
Figure 4.23: Shown is a radial slice of the extrapolated muon distribution or beam spot. The beam is localized off center of the storage ring due to the kicker settings used, Section 2.8. Plot courtesy of James Mott.



(a) The radial position of 0 mm corresponds to the magic radius of 7.112 m. The radial distribution is peaked radial outward from the center.

(b) The vertical distribution looks closely centered in the storage region, which as a reminder has a width of 9 cm.

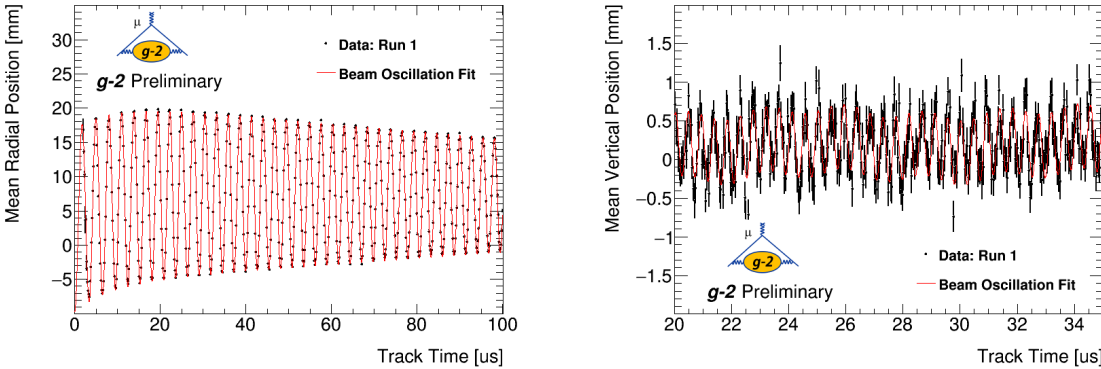
Figure 4.24: Shown are the muon beam radial (left) and vertical (right) distributions for all track times. Plots courtesy of James Mott.



(a) The radial distribution of the muons can be seen to both oscillate radially inward and outward as a function of time, and bunch and spread out as a function of time. This behavior is the CBO of the beam.

(b) The vertical distribution of the muons is relatively stable as a function of time, but there is an oscillation that can just barely be seen.

Figure 4.25: Shown are the muon beam radial (left) and vertical (right) distributions as a function of time in-fill for tracks in Station 12. In general the distributions for Station 18 are very similar. Plots courtesy of James Mott.



(a) The radial distribution mean oscillates at the CBO frequency. It can be seen to rise at early times in Station 12 due to the scraping procedure, and then slowly relax away once the scraping is turned off and the muons decay away.

(b) The vertical distribution mean oscillates at the vertical waist frequency, as described in Table 2.2. As shown for these early track times the beam is actually stored slightly higher than the center of the storage region.

Figure 4.26: Shown are the muon beam radial (left) and vertical (right) distribution means as a function of time in-fill for tracks in Station 12. In general the distributions for Station 18 are very similar. Plots courtesy of James Mott.

Run 1 Dataset Muon Beam Parameters					
Name	Radial Mean	Radial Mode	Radial Width	Vertical Mean	Vertical Width
60H	7.61	19.14	18.43	0.15	12.88
HighKick					
9d					
LowKick					
SuperLowKick					
Endgame					

Table 4.1: Table of muon beam widths and means. Both radial and vertical values are defined with respect to the center of the storage region. All values are in units of mm. Numbers input from root file, not from E-field/pitch workshop values. Verify this table with James, make sure the parameters are associated with the plots and cuts I've listed and shown. Might want to reduce the table if most dataset results are the same.

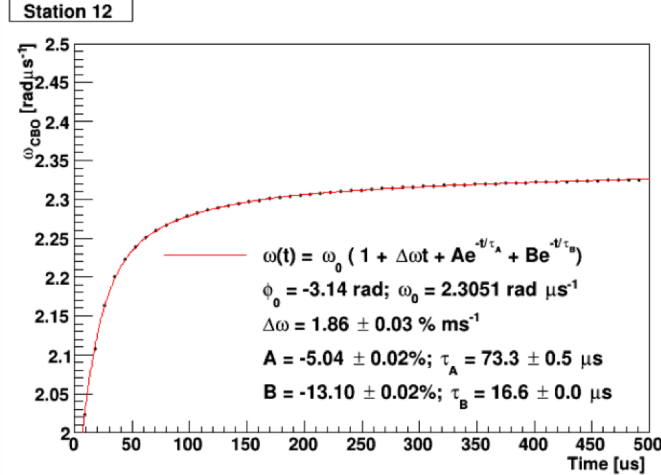


Figure 4.27: The CBO frequency as a function of time in fill. It can be seen to rise at early times and rise slowly at later times. This frequency change is due to the slowly changing quad voltages over each fill. The CBO frequency is fit to a function which includes a linear term and two exponentials. Plot courtesy of James Mott.

The observed oscillation is the CBO as described before in Section 2.6.1. It can be seen that over a course of a fill, the CBO decays away, and there is a corresponding beam motion as a consequence. As described in Section 2.8, the CBO characteristics of the beam were found to be changing over the course of a fill. Using the tracking results shown here, the CBO frequency and amplitude can be characterized [82]. The CBO frequency as a function of time in fill is shown in Figure 4.27. The CBO amplitude as a function of time in fill is shown in Figure 4.28. Both of these characteristics will be folded into the precession frequency analysis as will be described later.

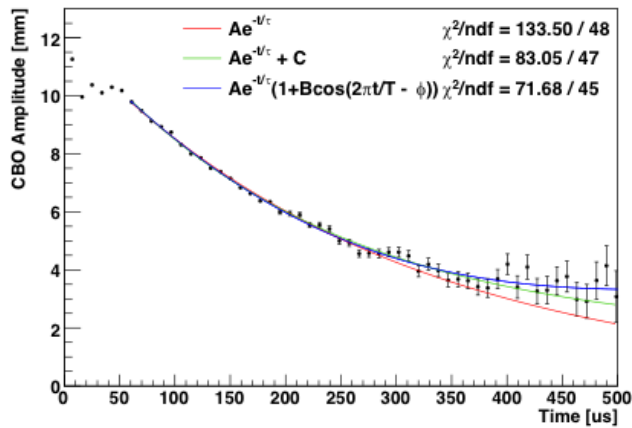


Figure 4.28: The CBO amplitude as a function of time in fill. The beginning of the data is not well understood, but after around  $50\text{ }\mu\text{s}$  the CBO amplitude falls away. Different envelopes for the amplitude are fit to the data with various degrees of success. Since most of the muons decay away early in the fill, it's the early fitted times that are most important, for which even the simple exponential in red is sufficient. The value for  $T/2\pi$  in the blue curve is approximately  $114.5\text{ }\mu\text{s}$ . Plot courtesy of James Mott.

## Chapter 5

# $\omega_a$ Measurement

The measurement of  $\omega_a$  is determined by counting the number of detected positrons in the calorimeters above some energy threshold, as described in Section 2.1. Doing so results in a histogram of counts which is modulated by  $\omega_a$ , Figure 2·4. Fitting for the frequency allows  $\omega_a$  to be extracted. The  $\omega_a$  measurement therefore consists of the steps needed to construct the histogram of counts, the fitting of that histogram, and any systematic studies done in the analysis.

### 5.1 Reconstruction

The calorimeters measure hit times and energies of impacting particles, where these hit times and energies are determined from the raw SiPM signals and a reconstruction procedure. In E989 there are two overall separate reconstruction algorithms, `ReconWest` and `ReconEast`. Each of these reconstruction algorithms is modularized, and the steps of the reconstruction process can be switched in and out at will. Using separate reconstruction methods gives confidence in any final results by removing single points of failure. The reconstruction method used in this analysis is `ReconWest`. A summary of its details will be presented here. A more thorough description is detailed by A. Fienberg [83].

The raw data are digitized waveforms, which are voltage versus time traces output from each SiPM for each calorimeter crystal hit. Due to the incredible amount of data coming in with the high muon fill rate, only those pulses which exceed some

threshold are saved to disk. An online processing system checks the traces against this pre-configured threshold by passing all of the data through a GPU farm [84]. If any trace is found above threshold, then the data is saved from every SiPM in every calorimeter, for a time range around the over-threshold trace. This time range is called a time island, similar to that in the tracking reconstruction, and typically has a width of 40 ns [83].

The traces are then fit with templates in order to extract the area and peak times of any present pulses. Each SiPM has its own templates, one for positrons and one for laser pulses. These templates are extracted from data, where each template is determined by collecting many single pulse traces from a SiPM, normalizing by pulse area, aligning in time, and averaging them. These templates were checked against many systematic effects in order to make sure that the constructed templates did not bias the energy or time measurements, such as hit angle, energy (pulse size), position, and rate, as well as aging effects [57, 83]. Each trace is fit using a  $\chi^2$  minimization algorithm with the corresponding SiPM templates in order to determine the time and energy of the hit. In order to fit for multiple pulses in a single time island, the fitting procedure first fits with a single template, and then checks the residuals for any remaining peaks. If peaks exist above some threshold, then the fitting is repeated until all pulses have been fit. The time measurement performance in the pulse finding was found to be unaffected by the number of pulses in a time island, and there is 100% pileup separation at 5 ns [83]. See Figure 5.1 for a typical single template fit to a SiPM trace.

Once a pulse has been fit with a template, the pulse area needs to be converted to real energy units using an energy calibration procedure. A couple of different techniques exist that can be used, including a method that counts photo-statistics seen in the SiPMs [83]. The default method used is a comparison of lost muon energy signa-

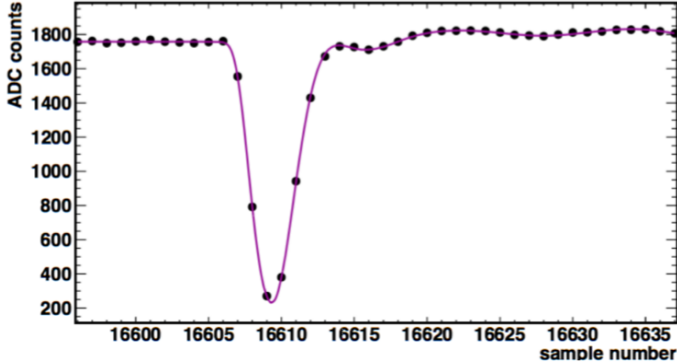


Figure 5.1: A template fit in purple to a SiPM trace delineated by the black points which is in units of ADC counts. Plot courtesy of Aaron Fienberg.

tures in the calorimeters. As described in Reference [85], muons lost from the storage ring can spiral inward and hit consecutive calorimeters with a specific time separation between calorimeter hits. These lost muons are minimum-ionizing particles, and thus leave a very distinct energy signature in the crystals, see Section 5.3. Selecting on the time signature allows hits corresponding to lost muons to be isolated, and the energy signature can be used to determine the appropriate conversions from area to energy<sup>1</sup>.

The energy calibration for positron hits as compared to lost muon hits then needs to be determined. Again there are a couple of different techniques, including a comparison of endpoint energies for high energy positrons which tail off at the magic momentum of 3.094 GeV, and comparison with simulation. The default technique is to calibrate the energies such that the optimal energy threshold for the  $\omega_a$  analysis is near 1.7 GeV [83]. Ultimately the energy calibration doesn't matter too much because it is not the energy units that really matter. What really matters is the number of positrons above some energy threshold, where that threshold can be optimized empirically. In fact, the entire  $\omega_a$  analysis could be done without even considering the energy of the incident positrons, and only considering the amplitude of the SiPM

---

<sup>1</sup>Different channels can also be equalized based on the energy signatures.

pulses<sup>2</sup>.

Each pulse fit now has an associated energy and time. Because the measurement of  $\omega_a$  depends heavily on the time reconstruction since the analysis is a frequency extraction, pulse times need to be corrected for various effects in order to reach the precision goal. The fitted times for each pulse need to be aligned on a fill-by-fill basis relative to the injection time of the beam, corrected for any channel differences due to differing pulse shapes or fiber lengths, and corrected for any calorimeter time misalignments due to the use of different laser system components. The fill-by-fill alignment is corrected for using the T0 detector as described in Section 3.1.1. The channel differences are corrected by aligning calorimeter channels in time using signals from islands with large simultaneous pulses in neighboring crystals. Calorimeters are time aligned using lost muon coincident events as described before. Once the times of the pulse fits or crystal hits have been determined, the energies can be corrected appropriately for gain effects measured by the laser system. As described in Section 3.2.3, the laser calibration system corrects for in-fill, out-of-fill, and SDTP effects [86]. Figure 5.2 shows an in-fill gain function fit to data for a single calorimeter. Systematic effects for corrected gain effects are studied in Section 5.5.1.

The last part of the calorimeter reconstruction is the clustering. Clustering is the stage which takes the individual template fit results from separate crystals, and turns them into the times, energies, and positions of decay positron impacts. For a time island with a single positron impact, the procedure is straightforward. The energy for the positron hit cluster is the sum of the individual hit crystal energies. The time for the cluster is taken as the time of the maximum energy hit in the island. This works because most of the deposited energy from a hit is localized to a single crystal. The position of the cluster is determined with a logarithmic weighting function between

---

<sup>2</sup>This statement ignores the effects of pileup which must be accounted for, and applies for a threshold style analysis, and not for other analysis methods which depend on the energy of the pulses.

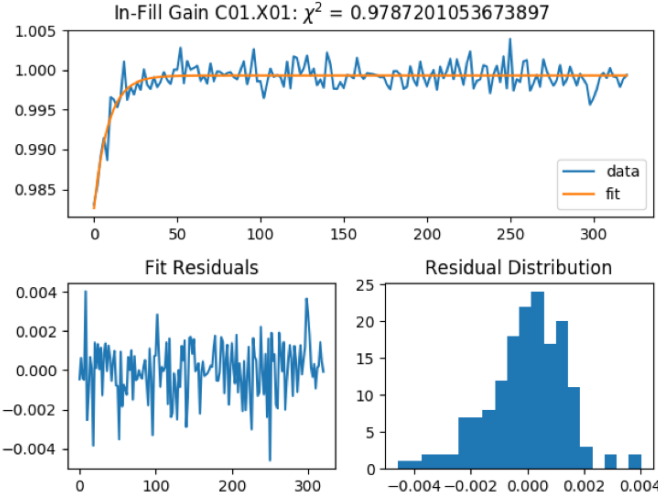


Figure 5.2: In-fill gain function fit for a single calorimeter crystal (top) and fit residuals (bottom). Each crystal has its own in-fill and SDTP gain function parameters. Plot courtesy of Matthias Smith.

crystal hits, which for a 2 GeV positron in the E989 calorimeters results in a resolution of 2 mm [83]. See Figure 5.3 for a single calorimeter cluster from a positron hit in the calorimeter. For a time island with multiple positron impacts, the individual crystal hits are separated in time, where the time partitioning separates hits that are 2.5 ns apart, and the clustering proceeds as before. For hits which are within this time window, a pileup event has occurred. If the pileup event happens within the same crystal, then the multiple hits are measured as a single hit, and this needs to be corrected for using a pileup subtraction technique, as described in Section 5.2.1. For hits that occur in separate crystals, the pileup can be resolved using the spatial separation of the calorimeters. This is an ongoing area of work, and one technique is described in Reference [83]. For this analysis the spatial separation was turned off, which simplifies the analysis somewhat. This increases the amount of pileup seen in the data, which then needs to be handled by the pileup subtraction technique. For the precision of the Run 1 analysis result, this was found to be acceptable.

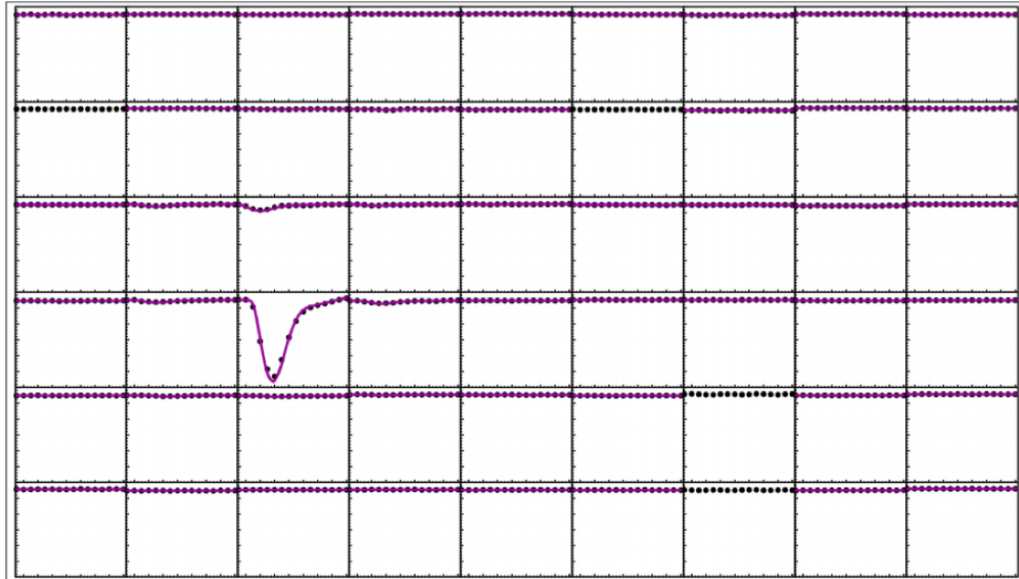


Figure 5.3: A single positron hit in the calorimeter, which resulted in a reconstructed calorimeter cluster. Each box is a crystal in the calorimeter, where the contained trace is the SiPM output fit with a template. The positron hit the crystal three from the left and three from the bottom, where it deposited most of its energy. Some of the energy was deposited in the neighboring crystals. Plot courtesy of Aaron Fienberg.

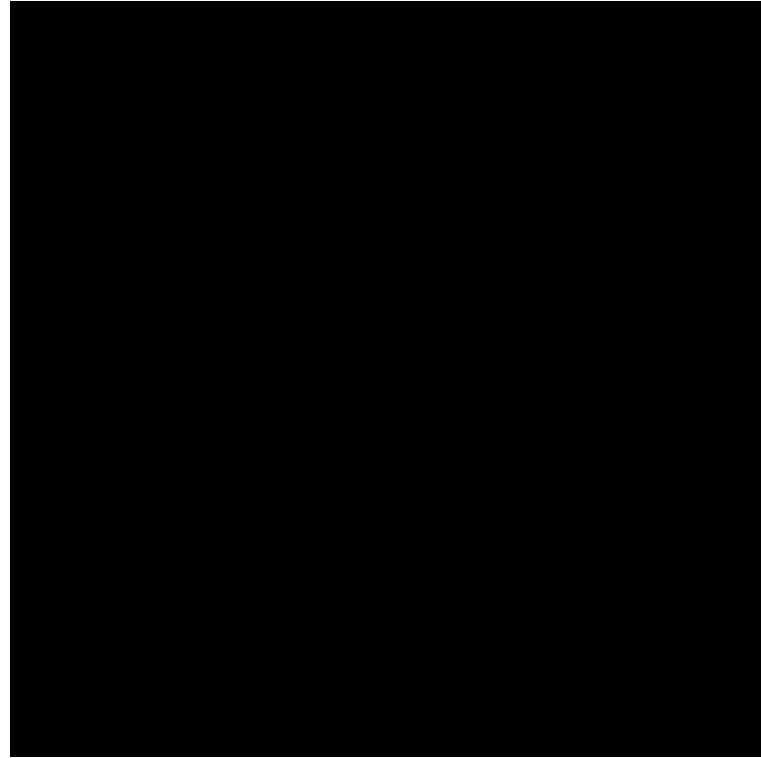


Figure 5.4: put a picture of the scanned optimal energy threshold here

## 5.2 Histogramming

Once the reconstruction has processed all the hits into clusters, the time spectra histograms need to be made.

-optimal energy threshold - reference last bit of wa intro section

-artificial deadtime -time randomization

### 5.2.1 Pileup subtraction

## 5.3 Lost muons

-need to include delta t plot and energy deposition plot

[85]

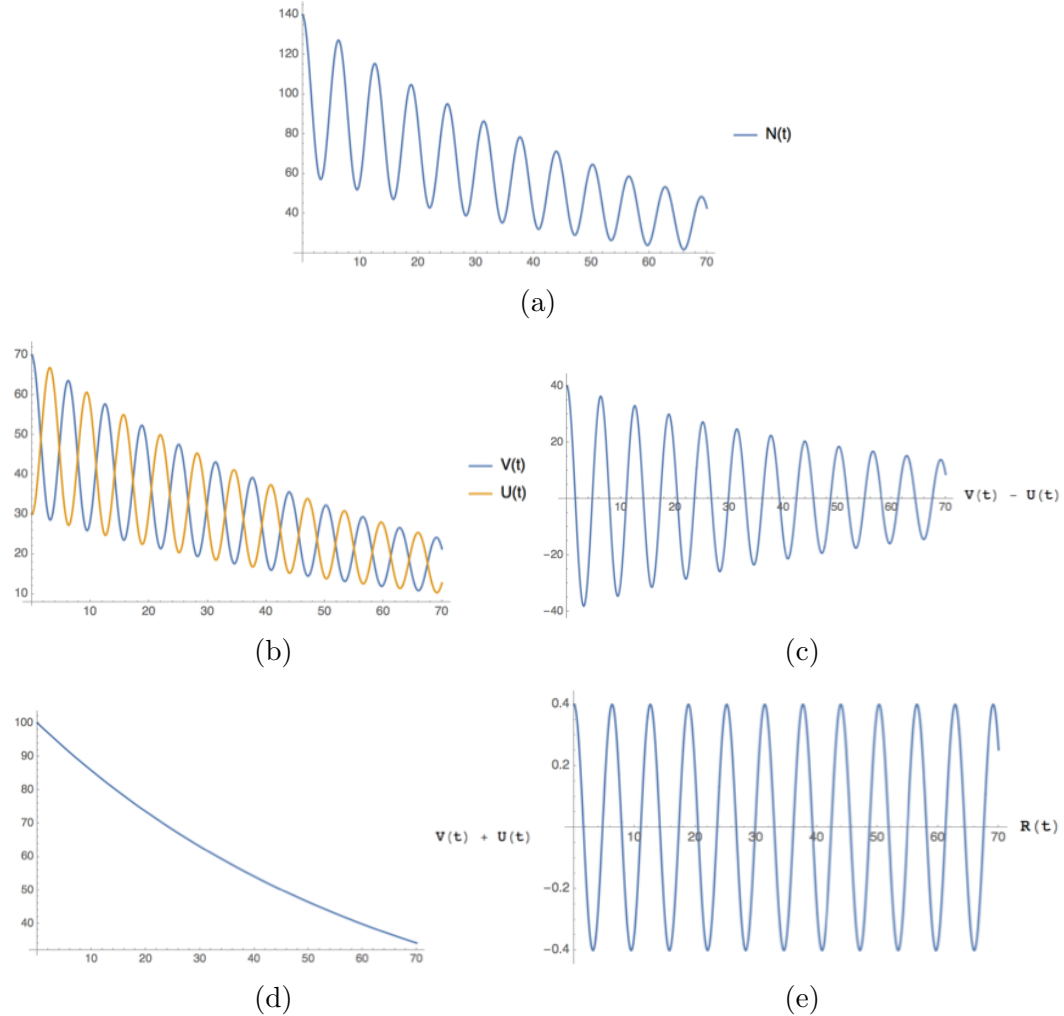


Figure 5.5

## 5.4 Fitting

-detail the ratio method - might need to pull stuff out from my appendix

$\omega_a$ Measurement Uncertainties	
Source of uncertainty	E989 Goal (ppb)
Gain changes	20
Pileup	40
Lost muons	20
CBO	30
E field and pitch corrections	30
Quadrature sum	70

Table 5.1: Systematic errors in the precession frequency measurement.  
**fill this table out more once I've gone through the various parts**

#### 5.4.1 CBO terms

### 5.5 Systematic errors

#### 5.5.1 Gain

-talk about the equations here - slight reference to either detector section or reconstruction section in this chapter

#### 5.5.2 Pileup

## Chapter 6

# Conclusion

### 6.1 Run 1 value of $a_\mu$

## Appendix A

# $g$ for Spin-1/2 Particles

Do I even want to include this derivation? Needs work if I am to do so. (If I remove it remove the reference in chapter 1 and just reference schwartz directly.)

Here is provided a relatively straightforward calculation of the g-factor for spin-1/2 particles, simplified from a derivation by Schwartz [87]. Start with the Dirac equation in the presence of an external electromagnetic field:

$$(i\gamma^\mu \partial_\mu - m - e\gamma^\mu A_\mu)\psi = 0, \quad (\text{A.1})$$

where  $\psi$  is the wavefunction of a spin-1/2 particle,  $m$  is its mass,  $A_\mu$  is the electromagnetic field operator,  $\partial_\mu$  is the 4-gradient, and  $\gamma^\mu$  are the gamma matrices<sup>1</sup>. Multiplying Equation A.1 by itself but with the sign on  $m$  switched, one arrives at the equation

$$[(i\partial_\mu - eA_\mu)(i\partial_\nu - eA_\nu)\gamma^\mu\gamma^\nu - m^2]\psi = 0. \quad (\text{A.2})$$

This can be split this into its symmetric and antisymmetric parts,

$$\left( \frac{1}{4}\{i\partial_\mu - eA_\mu, i\partial_\nu - eA_\nu\}\{\gamma^\mu, \gamma^\nu\} + \frac{1}{4}[i\partial_\mu - eA_\mu, i\partial_\nu - eA_\nu][\gamma^\mu, \gamma^\nu] - m^2 \right) \psi = 0, \quad (\text{A.3})$$

where  $[,]$  and  $\{, \}$  stand for the commutator and anti-commutator relations respec-

---

<sup>1</sup>Here  $\hbar$  and  $c$  will be set equal to 1.

tively. Using the identities

$$\frac{i}{2}[\gamma^\mu, \gamma^\nu] = \sigma^{\mu\nu} \quad (\text{A.4})$$

and

$$[i\partial_\mu - eA_\mu, i\partial_\nu - eA_\nu] = -ie[\partial_\mu A_\nu - \partial_\nu A_\mu] = -ieF_{\mu\nu}, \quad (\text{A.5})$$

where  $\sigma^{\mu\nu}$  is a tensor with elements consisting of the Pauli matrices, and  $F_{\mu\nu}$  is the electromagnetic field tensor, Equation A.3 can be formed as

$$((i\partial_\mu - eA_\mu)^2 - \frac{e}{2}F_{\mu\nu}\sigma^{\mu\nu} - m^2)\psi = 0. \quad (\text{A.6})$$

Expanding out the tensor objects

$$\frac{e}{2}F_{\mu\nu}\sigma^{\mu\nu} = -e \begin{pmatrix} (\vec{B} + i\vec{E}) \cdot \vec{\sigma} & 0 \\ 0 & (\vec{B} - i\vec{E}) \cdot \vec{\sigma} \end{pmatrix} \quad (\text{A.7})$$

and forming a new covariant derivative

$$\not{D}^2 = D_\mu^2 + \frac{e}{2}F_{\mu\nu}\sigma^{\mu\nu} \quad (\text{A.8})$$

where  $D_\mu = \gamma^\mu\partial_\mu$  is your ordinary covariant derivative, by moving to momentum space (this part is awkward) you can arrive at the equation

$$\frac{(H + eA)^2}{2m}\psi = \left(\frac{m}{2} + \frac{(\vec{p} + e\vec{A})^2}{2m} - 2\frac{e}{2m}\vec{B} \cdot \vec{s} \pm i\frac{e}{m}\vec{E} \cdot \vec{s}\right)\psi. \quad (\text{A.9})$$

Lo and behold, you have arrived at the Dirac  $g = 2$  result, contained in front of the magnetic piece in the form of Equation 1.1.

How then does such a term change at loop level? Most generally the vertex of a particle interacting with a magnetic field through the mediation of a photon can be

represented by

$$iM^\mu = \bar{u}(q_2)(f_1\gamma^\mu + f_2p^\mu + f_3q_1^\mu + f_4q_2^\mu)u(q_1) \quad (\text{A.10})$$

where  $q_1$  and  $q_2$  are the ingoing and outgoing four-momenta respectively, which can be constrained on-shell, and  $p$  is the four-momenta of the photon, which is off-shell. The  $f_i$  are in general contractions of four-momenta and gamma matrices. By using the Gordon identity

$$\begin{aligned} & \bar{u}(q_2)(q_1^\mu + q_2^\mu)u(q_1) \\ &= (2m)\bar{u}(q_2)\gamma^\mu u(q_1) + i\bar{u}(q_2)\sigma^{\mu\nu}(q_1^\nu - q_2^\nu)u(q_1) \end{aligned} \quad (\text{A.11})$$

any Feynman diagram can be reorganized into the form

$$iM^\mu = (-ie)\bar{u}\left[F_1\left(\frac{p^2}{m^2}\right)\gamma^\mu + \frac{i\sigma^{\mu\nu}}{2m}p_\nu F_2\left(\frac{p^2}{m^2}\right)\right]u, \quad (\text{A.12})$$

where  $F_1$  and  $F_2$  are form factors. One notices that the  $F_2$  piece is reminiscent of our magnetic dipole moment form that we derived from the Dirac equation. So the problem now becomes for any Feynman diagram calculation in any theory, at any order, to solve for this  $F_2$  to determine the contribution to the magnetic dipole moment.

## Appendix B

# Straw measurement angular correction

The tracker straws don't measure U and V coordinates directly, but instead measure the DCA radii deriving from measured hit times. In order to utilize the minimization procedure described in Section 4.2.2 on measured track parameters these radii must first be converted to U and V parameters, and similarly for the U and V errors. To first order the measured DCAs can be used identically as the U and V positions, but it was found that there were slight biases in the truth pulls due to this.

In order to improve the results, angular corrections were made to the DCAs to give more accurate estimates of the “measured” positions. It was found that for the error correction, assuming a straight particle path was sufficient for ideal results. For the position correction, it was found that assuming a circular particle path (constant field) correction for the curved tracks was sufficient. These corrections are dependent on the angle of the track, so it's important to note that during each successive iteration of the track fitting, the “measured” parameters are adjusted by the latest “predicted” momenta which change the angle of the track. The correction depends on whether the track went to the left or right side of the wire. Note that the momentum perpendicular to the straw measurement axis can be ignored since it doesn't affect the U or V value. A summary of the calculation of the right side correction follows, with the left side correction being calculated in a similar manner. See Figure B·1.

To solve for the measured U (or V) value, first use the following trigonometric

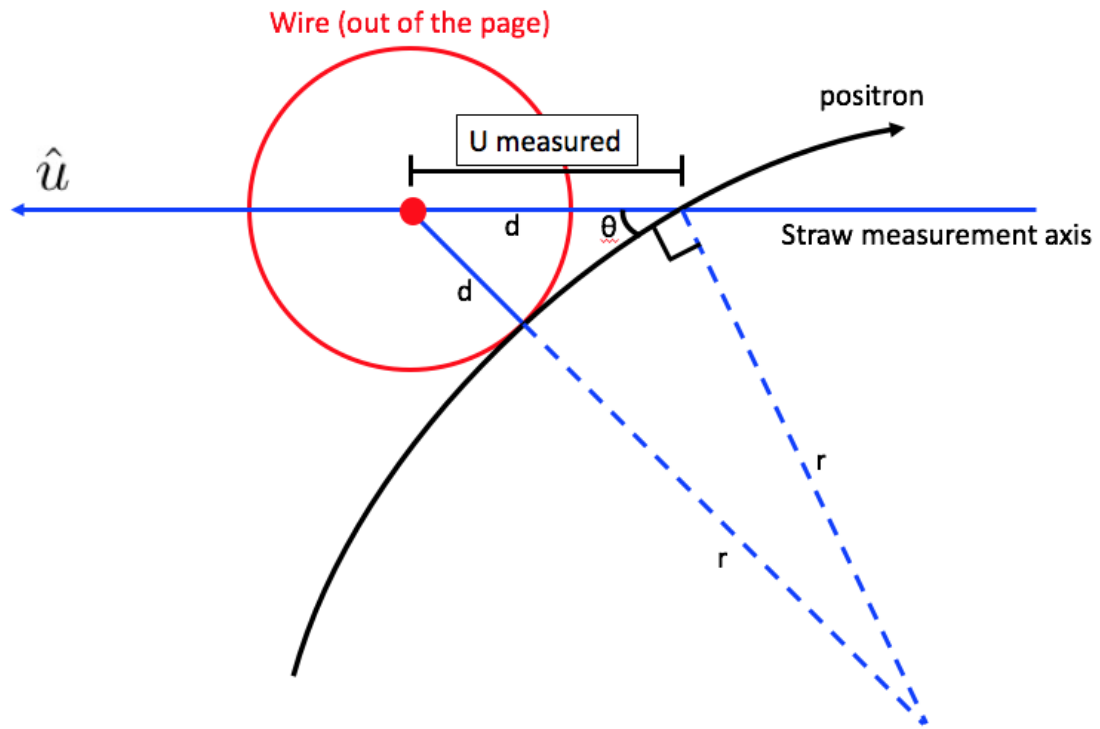


Figure B·1: A positron passing through a straw will produce a hit of radius  $d$ . The desired value is the U or V position along the straw measurement axis. The positron trajectory can be approximated as a circle in a constant magnetic field over the length of the path across the straw. The curvature for the high energy positrons is small such that  $r \gg d$  and the angle between the trajectory and the center of the circle can be approximated as  $90^\circ$ . Sizes and angles are exaggerated. A similar diagram can be drawn for positrons passing to the left of the wire. **Might want to clean up this picture at some point.**

identity:

$$(r + d)^2 = r^2 + u^2 - 2ru \cos(90 + \theta), \quad (\text{B.1})$$

where  $u$  is the parameter of interest. The angle  $\theta$  can be determined from

$$\hat{z}_{\parallel} \cdot \hat{p}_{\parallel} = \cos \theta, \quad \theta = \cos^{-1} \frac{p_{\parallel}}{p}, \quad (\text{B.2})$$

where  $p_{\parallel}$  is the positron momentum anti-parallel to the U measurement axis at the wire plane. Using some further trigonometric identities and solving for  $u$  gives

$$u = -r \sqrt{1 - \left(\frac{p_{\parallel}}{p}\right)^2} + \sqrt{d^2 + 2dr + r^2 \left(1 - \left(\frac{p_{\parallel}}{p}\right)^2\right)}, \quad (\text{B.3})$$

for the right side correction. Similarly,

$$u = +r \sqrt{1 - \left(\frac{p_{\parallel}}{p}\right)^2} - \sqrt{d^2 + 2dr + r^2 \left(1 - \left(\frac{p_{\parallel}}{p}\right)^2\right)}, \quad (\text{B.4})$$

for the left side correction. The radius  $r$  can be calculated from the momentum and magnetic field at the predicted hit position, and the momentum components can be determined within the Geant4 simulation. The straightline correction to the errors is done simpler manner using the Pythagorean theorem,

$$\sigma'_{uv} = \frac{\sigma_{uv}}{\sqrt{1 - \left(\frac{p_{\parallel}}{p}\right)^2}}, \quad (\text{B.5})$$

where  $\sigma'_{uv}$  is the improved error from original U or V error  $\sigma_{uv}$  on the DCA.

## Appendix C

# Ratio Method Derivation

### C.1 Ratio form and function

Consider the 5 parameter function:

$$N_5(t) = N_0 e^{-t/\tau} (1 + A \cos(\omega_a t + \phi)), \quad (\text{C.1})$$

which describes some ideal dataset in histogram format. Here  $\phi$  will be set to zero for simplicity. Now define the variables  $u_+(t)$ ,  $u_-(t)$ ,  $v_1(t)$ , and  $v_2(t)$  as

$$\begin{aligned} u_+(t) &= \frac{1}{4} N_5(t + T/2) \\ u_-(t) &= \frac{1}{4} N_5(t - T/2) \\ v_1(t) &= \frac{1}{4} N_5(t) \\ v_2(t) &= \frac{1}{4} N_5(t), \end{aligned} \quad (\text{C.2})$$

where the  $1/4$  out front reflects randomly splitting the whole dataset into 4 equally weighted sub-datasets, and  $T$  is the g-2 period known to high precision,  $\mathcal{O}(10^{-6})$ . This corresponds to a weighting of 1:1:1:1 between the datasets. To be explicit here regarding the signs, the counts that are filled into the histogram described by  $u_+$  have their times shifted as  $t \rightarrow t - T/2$ , which is what the function  $N_5(t + T/2)$  describes,

and vice versa for  $u_-$ . To form the ratio define the variables:

$$\begin{aligned} U(t) &= u_+(t) + u_-(t) \\ V(t) &= v_1(t) + v_2(t) \\ R(t) &= \frac{V(t) - U(t)}{V(t) + U(t)}. \end{aligned} \tag{C.3}$$

Plugging in and dividing the common terms ( $N_0 e^{-t/\tau}/4$ ),

$$R(t) = \frac{2(1 + A \cos(\omega_a t)) - e^{-T/2\tau}(1 + A \cos(\omega_a t + \omega_a T/2)) - e^{T/2\tau}(1 + A \cos(\omega_a t - \omega_a T/2))}{2(1 + A \cos(\omega_a t)) + e^{-T/2\tau}(1 + A \cos(\omega_a t + \omega_a T/2)) + e^{T/2\tau}(1 + A \cos(\omega_a t + \omega_a T/2))}. \tag{C.4}$$

Now set  $\omega_a T/2 = \delta$ , and note that  $T$  is really

$$\begin{aligned} T &= T_{guess} = \frac{2\pi}{\omega_a} + \Delta T, \\ \Delta T &= T_{guess} - T_{true}. \end{aligned} \tag{C.5}$$

Being explicit,

$$\delta = \frac{\omega_a}{2} T_{guess} = \frac{\omega_a}{2} \left( \frac{2\pi}{\omega_a} + \Delta T \right) = \pi + \pi \frac{\Delta T}{T_{true}} = \pi + \pi(\delta T), \tag{C.6}$$

and  $\delta$  can be redefined as

$$\delta = \pi(\delta T), \tag{C.7}$$

by flipping the sign of any cosine terms that contain  $\delta$ .

Then, using the trig identity

$$\cos(a \pm b) = \cos(a) \cos(b) \mp \sin(a) \sin(b) \tag{C.8}$$

so that

$$\begin{aligned}
\cos(\omega_a t \pm \delta) &= \cos(\omega_a t) \cos \delta \mp \sin(\omega_a t) \sin \delta \\
&\approx \cos(\omega_a t)(1 - \delta^2) \mp \sin(\omega_a t)\delta \\
&\approx \cos(\omega_a t),
\end{aligned} \tag{C.9}$$

since  $\delta \sim O(10^{-5})$ , the ratio becomes

$$R(t) \approx \frac{2(1 + A \cos(\omega_a t)) - (1 - A \cos(\omega_a t))(e^{-T/2\tau} + e^{T/2\tau})}{2(1 + A \cos(\omega_a t)) + (1 - A \cos(\omega_a t))(e^{-T/2\tau} + e^{T/2\tau})}. \tag{C.10}$$

Expanding

$$e^{\pm T/2\tau} = 1 \pm \frac{T}{2\tau} + \frac{1}{2} \left( \frac{T}{2\tau} \right)^2 \pm \dots, \tag{C.11}$$

replacing and simplifying,

$$R(t) \approx \frac{A \cos(\omega_a t) - C(1 - A \cos(\omega_a t))}{1 + C(1 - A \cos(\omega_a t))}, \tag{C.12}$$

where

$$C = \frac{1}{16} \left( \frac{T}{\tau} \right)^2 \approx 2.87 * 10^{-4}. \tag{C.13}$$

Using the expansion

$$f(x) = \frac{1}{1+x} = 1 - x + x^2 - \dots, \quad |x| < 1, \tag{C.14}$$

and since  $C$  is small, the denominator can be manipulated such that

$$\begin{aligned}
R(t) &\approx (A \cos(\omega_a t)) - C(1 - A \cos(\omega_a t))(1 - C(1 - A \cos(\omega_a t))) \\
&\approx A \cos(\omega_a t) - C + CA^2 \cos^2(\omega_a t),
\end{aligned} \tag{C.15}$$

after dropping terms of  $\mathcal{O}(C^2)$  and higher. In practice the last term is omitted since

it has a minimal effect on the fitted value of  $\omega_a$  [88], and one arrives at

$$R(t) \approx A \cos(\omega_a t) - C, \quad (\text{C.16})$$

the conventional 3 parameter ratio function.

In order to avoid approximations one can instead weight the counts in the histograms as

$$u_+(t) : u_-(t) : v_1(t) : v_2(t) = e^{T/2\tau} : e^{-T/2\tau} : 1 : 1, \quad (\text{C.17})$$

so that

$$\begin{aligned} u_+(t) &= \frac{e^{T/2\tau}}{2 + e^{T/2\tau} + e^{-T/2\tau}} N_5(t + T/2) \\ u_-(t) &= \frac{e^{-T/2\tau}}{2 + e^{T/2\tau} + e^{-T/2\tau}} N_5(t - T/2) \\ v_1(t) &= \frac{1}{2 + e^{T/2\tau} + e^{-T/2\tau}} N_5(t) \\ v_2(t) &= \frac{1}{2 + e^{T/2\tau} + e^{-T/2\tau}} N_5(t). \end{aligned} \quad (\text{C.18})$$

(These factors out front aren't so far off from 1/4 since  $e^{\pm T/2\tau} \approx e^{\pm 4.35/2*64.4} \approx 1.034, .967$ .) Then instead  $R(t)$  becomes

$$R(t) = \frac{2(1 + A \cos(\omega_a t)) - (1 - A \cos(\omega_a t + \delta)) - (1 - A \cos(\omega_a t - \delta))}{2(1 + A \cos(\omega_a t)) + (1 - A \cos(\omega_a t + \delta)) + (1 - A \cos(\omega_a t - \delta))}, \quad (\text{C.19})$$

where the  $e^{\pm T/2\tau}$  terms out front now cancel. Using Equation C.9 again and this time avoiding approximations in  $\delta$ ,

$$R(t) = \frac{2A \cos(\omega_a t)(1 + \cos \delta)}{4 + 2A \cos(\omega_a t)(1 - \cos \delta)}, \quad (\text{C.20})$$

after simplifying. In the limit that

$$\delta = \pi(\delta T) \rightarrow 0 \quad (\text{C.21})$$

since  $\delta T$  is small,

$$R(t) \approx A \cos(\omega_a t), \quad (\text{C.22})$$

with the only approximation being made at  $\mathcal{O}(\delta^2) \sim \mathcal{O}(10^{-10})$ .

Finally, while the 3 parameter ratio function suffices for fits to data containing slow modulations, it does not suffice for faster oscillation features. In that case it is more useful to fit with the non-approximated or simplified version of the ratio,

$$\begin{aligned} R(t) &= \frac{v_1(t) + v_2(t) - u_+(t) - u_-(t)}{v_1(t) + v_2(t) + u_+(t) + u_-(t)}, \\ &= \frac{2f(t) - f_+(t) - f_-(t)}{2f(t) + f_+(t) + f_-(t)}, \end{aligned} \quad (\text{C.23})$$

where

$$\begin{aligned} f(t) &= C(t)(1 + A \cos(\omega_a t + \phi)) \\ f_{\pm}(t) &= f(t \pm T_a/2), \end{aligned} \quad (\text{C.24})$$

and  $C(t)$  can encode any other effects in the data that need to be fitted for, such as the CBO,

$$C(t) = 1 + A_{cbo} \cdot e^{-t/\tau_{cbo}} \cdot \cos(\omega_{cbo}t + \phi_{cbo}). \quad (\text{C.25})$$

Additionally, any other fit parameters such as  $A$  or  $\phi$  can be made a function of  $t$ . Using the non-approximated form for the final fit function gives greater confidence in the fit results for the high precision  $\omega_a$  extraction necessary for the experimental measurement.

## C.2 Ratio errors

In order to determine the errors on the points in the formed ratio, Equation C.3, we use standard error propagation:

$$\sigma_R(t)^2 = \left( \frac{\partial R(t)}{\partial V(t)} \right)^2 \delta V(t)^2 + \left( \frac{\partial R(t)}{\partial U(t)} \right)^2 \delta U(t)^2 \quad (\text{C.26})$$

This works because  $V(t)$  and  $U(t)$  are statistically independent datasets. Using standard error propagation again,

$$\begin{aligned} \delta V(t)^2 &= \delta v_1(t)^2 + \delta v_2(t)^2 = v_1(t) + v_2(t) = V(t), \\ \delta U(t)^2 &= \delta u_+(t)^2 + \delta u_-(t)^2 = u_+(t) + u_-(t) = U(t). \end{aligned} \quad (\text{C.27})$$

Calculating out and simplifying the partial derivatives, (and this time dropping the  $t$ 's),

$$\begin{aligned} \frac{\partial R}{\partial V} &= \frac{2U}{(V+U)^2}, \\ \frac{\partial R}{\partial U} &= \frac{-2V}{(V+U)^2}. \end{aligned} \quad (\text{C.28})$$

Combining and simplifying, we arrive at the error formula:

$$\sigma_R^2 = \frac{4UV}{(V+U)^3} = \frac{1-R^2}{(V+U)} \quad (\text{C.29})$$

## Appendix D

# Pileup Modified Errors

In the pileup subtraction method detailed in Section 5.2.1, pileup events are statistically constructed and then subtracted from the data. Because of this, the errors on the bins need to be adjusted appropriately. Reference [89] describes the modified errors, but is not quite correct. Here is provided an improved calculation that is easier to understand. While we are mainly interested in the errors on the histogram bins after pileup subtraction, it first helps to examine the errors of the pileup histogram itself. Here we only consider doublets.

In the asymmetric shadow window pileup method, shadow doublets are constructed from two singlets. The pileup histogram is then filled as the sum of the doublets minus the singlets,

$$P = D - S, \tag{D.1}$$

where  $D$  or  $S$  are only added or subtracted when they are above some energy threshold. If the threshold is set to 0, then for every doublet one entry will be added and two will be subtracted. Since these entries are exactly correlated, the error in each time bin will be

$$\sigma_P = \sqrt{N_D}, \tag{D.2}$$

where  $N_D$  is the number of doublets in that time bin. If the energy threshold is above 0, then we can determine whether the counts in the pileup histogram increase

	$E_1 < E_{th}$	$E_1 > E_{th}$
$E_2 < E_{th}$	$N_1(+1)$	$N_2(0)$
$E_2 > E_{th}$	$N_3(0)$	$N_4(-1)$

Table D.1: Table of doublets above threshold. Here  $E_1$  and  $E_2$  are the energies of the two singlets,  $E_{th}$  is the energy threshold, and  $N_i$  are the number of doublets above threshold for the different combinations of  $E_1$  and  $E_2$ . ( $N_1$  is assumed above threshold here.) The numbers in the parentheses indicate the number of counts gained or lost in the pileup histogram.

or decrease based on whether the singlets and doublets are above threshold or not.

Table D.1 shows the different combinations of counts put into the pileup histogram.

The counts that go into  $P$  will be

$$\begin{aligned}
 P &= \sum_i N_i - \text{singlets above threshold} \\
 &= (N_1 + N_2 + N_3 + N_4) - (N_2 + N_4) - (N_3 + N_4) \\
 &= N_1 - N_4
 \end{aligned} \tag{D.3}$$

and the errors are

$$\sigma_P = \sqrt{N_1 + N_4}. \tag{D.4}$$

This makes sense considering the cases individually. In the cases for  $N_1$ , you will gain a count from the doublet above threshold, and lose no counts since both singlets are below threshold. In the cases for  $N_2$  and  $N_3$ , you will gain a count from the doublet, and lose a count from one of the singlets which is above threshold. In the cases for  $N_4$ , you will gain a count from the doublet and lose two counts from the singlets which are both above threshold. Since the doublet and singlets are exactly correlated, the  $N_1$  and  $N_4$  cases naturally result in a single weight being added into the error, while the  $N_2$  and  $N_3$  cases result in no additions to the error.

Now what about the pileup subtracted time spectrum? Our corrected spectrum can be written as

$$N_{\text{corrected}} = N_{\text{measured}} - P. \quad (\text{D.5})$$

What is in  $N_{\text{measured}}$  doesn't matter exactly. What we care about is what is in  $N_{\text{measured}}$  that is also within  $P$ , for that is where the correlations come from. Since  $N_{\text{measured}}$  is the sum of all singlets above threshold, we can write it as

$$N_{\text{measured}} = N_{\text{other}} + N_2 + N_3 + 2N_4 \quad (\text{D.6})$$

since we know that those cases  $N_i$  listed come from singlets above threshold, and  $N_{\text{other}}$  is anything in the measured hits that was not included in the pileup shadow construction. We can then replace  $P$  and simplify to get

$$N_{\text{corrected}} = N_{\text{other}} - N_1 + N_2 + N_3 + 3N_4. \quad (\text{D.7})$$

The error on the corrected histogram is then

$$\sigma_{N_{\text{corrected}}} = \sqrt{N_{\text{other}} + N_1 + N_2 + N_3 + 9N_4}. \quad (\text{D.8})$$

Replacing  $N_{\text{other}}$  as

$$N_{\text{other}} = N_{\text{corrected}} + N_1 - N_2 - N_3 - 3N_4, \quad (\text{D.9})$$

we can remove the dependence of the corrected histogram errors on the unknown quantity and arrive at

$$\begin{aligned} \sigma_{N_{\text{corrected}}} &= \sqrt{N_{\text{corrected}} + 2N_1 + 6N_4}, \\ &= \sqrt{N_{\text{corrected}}} \cdot \sqrt{1 + (2N_1 + 6N_4)/N_{\text{corrected}}}. \end{aligned} \quad (\text{D.10})$$

(This argument might seem circular at the end, but it works because of the squaring that occurs when calculating the error.) In the end we have a form for the bin errors of the pileup corrected histogram which only depend on  $N_1$  and  $N_4$  in addition to the number of counts in the corrected histogram. As shown it can be refactored into a form equal to the naive errors (just the bin content) times some correction factor. Since  $N_1$  and  $N_4$  are much smaller than  $N_{\text{corrected}}$  at all times, and because they decay away at about twice the rate as the pileup diminishes, the change to the errors is small, of the order 1 or 2% at 30  $\mu\text{s}$ .

## D.1 Pileup errors for the ratio function

Equation D.10 applies to the corrected errors for a pileup subtracted histogram, but what about the modifications to the ratio errors? If we parameterize that equation as

$$\sigma_{N_{\text{corrected}}} = \sqrt{N_{\text{corrected}}} \cdot \sqrt{\gamma(t)}, \quad (\text{D.11})$$

where the correction factor  $\gamma(t) \approx \gamma e^{-t/\tau_\mu}$  is small and decays at approximately the muon lifetime, we can recast the errors on the individual ratio sub-datasets as

$$\begin{aligned} \delta V(t)^2 &= \delta v_1(t)^2 \cdot \gamma(t) + \delta v_2(t)^2 \cdot \gamma(t) = (v_1(t) + v_2(t)) \cdot \gamma(t) = V(t) \cdot \gamma(t), \\ \delta U(t)^2 &= \delta u_+(t)^2 \cdot \gamma(t + T/2) + \delta u_-(t)^2 \cdot \gamma(t - T/2) \\ &\approx u_+(t) \cdot \gamma(t) e^{-T/2\tau} + u_-(t) \cdot \gamma(t) e^{+T/2\tau} \\ &\approx (u_+(t) + u_-(t)) \cdot \gamma(t) \cdot \left(1 + \frac{1}{2} \left(\frac{T}{2\tau}\right)^2\right) \\ &\approx U(t) \cdot \gamma(t), \end{aligned} \quad (\text{D.12})$$

where in the last step the  $\frac{1}{2} \left(\frac{T}{2\tau}\right)^2$  term has been neglected because it's small. With these approximations having been made, the modified errors on the ratio points simply

become

$$\sigma_R^2 \rightarrow \sigma_R^2 \cdot \gamma(t), \quad (\text{D.13})$$

with the correction being the same as that on the pileup subtracted histogram. Credit to Reference [90] for this derivation.

# Bibliography

- [1] P. Dirac. “The quantum theory of the electron”. In: *Proceedings of the Royal Society of London Series A, Containing Papers of a Mathematical and Physical Character* (1928).
- [2] J. E. Nafe, E. B. Nelson, and I. I. Rabi. “The Hyperfine Structure of Atomic Hydrogen and Deuterium”. In: *Phys. Rev.* 71 (12 June 1947), pp. 914–915. DOI: 10.1103/PhysRev.71.914. URL: <https://link.aps.org/doi/10.1103/PhysRev.71.914>.
- [3] Julian Schwinger. “On Quantum-Electrodynamics and the Magnetic Moment of the Electron”. In: *Phys. Rev.* 73 (4 Feb. 1948), pp. 416–417. DOI: 10.1103/PhysRev.73.416. URL: <https://link.aps.org/doi/10.1103/PhysRev.73.416>.
- [4] Joshua Ellis. “TikZ-Feynman: Feynman diagrams with TikZ”. In: *Comput. Phys. Commun.* 210 (2017), pp. 103–123. DOI: 10.1016/j.cpc.2016.08.019. arXiv: 1601.05437 [hep-ph].
- [5] Max Dohse. “TikZ-FeynHand: Basic User Guide”. In: (2018). arXiv: 1802.00689 [cs.0H].
- [6] Tatsumi Aoyama et al. “Complete Tenth-Order QED Contribution to the Muon g-2”. In: *Phys. Rev. Lett.* 109 (2012), p. 111808. DOI: 10.1103/PhysRevLett.109.111808. arXiv: 1205.5370 [hep-ph].
- [7] Tatsumi Aoyama, Toichiro Kinoshita, and Makiko Nio. “Revised and Improved Value of the QED Tenth-Order Electron Anomalous Magnetic Moment”. In: *Phys. Rev.* D97.3 (2018), p. 036001. DOI: 10.1103/PhysRevD.97.036001. arXiv: 1712.06060 [hep-ph].
- [8] C. Gnendiger, D. Stöckinger, and H. Stöckinger-Kim. “The electroweak contributions to  $(g - 2)_\mu$  after the Higgs boson mass measurement”. In: *Phys. Rev.* D88 (2013), p. 053005. DOI: 10.1103/PhysRevD.88.053005. arXiv: 1306.5546 [hep-ph].
- [9] Tadashi Ishikawa, Nobuya Nakazawa, and Yoshiaki Yasui. “Numerical calculation of the full two-loop electroweak corrections to muon  $(g-2)$ ”. In: (2018). arXiv: 1810.13445 [hep-ph].
- [10] Bernd A. Kniehl. “Dispersion relations in loop calculations”. In: *Acta Phys. Polon.* B27 (1996), pp. 3631–3644. arXiv: hep-ph/9607255 [hep-ph].

- [11] F. Jegerlehner. *The Anomalous Magnetic Moment of the Muon*. Springer Tracts in Modern Physics. Springer Berlin Heidelberg, 2007. ISBN: 9783540726340. URL: <https://books.google.com/books?id=uxQj004Py6AC>.
- [12] D. Babusci et al. “Precision measurement of  $\sigma(e^+e^- \rightarrow \pi^+\pi^-\gamma)/\sigma(e^+e^- \rightarrow \mu^+\mu^-\gamma)$  and determination of the  $\pi^+\pi^-$  contribution to the muon anomaly with the KLOE detector”. In: *Phys. Lett.* B720 (2013), pp. 336–343. DOI: 10.1016/j.physletb.2013.02.029. arXiv: 1212.4524 [hep-ex].
- [13] T. Xiao et al. “Precision Measurement of the Hadronic Contribution to the Muon Anomalous Magnetic Moment”. In: *Phys. Rev.* D97.3 (2018), p. 032012. DOI: 10.1103/PhysRevD.97.032012. arXiv: 1712.04530 [hep-ex].
- [14] Bogdan Malaescu. “Measurement of hadronic cross sections at BABAR with ISR and implications for the muon (g-2)”. In: *Proceedings, International Conference on the Structure and the Interactions of the Photon including the 20th International Workshop on Photon-Photon Collisions and the International Workshop on High Energy Photon Linear Colliders, PHOTON 2013: Paris, France, May 20-24, 2013*. 2014. arXiv: 1404.6887 [hep-ex]. URL: <http://www-public.slac.stanford.edu/sciDoc/docMeta.aspx?slacPubNumber=SLAC-PUB-16106>.
- [15] M. Ablikim et al. “Measurement of the  $e^+e^- \rightarrow \pi^+\pi^-$  cross section between 600 and 900 MeV using initial state radiation”. In: *Phys. Lett.* B753 (2016), pp. 629–638. DOI: 10.1016/j.physletb.2015.11.043. arXiv: 1507.08188 [hep-ex].
- [16] Alexander Keshavarzi, Daisuke Nomura, and Thomas Teubner. “Muon  $g-2$  and  $\alpha(M_Z^2)$ : a new data-based analysis”. In: *Phys. Rev.* D97.11 (2018), p. 114025. DOI: 10.1103/PhysRevD.97.114025. arXiv: 1802.02995 [hep-ph].
- [17] Michel Davier et al. “Reevaluation of the hadronic vacuum polarisation contributions to the Standard Model predictions of the muon  $g-2$  and  $\alpha(m_Z^2)$  using newest hadronic cross-section data”. In: *Eur. Phys. J.* C77.12 (2017), p. 827. DOI: 10.1140/epjc/s10052-017-5161-6. arXiv: 1706.09436 [hep-ph].
- [18] T. Blum et al. “Calculation of the Hadronic Vacuum Polarization Contribution to the Muon Anomalous Magnetic Moment”. In: *Phys. Rev. Lett.* 121 (2 July 2018), p. 022003. DOI: 10.1103/PhysRevLett.121.022003. URL: <https://link.aps.org/doi/10.1103/PhysRevLett.121.022003>.
- [19] Gilberto Colangelo et al. “Dispersive approach to hadronic light-by-light scattering”. In: *JHEP* 09 (2014), p. 091. DOI: 10.1007/JHEP09(2014)091. arXiv: 1402.7081 [hep-ph].
- [20] Gilberto Colangelo et al. “Dispersion relation for hadronic light-by-light scattering: theoretical foundations”. In: *JHEP* 09 (2015), p. 074. DOI: 10.1007/JHEP09(2015)074. arXiv: 1506.01386 [hep-ph].

- [21] Gilberto Colangelo et al. “Rescattering effects in the hadronic-light-by-light contribution to the anomalous magnetic moment of the muon”. In: *Phys. Rev. Lett.* 118.23 (2017), p. 232001. DOI: 10.1103/PhysRevLett.118.232001. arXiv: 1701.06554 [hep-ph].
- [22] Thomas Blum et al. “Lattice Calculation of Hadronic Light-by-Light Contribution to the Muon Anomalous Magnetic Moment”. In: *Phys. Rev.* D93.1 (2016), p. 014503. DOI: 10.1103/PhysRevD.93.014503. arXiv: 1510.07100 [hep-lat].
- [23] Thomas Blum et al. “Connected and Leading Disconnected Hadronic Light-by-Light Contribution to the Muon Anomalous Magnetic Moment with a Physical Pion Mass”. In: *Phys. Rev. Lett.* 118.2 (2017), p. 022005. DOI: 10.1103/PhysRevLett.118.022005. arXiv: 1610.04603 [hep-lat].
- [24] Thomas Blum et al. “Using infinite volume, continuum QED and lattice QCD for the hadronic light-by-light contribution to the muon anomalous magnetic moment”. In: *Phys. Rev.* D96.3 (2017), p. 034515. DOI: 10.1103/PhysRevD.96.034515. arXiv: 1705.01067 [hep-lat].
- [25] Nils Asmussen et al. “Hadronic light-by-light scattering in the anomalous magnetic moment of the muon”. In: *15th International Workshop on Tau Lepton Physics (TAU2018) Amsterdam, Netherlands, September 24-28, 2018*. 2018. arXiv: 1811.08320 [hep-lat].
- [26] Andreas Nyffeler. “Precision of a data-driven estimate of hadronic light-by-light scattering in the muon  $g - 2$ : Pseudoscalar-pole contribution”. In: *Phys. Rev.* D94.5 (2016), p. 053006. DOI: 10.1103/PhysRevD.94.053006. arXiv: 1602.03398 [hep-ph].
- [27] B. Lee Roberts. “The History of the Muon  $(g - 2)$  Experiments”. In: *15th International Workshop on Tau Lepton Physics (TAU2018) Amsterdam, Netherlands, September 24-28, 2018*. 2018. arXiv: 1811.06974 [hep-ex].
- [28] G. W. Bennett et al. “Final Report of the Muon E821 Anomalous Magnetic Moment Measurement at BNL”. In: *Phys. Rev.* D73 (2006), p. 072003. DOI: 10.1103/PhysRevD.73.072003. arXiv: hep-ex/0602035 [hep-ex].
- [29] D. Hanneke, S. Fogwell, and G. Gabrielse. “New Measurement of the Electron Magnetic Moment and the Fine Structure Constant”. In: *Phys. Rev. Lett.* 100 (2008), p. 120801. DOI: 10.1103/PhysRevLett.100.120801. arXiv: 0801.1134 [physics.atom-ph].
- [30] Peter J. Mohr, David B. Newell, and Barry N. Taylor. “CODATA recommended values of the fundamental physical constants: 2014”. In: *Rev. Mod. Phys.* 88 (3 Sept. 2016), p. 035009. DOI: 10.1103/RevModPhys.88.035009. URL: <https://link.aps.org/doi/10.1103/RevModPhys.88.035009>.

- [31] Richard H. Parker et al. “Measurement of the fine-structure constant as a test of the Standard Model”. In: *Science* 360.6385 (2018), pp. 191–195. ISSN: 0036-8075. DOI: 10.1126/science.aap7706. eprint: <https://science.sciencemag.org/content/360/6385/191.full.pdf>. URL: <https://science.sciencemag.org/content/360/6385/191>.
- [32] L. Roberts. Personal communication. 2019.
- [33] J. Jackson. *Classical Electrodynamics*. Wiley Indiana, 2011.
- [34] W. Liu et al. “High Precision Measurements of the Ground State Hyperfine Structure Interval of Muonium and of the Muon Magnetic Moment”. In: *Phys. Rev. Lett.* 82 (4 Jan. 1999), pp. 711–714. DOI: 10.1103/PhysRevLett.82.711. URL: <https://link.aps.org/doi/10.1103/PhysRevLett.82.711>.
- [35] E. D. Commins and P. H. Bucksbaum. *Weak interactions of leptons and quarks*. Cambridge University Press, 1983.
- [36] G. W. Bennett et al. “Statistical equations and methods applied to the precision muon (g-2) experiment at BNL”. In: *Nucl. Instrum. Meth.* A579 (2007), pp. 1096–1116. DOI: 10.1016/j.nima.2007.06.023.
- [37] J. Grange et al. “Muon (g-2) Technical Design Report”. In: (2015). arXiv: 1501.06858 [physics.ins-det].
- [38] R. Ossofsky. *Improving Magnetic Field Uniformity in the Muon g – 2 Storage Ring*. Muon g-2 DocDB 12497. 2018.
- [39] M. Tanabashi et al. “Review of Particle Physics”. In: *Phys. Rev. D* 98 (3 Aug. 2018), p. 030001. DOI: 10.1103/PhysRevD.98.030001. URL: <https://link.aps.org/doi/10.1103/PhysRevD.98.030001>.
- [40] Diktys Stratakis et al. “Accelerator performance analysis of the Fermilab Muon Campus”. In: *Phys. Rev. Accel. Beams* 20.11 (2017), p. 111003. DOI: 10.1103/PhysRevAccelBeams.20.111003. arXiv: 1803.00597 [physics.acc-ph].
- [41] Cary Yoshikawa et al. “Optimization of the Target Subsystem for the New g-2 Experiment”. In: (Jan. 2013).
- [42] A. Yamamoto et al. “The superconducting inflector for the BNL g-2 experiment”. In: *Nucl. Instrum. Meth.* A491 (2002), pp. 23–40. DOI: 10.1016/S0168-9002(02)01232-9.
- [43] Y. K. Semertzidis et al. “The Brookhaven muon (g-2) storage ring high voltage quadrupoles”. In: *Nucl. Instrum. Meth.* A503 (2003), pp. 458–484. DOI: 10.1016/S0168-9002(03)00999-9.
- [44] H. Wiedermann. *Particle Accelerator Physics*. Springer-Verlag New York, 1993.
- [45] A. Chapelain D. Seleznev and D. Rubin. *Extraction of the Muon Beam Frequency Distribution via the Fourier Analysis of the Fast Rotation Signal*. Muon g-2 Note 130 DocDB 9701. 2018.

- [46] A. Keshavarzi. *Fast rotation summary*. Muon g-2 DocDB 15304. 2018.
- [47] M. J. Syphers. *Storage Ring Linear Tune Tables*. Muon g-2 DocDB 11547. 2018.
- [48] A. Chapelain. *Data Quality Control - a.k.a. DQC*. Muon g-2 DocDB 15295. 2018.
- [49] H. Binney et al. *Data Quality Control for the 60-Hour Dataset*. Muon g-2 DocDB 16568. 2019.
- [50] K. Khaw. *How each dataset is different for Run 1 of E989*. Muon g-2 DocDB 15781. 2019.
- [51] H. Binney. *T0: update and current work*. Muon g-2 DocDB 10162. 2018.
- [52] A. Fienberg. *T0 Detector*. Muon g-2 DocDB 10911. 2018.
- [53] P. Kammel et al. *Inflector Beam Monitoring System Justification Document*. Muon g-2 DocDB 2722. 2015.
- [54] B. MacCoy and P. Kammel. *IBMS Update*. Muon g-2 DocDB 10944. 2018.
- [55] F. Gray. *Fiber Harp Beam Monitor*. Muon g-2 DocDB 8366. 2017.
- [56] A. T. Fienberg et al. “Studies of an array of PbF<sub>2</sub> Cherenkov crystals with large-area SiPM readout”. In: *Nucl. Instrum. Meth.* A783 (2015), pp. 12–21. DOI: 10.1016/j.nima.2015.02.028. arXiv: 1412.5525 [physics.ins-det].
- [57] J. Kaspar et al. “Design and performance of SiPM-based readout of PbF<sub>2</sub> crystals for high-rate, precision timing applications”. In: *JINST* 12.01 (2017), P01009. DOI: 10.1088/1748-0221/12/01/P01009. arXiv: 1611.03180 [physics.ins-det].
- [58] David A. Sweigart. “A new MicroTCA-based waveform digitizer for the Muon g-2 experiment”. In: *PoS ICHEP2016* (2016), p. 845. DOI: 10.22323/1.282.0845. arXiv: 1612.05145 [physics.ins-det].
- [59] A. Anastasi et al. “The laser control of the muon  $g-2$  experiment at Fermilab”. In: *JINST* 13.02 (2018), T02009. DOI: 10.1088/1748-0221/13/02/T02009.
- [60] S. Charity. “Beam profile measurements using the straw tracking detectors at the Fermilab muon  $g-2$  experiment, and a study of their sensitivity to a muon electric dipole moment”. PhD thesis. University of Liverpool, 2018.
- [61] W. Riegler W. Blum and L. Rolandi. *Particle Detection with Drift Chambers*. Springer-Verlag Berlin Heidelberg, 2008.
- [62] M. Raminsky. *Garfield*. Muon g-2 DocDB 905. 2012.
- [63] J. Mott. *Garfield Paramterisation: First Simulation Attempt*. Muon g-2 DocDB 6171. 2017.
- [64] W. Turner. “The construction and commissioning of the straw tracking detector in the new muon  $g-2$  experiment at Fermilab”. PhD thesis. University of Liverpool, 2018.

- [65] C. Green et al. “The Art Framework”. In: *J. Phys. Conf. Ser.* 396 (2012), p. 022020. DOI: 10.1088/1742-6596/396/2/022020.
- [66] T. Walton. *Track Finding Overview*. Muon g-2 DocDB 7580. 2017.
- [67] T. Walton and J. Price. *Track formation details*. Muon g-2 DocDB 8555. 2017.
- [68] J. Price. *Track Finding - simple pattern recognition*. Muon g-2 DocDB 5793. 2017.
- [69] N. Kinnaird. *Geane Track Fitting*. Muon g-2 Note 184 DocDB 8102. 2017.
- [70] V. Innocente, M. Maire, and E. Nagy. “GEANE: Average tracking and error propagation package”. In: *MC 91: Detector and event simulation in high-energy physics. Proceedings, Workshop, Amsterdam, Netherlands, April 8-12, 1991*. 1991, pp. 58–78. URL: [http://innocentonnice.web.cern.ch/innocentonnice/napoli99/geane\\_manual.ps](http://innocentonnice.web.cern.ch/innocentonnice/napoli99/geane_manual.ps).
- [71] Lia Lavezzi. “The fit of nuclear tracks in high precision spectroscopy experiments”. pp. 57-86. PhD thesis. Pavia U., 2007. URL: [http://bamboo.pv.infn.it/doc/L\\_Lavezzi.pdf](http://bamboo.pv.infn.it/doc/L_Lavezzi.pdf).
- [72] K. Lassila-Perini and L. Urban. “Energy loss in thin layers in GEANT”. In: *Nucl. Instrum. Meth.* A362 (1995), pp. 416–422. DOI: 10.1016/0168-9002(95)00344-4.
- [73] A. Strandlie and W. Wittek. “Derivation of Jacobians for the propagation of covariance matrices of track parameters in homogeneous magnetic fields”. In: *Nucl. Instrum. Meth.* A566 (2006), pp. 687–698.
- [74] V. Innocente and E. Nagy. “Trajectory fit in presence of dense materials”. In: *Nucl. Instrum. Meth.* A324 (1993), pp. 297–306. DOI: 10.1016/0168-9002(93)90992-Q.
- [75] N. Kinnaird J. Mott and F. Azfar. *Residuals, Covariance & Correlation in Fitting Straight Line Tracks in UV*. Muon g-2 DocDB 3813. 2016.
- [76] Gaël Guennebaud, Benoît Jacob, et al. *Eigen v3*. <http://eigen.tuxfamily.org>. 2010.
- [77] N. Kinnaird. *Left/Right - What we do/have at the moment*. Muon g-2 DocDB 12017. 2018.
- [78] J. Price. *LR from wire fit*. Muon g-2 DocDB 6947. 2017.
- [79] J. Price and S. Charity. *Extrapolation uncertainty*. Muon g-2 DocDB 14920. 2018.
- [80] J. Mott. *Track Quality Cuts*. Muon g-2 DocDB 16282. 2019.
- [81] J. Mott. *Track Quality Cuts: Second Edition*. Muon g-2 DocDB 16420. 2019.
- [82] J. Mott et al. *CBO Frequency Change*. Muon g-2 DocDB 14208. 2018.

- [83] A. Fienberg. “Measuring the Precession Frequency in the E989 Muon  $g - 2$  Experiment”. PhD thesis. University of Washington, 2019.
- [84] W. Gohn. “Data Acquisition with GPUs: The DAQ for the Muon  $g-2$  Experiment at Fermilab”. In: *PoS ICHEP2016* (2016), p. 174. DOI: 10.22323/1.282.0174. arXiv: 1611.04959 [physics.ins-det].
- [85] Jason Crnkovic et al. “Lost Muon Study for the Muon g-2 Experiment at Fermilab”. In: *Proceedings, 8th International Particle Accelerator Conference (IPAC 2017): Copenhagen, Denmark, May 14-19, 2017*. 2017, WEPIK119. DOI: 10.18429/JACoW-IPAC2017-WEPIK119.
- [86] A. Driutti et al. *Status of the STDP module and of the new IFG correction functions*. Muon g-2 DocDB 16003. 2019.
- [87] M. Schwartz. *Quantum Field Theory and the Standard Model*. Cambridge University Press, 2014.
- [88] L. Duong. “A Precise Measurement of the Anomalous Magnetic Moment of the Positive Muon”. PhD thesis. University of Minnesota, 2001.
- [89] F. Farley et al. *Estimation of Error in Differential Pileup Subtracted Data*. E821 Muon g-2 Note 377. 2018.
- [90] J. Paley. “Measurement of the Anomalous Magnetic Moment of the Negative Muon to 0.7 Parts Per Million”. PhD thesis. Boston University, 2004.

# Nicholas Kinnaird

512-922-0534 | nickkinn@bu.edu | 205 N Oakhurst Dr, Aurora, IL

## 6.2 Education

**Boston University**  
*Ph.D. in Physics*

Boston, MA  
2019

**Dissertation:** Measurement of the Magnetic Anomaly of the Muon to X parts per billion  
in Run 1 of the Fermilab Muon  $g - 2$  Experiment

**Boston University**  
*M.A. in Physics*

Boston, MA  
2016

**University of Texas at Austin**  
*B.S. in Physics*

Austin, TX  
2013

**University of Texas at Austin**  
*B.S. in Mathematics*

Austin, TX  
2013